THE MICROMETEOROLOGICAL EFFECTS OF DRAINAGE FLOW IN THE WINTER ATMOSPHERIC BOUNDARY LAYER

By

John Arthur Mayfield Junior

RECOMMENDED: _____

_____

_____
Advisory Committee Chair

_____
Chair, Department of Atmospheric Sciences

APPROVED: _____
Dean, College of Natural Science and Mathematics

_____
Dean of the Graduate School

_____
Date

THE MICROMETEOROLOGICAL EFFECTS OF DRAINAGE FLOW IN THE WINTER ATMOSPHERIC BOUNDARY LAYER

A

THESIS

Presented to the Faculty

of the University of Alaska Fairbanks

in Partial Fulfillment of the Requirements

for the Degree of

MASTER OF SCIENCE

By

John A. Mayfield, Jr., B.S.

Fairbanks, Alaska

December 2011

Abstract

This thesis presents observational research conducted in the framework of the Winter Boundary Layer Experiment (Wi-BLEx) in Fairbanks, interior of Alaska. Two intensive observing periods (IOPs) were carried out from October 2009 to February 2010 and from November 2010 to March 2011. The objectives of this thesis are: (1) to study the micrometeorological effects of drainage flow on the Stable Atmospheric Boundary Layer (SABL) surface layer, and (2) on the vertical structure of the SABL, and (3) to study the large-scale synoptic features represented by the elevated inversions (EI) as possible radiative-dynamic mechanisms affecting the local SABL stratification and, the occurrence of drainage flows.

Previous observations carried out in winter 2008-2009 suggested the presence of a small-scale flow penetrating and modifying differently the structure of the SABL across the winter close to the foothills, northwest of Fairbanks. In this research, surface turbulence at local and basin scales was measured by sonic anemometers and laser scintillometry respectively. Vertical profiling of thermal turbulence and flow dynamics of the SABL were determined by means of a Doppler Phased Array Acoustic Sounder. This study found that at the penetration of the drainage flow the surface atmospheric boundary layer becomes turbulent developing mixing. The drainage flow produces shear driven thermal turbulence in upper levels of the SABL and combined with surface stress increase in the surface layer. The set of observations across the winter revealed the presence of sustained and intermittent drainage flow. At breakup of the drainage flow the surface layer re-stratifies. At synoptic level, the drainage flow occurrence coincides with the dominance of anticyclone surface pressure system and weak pressure gradient forces. Observational evidence was found

that the SABL structure is lifted via a radiative-dynamic mechanism caused by the presence of EI layers when the synoptic pattern changes. The studied drainage flow effectively introduces mixing between the colder drainage flow airmass and the polluted urban valley air mass.

Table of Contents

Page

Signature Page i

Title Page ii

Abstract iii

Table of Contents v

Nomenclature and Acronyms viii

List of Figures ix

List of Tables xii

Acknowledgements xiii

Chapter 1: Introduction 1

1.1 Lower Atmospheric Circulation and Flow Pattern during the Arctic Winter 1

1.2 High-Latitude Atmospheric Boundary Layer 2

1.3 Drainage Flow Development and Exchange Processes 6

1.4 Formulation of the Thesis and Objectives 9

1.5 Organization of the Thesis 10

1.6 References 13

Chapter 2: Flow Variability and the Atmospheric Boundary Layer Structure during Winter in the Interior of Alaska 17

2.1 Abstract 17

2.2 Introduction 18

2.3 Methodology 22

2.4 Flow Variability 27

2.4.1 Period I: October to December 2009 28

2.4.1.1 Period I-I: 11 to 18 October 2009 28

2.4.1.2 Period I-II: 13 to 25 October 2009 28

2.4.1.3 Period I-III 1 to 8 November 2009 29

2.4.1.4 Period I-IV 20 to 24 November 2009 29

2.4.2 Period II: January – February 2010 30

2.4.2.1 Period II-III: 31 January to 7 February 2010 30

2.4.2.2 Period II-III: 31 January to 7 February 2010 30

2.4.2.3 Period II-III: 31 January to 7 February 2010 31

2.5 ABL Structure 32

2.5.1 Case I: 23-25 October 2009 (low-level jet) 34

2.5.2 Case II: 22-24 November, 2009 (synoptic transient) 36

2.5.3 Case III: 26-27 January 2010 (Anticyclone Situation) 37

2.6 Discussion and Conclusions 39

2.7 Acknowledgements 43

2.8 References 43

2.9 Figures 48

2.10 Tables 65

Chapter 3: Influence of Drainage Flow in the Wintertime Atmospheric Boundary Layer at High Latitude 66

3.1 Abstract 66

3.2 Introduction 67

3.3 Experiment and Methodology 70

3.4 Meteorological and Mean Flow Conditions during Observations 72

3.5 Drainage Flow Events – Turbulent variables 74

3.5.1 Case I 74

3.5.2 Case II 76

3.5.3 Case III 78

3.6 Discussion 80

3.7 Conclusions 84

3.8 References 87

3.9 Figures 89

Chapter 4: The Layered Structure of the Winter Atmospheric Boundary Layer in the Interior of Alaska 119

4.1 Abstract 119

4.2 Introduction 120

4.3 Data and Methodology 125

4.4 Temporal Series of Inversion Layers 129

4.5 Locally-Controlled Inversions 131

4.6 Synoptically-Controlled Inversions 134

4.7 Discussion and Summary 138

4.8 Acknowledgements 145

4.9 References 146

4.10 Figures 152

4.11 Tables 171

Chapter 5: Thesis Summary and Research Perspectives 180

Nomenclature and Acronyms

ABL – Atmospheric Boundary Layer
AC – Anticyclone
BL – Boundary Layer
C_T^2 – Temperature Turbulence Structure (Acoustic Backscatter) (a.u.)
C_n^2 – Refractive-Index Turbulence Structure ($m^{-2/3}$)
H – Turbulent Sensible Heat Flux (Wm^{-2})
IR – infrared radiation
SABL – Stable Atmospheric Boundary Layer
SBI – Surface-Based Inversion
sodar – SOund Detection And Ranging
T –Temperature ($^{\circ}C$)
T' – Turbulent Temperature ($^{\circ}C$)
$\overline{T}$ – mean Temperature ($^{\circ}C$)
TKE – Turbulent Kinetic Energy (m^2s^{-2})
Ri_f – Richardson Flux Number (Dimensionless)
u* – Friction Velocity (ms^{-1})
u – East-West component of the horizontal wind (ms^{-1})
u' – Turbulent component of u (ms^{-1})
$\bar{u}$ – mean u (East-West) component of the horizontal wind (ms^{-1})
v – North-South component of the horizontal wind (ms^{-1})
v' – Turbulent component of v (ms^{-1})
$\bar{v}$ – mean of v (ms^{-1})
WAA – Warm Air Advection
w – vertical component wind (ms^{-1})
w' – Turbulent vertical component of the wind (ms^{-1})
$\overline{w}$ – mean vertical component of the wind (ms^{-1})
ws – wind speed (ms^{-1})
wdir – wind direction (°)

θ – Potential Temperature (^{o}K)
σ – Standard deviation
σ_{dir} – Standard deviation of wind direction (^{o})
σ_w – Standard deviation of vertical velocity (ms^{-1})
τ_0 – Surface Stress (m^2s^{-2})

List of Figures

Chapter 1:

Page

Figure 1. Topographic Map of the Fairbanks Area 3

Figure 2. An artwork representation of the drainage flow illustrating the Tanana Valley area and the adjacent Goldstream Valley 9

Chapter 2:

Figure 1. Comparison of collocated in situ radiosonde and remote sensing Doppler sodar vertical profiling of wind speed and wind direction 49

Figure 2. Summary of the ABL and FA winter flow variability wind speed and direction 52

Figure 2. Case I: 23-25 October 2009 56

Figure 3.Case II: 22-24 November 2009 59

Figure 5. Case III: 26-27 January 2010 62

Chapter 3:

Figure 1. Topographic Map of the Fairbanks Area 90

Figure 2. Aerial photo of the UAF-SNRAS campus farm 91

Figure 3. 18 January – January 19 Mean Wind Direction and Wind Speed Evolution 92

Figure 4.7 February Mean Wind Direction and Wind Speed Evolution 93

Figure 5.6 March Mean Wind Direction and Wind Speed Evolution 94

Figure 6. Surface layer turbulent flow for Case I 95

Figure 7. Surface layer turbulent parameters for Case I 97

Figure 8. Vertical structure of the ABL from 18 – 20 January sodar 99

Figure 9. Surface layer turbulent flow for Case II 100

Figure 10. Surface layer turbulent parameters for Case II 102

Figure 11. Vertical structure of the ABL from 7 February sodar 104

Figure 12. Surface layer turbulent flow for Case III 105

Figure 13. Surface layer turbulent parameters for Case III 107

Figure 14. Vertical structure of the ABL from 6 March sodar 109

Figure 15. Vertical Profiles of Case I 110

Figure 16. Vertical Profiles of Case II 112

Figure 17. Vertical Profiles of Case III 114

Figure 18. Sensible Heat Flux for Case I 116

Figure 19. Sensible Heat Flux for Case II 117

Figure 20. Sensible Heat Flux for Case III 118

Chapter 4:

Figure 1. Examples of temperature profiles indicating multiple inversion layers 152

Figure 2a. Temporal series of inversion heights and statistical characterization (INV-1) 153

Figure 2b. Temporal series of inversion heights and statistical characterization (INV-2) 154

Figure 2c. Temporal series of inversion heights and statistical characterization (INV-3) 155

Figure 3. Number of occurrence and cumulative probability density function (CPDF) corresponding to the INV 1, INV 2, and INV 3 temporal series 156

Figure 4. Temporal series of stratified layers within the surface-based inversion 158

Figure 5. Temporal series of stratified layers within the surface-based inversion 159

Figure 6. Statistical characterization of the stratified layers within the surface-based inversion. 160

Figure 7. Statistical analysis of the temporal series of Elevated Inversion (EI) layers during Anticyclone (AC) conditions 161

Figure 8. Statistical analysis of the temporal series of Elevated Inversion (EI) layers during Warm Air Advection (WAA) conditions 162

Figure 9. Statistical analysis of the temporal series of Elevated Inversion (EI) layers during synoptic transients (WAA/AC) 163

Figure 10. Statistical analysis of the temporal series of Elevated Inversion (EI) layers during synoptic transients (AC/WAA) 164

Figure 11. Vertical structure of the atmospheric boundary layer retrieved by monostatic Doppler Phased Array Acoustic Sounder (Sodar Remtech PA-2) from 11 to 13 January, 2010 in Fairbanks, Alaska 165

Figure 12. Thermodynamic structure of the boundary layer retrieved by radiosondes 00 and 12 Z from 11 to 14 January of 2010 at the NWS-PAFA station in Fairbanks, Alaska..... 166

Figure 13. Temperature profiles starting on 27 January at 12 UTC and continuing until 31 January at 00 UTC..... 167

Figure 14. Sodar profiles relative to the turbulence temperature structure coefficient C_T^2 168

List of Tables:

Chapter 2:

Page

Table 1. Absolute error between in situ radiosonde and remote-sensing sodar measurements 65

Table 2. Relative frequency (%) of occurrence of ABL and FA wind speed interval 65

Chapter 4:

Table 1. Number of average radiosonde data points 171

Table 2. Retrieved inversion and stratified layers for radiosonde profiles of 18 Nov 2001 (12Z) and 31 Dec 2009 (00Z) 172

Table 3. Statistical parameters of the temporal series of inversion heights INV-1 to INV-5 during the period Jan. 2000 to Dec. 2010 174

Table 4. Statistical analysis of inversion characteristics 175

Table 5. Statistical indicators of the temporal series of stratified layers 176

Table 6. Statistical parameters describing the elevated inversion (EI) height, depth, strength, and dew point for the EI-1 and EI-2 temporal series 177

Table 7. Comparison of sodar and radiosonde observations RAOBS 178

Table 8. Inversion levels measured by radiosonde profiles 179

Acknowledgments

The author would like to acknowledge his advisor Dr. Fochesatto and his committee members Dr. Nicole Moelders and Dr. Richard Collins from the Department of Atmospheric Sciences, University of Alaska Fairbanks0.

Chapter 1. Introduction

1.1 Lower Atmospheric Circulation and Flow Pattern during the Arctic Winter

The absence of daylight combined with ice and snow-covered surfaces during the extreme winter in Alaska sets up unique meteorological conditions in the lower troposphere where radiative cooling is one of the dominant forcing mechanisms that drive extremely Stable Atmospheric Boundary Layer (SABL) states, particularly under clear skies in the middle of the winter. In these cases, and under weak synoptic flow, the topographic configuration and the orientation of mountains in the Fairbanks area constrain the low-level tropospheric circulation. The air flow in the SABL becomes locally quasi-laminar and regionally stagnant, and is forced mainly by local-scale circulation and radiative cooling.

This meteorological configuration can set up several days of strong stable BLs during which multiple stratified inversion layers develop. The local SABL is prone to strong, continuous radiative cooling, causing stratification to develop in the vertical structure of the SABL, while the upper levels above the SABL are dominated by synoptic flow (Bowling et al., 1968; Benson and Weller, 1970; Beran et al., 1973; Holmgren et al., 1975). Bowling et al., (1968) and Benson and Weller (1970) concluded that radiative cooling and weak synoptic flow are the two main forces in controlling the extreme local temperature lapse rates. Beran et al. (1973) and Holmgren et al. (1975) utilized acoustic sounder interpretation to yield detailed insight into instability layers, the formation and destruction of the inversion layers, and wave activity in the local SABL of the Tanana Valley Basin. Depending upon the synoptic conditions, the flow above the local SABL

may also develop inversion layers with respect to the flow in the SABL; these layers are called elevated inversion (EI) layers. EI layers are discontinuities in air density that occur between the SABL and the free atmosphere (FA), mainly as a function of a specific synoptic flow condition (Mayfield and Fochesatto, 2011).

Fairbanks (64^{o} 49' N, 147^{o} 52' W) is a city that lies within the Tanana River Valley. The city is sheltered by the foothills of the White Mountains to the north (average height of 550 m) and, 60 km to the south, by the Alaska Range (average height of 1000 m). This topographic position, combined with lengthy periods of time in which stagnant conditions prevail, causes anthropogenic pollution to accumulate in the valley; strong stratification and a low-level SABL. The combination of extremely weak winds and the topography within the Tanana Valley limits ventilation of anthropogenic emissions as described above. Temperatures in the cool valleys and north-facing slopes behind Ester Dome and the Cranberry Hills are lower than those in the urban Fairbanks area, causing local-scale flows to develop (Benson, 1965; Benson and Weller, 1970) (See Figure 1). Large cold pools of air that accumulate between Arctic mountains are exposed to higher radiative cooling rates than the air in the main basin (i.e. Tanana Valley), enabling density or drainage flows to develop. These small-scale flows are channeled through the varying terrain morphology and come out into the Tanana Valley, profoundly affect the stability of the surface layer and the micrometeorological flux regimes.

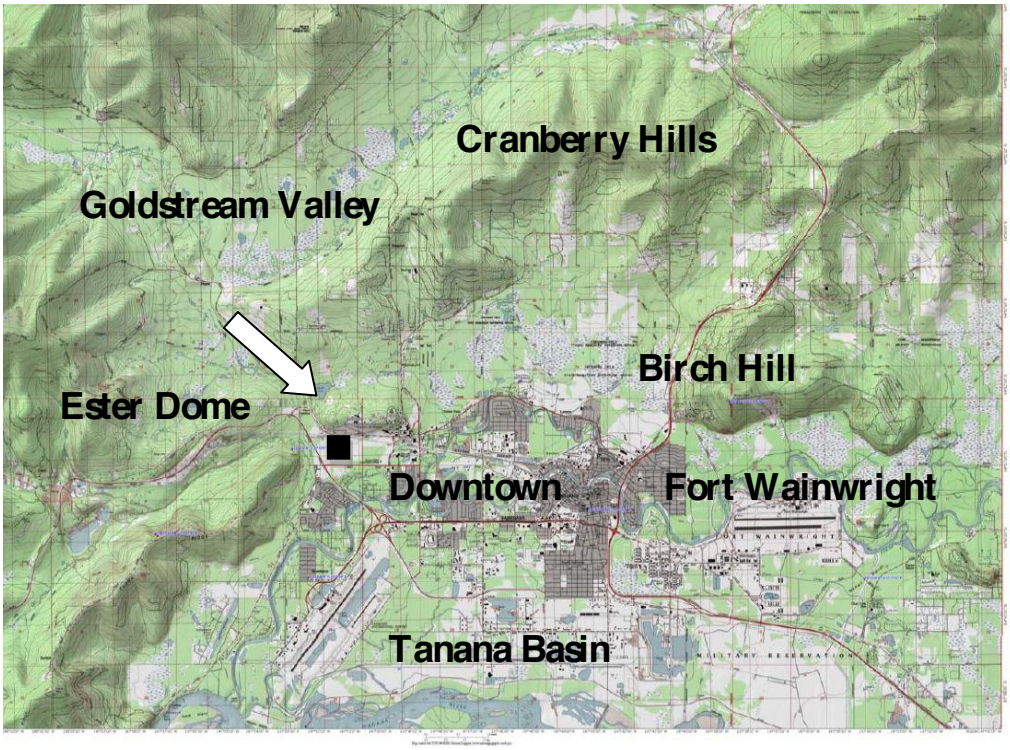

Figure 1. Topographic Map of the Fairbanks Area. '■' represents the Experiment Site. '=>' represents motion of small scale flow.

1.2 High-Latitude Atmospheric Boundary Layer

In the high latitudes, the SABL dominates during mid-winter because of the lack of sunlight (i.e. incoming solar radiation). At Fairbanks, the minimum amount of sunshine on the winter solstice is 3 hours and 11 minutes, while the radiative equilibrium in the stable phase is dominated by long-wave radiation and is established at one hundred of Wm^{-2}. The SABL is therefore fragile and prone to disruptions by different scale-dependent mechanisms, e.g., advections, local flows, drainage flows, and more importantly by long-wave down-welling radiation generated by, for example, low-level cloudiness. Therefore, the study of the SABL needs to be considered within the

framework of complex atmospheric processes acting at different temporal and spatial scales.

In general, the ABL is the portion of the atmosphere in contact with the surface, and it responds to forcing on timescales of minutes to hours. The ABL is bounded by two interfaces. One interface is defined by its interaction and exchanges of energy and matter with the surface. The other interface exists where the BL exchanges energy and matter with the free atmosphere. The ABL depth can vary from hundreds of meters to a few kilometers, depending upon the meteorological conditions, topographic interaction of the flow, location and season, and other parameters (Plate, 1971; Oke, 1978; Stull, 1988; Garratt, 1992; Kaimal and Finnigan, 1994; Blackadar, 1997; Arya, 2001).

The local SABL that occurs during the wintertime in central Alaska has been studied in terms of the synoptic and large scale forcing (Bowling et al., 1968; Benson and Weller, 1970; Wendler and Jayaweera, 1972; Holmgren et al., 1975; Kankanala, 2007; Bourne, 2008; Bourne et al., 2010; Malingowski, 2010). This sub-Arctic SABL develops in space and time mainly due to infrared (IR) radiation loss (i.e., radiative cooling), and turbulent fluxes; however, horizontal advection, when it exists, plays an important role in some specific cases. In particular, under the influence of the continental Arctic airmass, the meteorological conditions are dominated by clear skies, weak winds, and low solar angle. The solar radiation therefore is negligible and the SABL is dominated by IR cooling and turbulent fluxes as mentioned previously. Over a flat surface, the dominant quantities characterizing the surface exchange are represented by the turbulent kinetic energy (TKE), momentum and heat fluxes which under specific and very limited

conditions can be represented in terms of the Monin-Obukbov similarity theory. The local SABL is decoupled from the FA and exchanges of energy and matter are, in this case, limited to altitudes a few hundred meters from the surface. Despite its much shorter vertical development and apparent simplicity, this SABL state is difficult to characterize because of the complexities involved in describing the turbulent fields, identifying the forcing scales, and understanding the functions of the main synoptic and local drivers of this ABL state. The evolution and transitions of the SABL are essentials to understand due to the occurrence and frequency of local and mesoscale flows in the Tanana Valley.

Changes between two well-defined ABL states are called transitions or transitional ABLs. Little is known about turbulent and wave occurrence during a transitional time when the ABL is evolving from one state to the other. Evidence of how this transition occurs has been scarce and is barely addressed in Oke (1978) and Stull (1988). However, focused experiments (Angevine et al., 2001; Fochesatto et al., 2001 a, b) showed that interactions established at the time of the nocturnal-to-diurnal transition are important to consider for exchanges between near-neutral layers and the development of the unstable phase. These transitions are important for describing surface pollutants and noxious gas concentrations in areas of exchange between urban/suburban and continental/maritime air masses. In particular, studies on the extinction of turbulence in upper near-neutral layers as the surface layer proceeds to form the stable phase (Caughey et al., 1979; Duynkerke, 1998; Kolev et al., 2000; Sorbjan, 2006). The transitions in the ABL are key to understand the turbulent processes at the surface and aloft during the

occurrence of drainage flow. The transition and the initial state of the local SABL during the initiation of the drainage flow are considered essential elements of this research.

1.3 Drainage Flow Development and Exchange Processes

Drainage flows manifest as small-scale air motion in the SABL altering the thermodynamic regime of the SABL close to mountains. The dynamics and interaction of drainage flows with the thermodynamic state of the nocturnal ABLs and SABL have been investigated in different field experiments. An early field experiment was conducted in the 1960s on a snow-covered mountain in the Washington state area that measured small-scale downslope flows (Businger and Rao, 1965). Businger and Rao (1965) analysis summarized the local drainage flow from surface measurements and concluded the flow was dominatingly controlled by gravity and buoyancy forces. The experiment was later revisited by Mahrt (1982) who quantified the drainage flow from a dynamic and mathematical point of view. Mahrt (1982) balanced the gravity and the buoyancy forces with the velocity of the flow to quantify the scale and turbulence of the flow.

Hootman and Blumen (1983) and Blumen (1984) studied the frequency and occurrence of drainage flow in Boulder, Colorado under anticyclonic flow with weak pressure gradient forcing (PGF). The drainage flow characteristics in Hootman and Blumen (1983) and Blumen (1984) are similar to the characteristics of outflows from thunderstorms. Outflows from thunderstorms are defined as a cold density flow originating from the downdraft of a thunderstorm. The drainage flow consisted of a turbulent leading edge followed by a steady flow lasting a few hours on average.

Hootman and Blumen (1983) concluded that under specific synoptic situations drainage flows occurred under a weak PGF.

Mahrt et al. (2001) and Soler et al. (2002) investigated the development of a shallow gully drainage flow and its dynamic coupling to the synoptic flow during the Cooperative Atmosphere-Surface Exchange Study (CASES-99) field campaign in Kansas (Poulos et al., 2002). Mahrt et al. (2001) analysis found that cooling in the gully in the early evening lead to negative turbulent heat fluxing in the surface layer. The initial surface cooling forms a SABL and as the evening progressed, the synoptic flow above increases. The increase in velocity in the flow aloft induces downward mixing to break-up the drainage flow in the shallow gully and erodes the SABL. Soler et al. (2002) concluded that the shallow drainage flow is best defined under clear skies condition and weak synoptic forcing. Soler et al. (2002) verified vertical mixing from shallow gully drainage flow defined in Mahrt et al. (2001). When the drainage flow became dynamically unstable, the instability induced turbulence, which mixed warm air and momentum downwards. This process warms consequently the surface air and subsoil temperature. Both of these studies Mahrt et al. (2001) and Soler et al. (2002) concluded that the shallow drainage flow changed the initial conditions in the surface layer, induces mixing with the FA, and erodes the SABL.

A collection of works dealing with gravity flows in nature, Simpson (1982), points out gravity flow in three types of different media: flow from salt water into fresh water, volcanic magma descending down a mountain side, and cold air sinking into a valley from a mountain slope. Taking advantage of the similarities between

hydrodynamic and atmospheric flows, a hydrodynamic tank has been used for extensive investigations of entrainment and mixing of density flow in stratified environments (Baines 2001; 2002; 2005; 2008).

In this study, we concentrated our attention on the interaction between two basins: the Goldstream Valley (colder) and the Tanana Valley Basin (warmer). Figure 2 is an artistic representation of the Tanana Valley and the adjacent northward Goldstream Valley. This figure illustrates the north-south orientation of the inter-basin exchange source for drainage flow development in the Fairbanks area. Generally, the surfaces in both the Tanana Basin and the Goldstream Valley, cools and forms SABLs independently. However, the Goldstream Valley cools at a faster rate due to the lack of sunlight under the shade of the mountain slopes during most of the winter. Therefore, a density difference is created sufficient to cause a local-scale flow between these basins. This local-scale (mountain-valley) flow travels from the surrounding topographical features to affect the Tanana Basin BL as has been investigated in the past (Benson and Weller 1970).

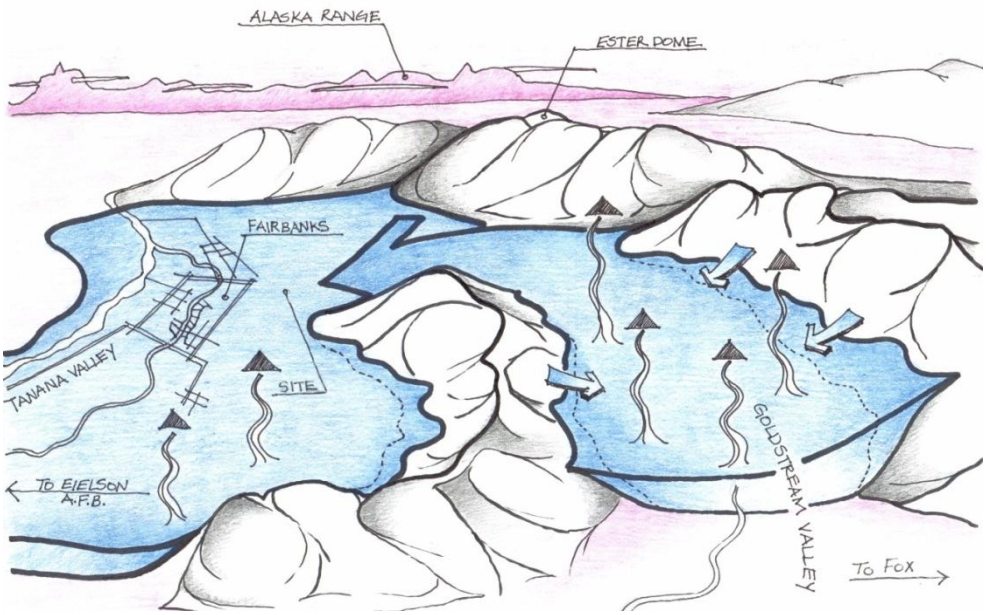

Figure 2. An artwork representation of the drainage flow illustrating the Tanana Valley area and the adjacent Goldstream Valley (the cold air source). Courtesy of Derek Starkenburg, 2011.

1.4 Formulation of the Thesis and Objectives

Wi-BLEx was formulated to study the turbulence and dynamic structure of the wintertime SABL in Fairbanks. A preliminary observational experiment, carried out in the winter from December 2008 to March 2009 at the University of Alaska Fairbanks Campus Farm, collocated a Doppler acoustic sodar and a meteorological mast with two levels at 3 and 10 m using ventilated thermocouples for temperature measurements. This experiment found that the surface layer stratifies when a small scale air flow originates from the northwest to west-northwest penetrated the SABL. This observed process led to

formulate a number of further questions related to the influences of the drainage flow in the winter SABL in the Fairbanks area. Some of these questions are the objective of this thesis as it is detailed as follows:

1. To determine the effect of the drainage flow in the micrometeorological regime of the atmospheric surface layer.
2. To determine the effect of the drainage flow on the turbulent structure of upper ABL levels.
3. To determine what conditions at the synoptic scale may affect the occurrence of drainage flows.

1.5 Organization of the Thesis

This thesis is presented in five chapters. Chapter 1 contains the introduction and the thesis objective. Chapter 2 entitled, "Synoptic Drivers and ABL States", summarizes the results of an intensive observing period during Wi-BLEx 2009-2010. This experiment was devoted to the observation of flows in the Tanana Basin. The experiment was based on simultaneous measurements Remtech PA-2 Doppler Phased Array Sodar collocated to the NWS NOAA station radiosonde launches. This experiment determined the evolution and variability of wind speed and direction in the ABL and in the free troposphere in the Tanana Basin area and compares it with the same information retrieved by radiosonde. A representation of the SABL thermodynamic profile using acoustic backscatter (C_T^2) collocated with thermodynamic in situ radiosonde was obtained during inversion formation and SABL stratification. This study verified that during radiational cooling and

in the absence of significant advection the formation of stratified layers corresponds to enhancements in the (C_T^2) backscattering profiles.

Chapter 3, entitled "Micrometeorological Effects of Drainage Flow on the winter Atmospheric Boundary Layer", presents observational evidence of mixing followed by stratification in the SABL due to the penetration of small scale drainage flows during Wi-BLEx 2009-2011. This experiment was carried out at the University of Alaska Farm close to the foothills surrounding the Tanana Valley basin. Three case studies are presented illustrating the distinctive pattern of the drainage flow penetration and its influences on the surface layer turbulent regime is discussed as well as the changes in the turbulent and dynamic structure of the SABL. This study uses local and basin scale surface turbulence measurements by sonic anemometers and laser scintillometry respectively to determine the turbulent sensible heat fluxes, combined with vertical profiling of thermal turbulence and dynamic flows in the SABL by Doppler Phased Array Sodar. The case study spans over the deep winter with no diurnal cycle illustrating a sustained drainage flow (18 January – 19 January 2011) and intermittent drainage flow (7 February 2011) and late winter representing drainage flows in conditions of diurnal cycle (6 March 2011).

Chapter 4, "Influence of Synoptic Meteorology on the Occurrence of the Small Scale Flow", summarizes a study of synoptic flows and their thermodynamic features as precursor for the occurrence of drainage flow. Although the typical conditions of drainage flow formation are known, this study performed a historical ten years analysis of the radiosonde data base for the Fairbanks PAFA to determine the layered structure of the

winter ABL to infer possible dynamic-radiative mechanisms favoring the occurrence of drainage flows. A numerical algorithm was developed to detect and discriminate all inversion levels presents in the radiosonde thermodynamic profile. This study found a high frequency of occurrence of the so-called local and synoptically-controlled inversions and classified their formation mechanism. Combining this analysis with Wi-BLEx observations of simultaneous multiple inversions levels this thesis elaborates and gives observational evidence of occurrence of radiative-dynamic coupling between EIs with the locally controlled inversions. Future research combining more observational and modeling tools will be needed to assess the extent of this coupling process in terms of ABL exchange processes.

Chapter 5, “Thesis Summary and Research Perspectives”, summarizes the main results obtained during Wi-BLEx related to the micrometeorological influences of small scale drainage flows in the winter SABL as well as the role of the synoptic meteorology and possible driver of radiative-dynamic coupling at the local SABL. Suggestions for future research to investigate the turbulent scales interaction, the atmospheric coupling at different scale levels and their effect on the SABL are proposed.

1.6 References

Angevine, W., H. Baltink, and F. Bosveld, 2001: Observations of the Morning Transition of the Convective Boundary Layer. *Boundary-Layer Meteorol.* **101**, 209-227.

Arya, S.P.S., 2001: Introduction to Micrometeorology, 2nd Ed. Academic Press. San Diego, CA

Baines, P.G., 2001: Mixing in flows down gentle slopes into stratified environments. *J. Fluid. Mech.* **443**, 237-270.

Baines, P.G., 2002: Two-dimensional plumes in stratified environments. *J. Fluid. Mech.* **471**, 315-337.

Baines, P.G., 2005: Mixing regimes for the flow of dense fluid down slopes into stratified environments. *J. Fluid. Mech.* **538**, 245-267.

Baines, P. G., 2008: Mixing in Downslope Flows in the Ocean - Plumes versus Gravity Currents. *Atmos. Ocean.* **46**, 405-419.

Benson, C.S., 1965: *Ice Fog: Low Temperature Air Pollution, Defined with Fairbanks, Alaska as Type Locality.* College, Alaska: University of Alaska Fairbanks, Geophysical Institute, pp: 134.

Benson, .C.S. and G. Weller, 1970: A Study of Low-Level Winds in the Vicinity of Fairbanks, Alaska. Report to Earth Resources Co., Geophyiscal Institute, University of Alaska.

Beran, D., W. Hooke and S. Clifford, 1973: Acoustic Echo-Sounding Techniques and their Application to Gravity-Wave, Turbulence, and Stability Studies. *Boundary-Layer Meteor.* **4**, 133-153.

Blackadar, A.K., 1997: Turbulence and Diffusion in the Atmosphere. Springer-Verlag. New York.

Blumen, W., 1984: An Observational Study of Instability and Turbulence in Nighttime Drainage Winds. *Boundary-Layer Meteor.* **28**, 245-269.

Bourne, S., 2008: A Climate Perspective of Observed and Modeled Surface-Based Temperature Inversions in Alaska. MS Thesis, Department of Atmospheric Sciences, University of Alaska Fairbanks, Fairbanks. Available at: http://ffden-2.phys.uaf.edu/atm/Students/theses/Bourne_SM.pdf, pp. 106.

Bourne S.M., U.S. Bhatt, J. Zhang, and, R. Thoman, 2010: Surface-Based Temperature Inversions in Alaska from a Climate Perspective. *Atmos. Res.* **95**, 353-366.

Bowling, S.A., T. Ohtake, and C.S. Benson, 1968: Winter pressure systems and ice fog in Fairbanks, Alaska. *J. Appl. Meterorol.* **7**, 961-968.

Businger, J.A. and K.R. Rao,1965: The formation of drainage wind on a snow-dome. *J. Glaciol*. **5**, 833-841.

Caughey, S. J., J.C. Wyngaard, and J.C. Kaimal, J. C. 1979: Turbulence in the Evolving Stable Boundary Layer. *J. Atmos. Sci*. **36**, 1041-1052.

Duynkerke, P.G., 1998: Turbulence, Radiation and fog in Dutch Stable Boundary Layers. *Boundary-Layer Meteorol.* **90**, 447-477.

Fochesatto, J., P. Drobinski, C. Flamant, D. Guédalia, C. Sarrat, P.H. Flamant, and J. Pelon, 2001a: Observations and modeling of the atmospheric boundary layer nocturnal-diurnal transition during the ESQUIF experiment. *Advances in Laser Remote Sensing*, Dabas, A., C. Loth, and J. Pelon, Eds., Ecole Polytechnique Editions, Paris, France, 439-442.

Fochesatto, J., P. Drobinski, C. Flamant, D. Guédalia, C. Sarrat, P. Flamant, and J. Pelon, 2001b: Evidence of dynamical coupling between the residual layer and the developing convective boundary layer. *Boundary-Layer Meteorol.,* **99**, 451-464.

Garratt, J.R., 1992: The Atmospheric Boundary Layer. Cambridge Atmospheric And Space Science Series, Vol. 1. Cambridge University Press, Cambridge, New York

Holmgren, B., L. Spears, C. Wilson, and C.S. Benson C.S., 1975: Acoustic Soundings of the Fairbanks Temperature Inversions. *Climate of the Arctic: Proceedings of the AAAS-AMS conference, Fairbanks, Alaska. 1973. Weller, G. and S.A. Bowling, Eds., Geophysical Institute, University of Alaska,* 293-306.

Hootman, B.W. and Blumen W., 1983: Analysis of Nighttime Drainage Winds in Boulder, Colorado during 1980. *Mon. Wea. Rev.* **111**, 1052-1061.

Kaimal J.C. and J.J. Finnigan, 1994: Atmospheric Boundary Layer Flows: Their Structure and Measurement. Oxford University Press.

Kankanala, P. K. R., 2007: Doppler Sodar Observations of the Winds and Structure in the Lower Atmosphere Over Fairbanks, Alaska. MS Thesis, Department of Atmospheric Sciences, University of Alaska Fairbanks, Fairbanks.. Available at: http://ffden-2.phys.uaf.edu/atm/Students/theses/Pavan_thesis.pdf, pp. 65.

Kolev, I., P. Savov, B. Kaprielov, O. Parvanov, and V. Simeonov, 2000: Lidar observation of the nocturnal boundary layer formation over Sofia, Bulgaria. *Atmos. Environ.* **34** , 3223-3235.

Mahrt L., 1982: Momentum Balance of Gravity Flows. *J. Atmos. Sci.* **39**, 2701-2711.

Mahrt L., D. Vickers, R., Nakamura, M.R. Soler, J.L. Sun, S. Burns, and D.H. Lenschow 2001: Shallow drainage flows. *Boundary-Layer Meteorol.* **101**, 243-260.

Malingowski, J., 2010: An observational study of the surface-based radiation temperature inversion in Fairbanks, Alaska. MS Thesis, Department of Atmospheric Sciences, University of Alaska Fairbanks. Available at: http://ffden2.phys.uaf.edu/atm/Students/theses/JMalingowski_ MSthesis_ 2010.pdf, pp. 91..

Mayfield, J. and G.J. Fochesatto, 2011: The Layered Structure of the Winter Atmospheric Boundary Layer in the Interior of Alaska. *J. Appl. Meteorol. Clim. Submitted October 2011. In Review*.

Oke, T.R., 1978: *Boundary Layer Climates*. Methuen & Co. Ltd. London, UK. pp: 434.

Plate, E.J., 1971: Aerodynamic Characteristics of Atmospheric Boundary Layers. U.S. Atomic Energy Commission, Division of Technical Information [available from National Technical Information Service, U.S. Dept. of Commerce, Springfield, Va.] pp. 190.

Poulos G.S., W, Blumen, D. C. Fritts, J. K. Lundquist, J. Sun, S. Burns, C. Nappo, R.M. Banta, R.K. Newsom, J. Cuxart , E. Terradellas, B. Basley, M. Jensen, 2002: CASES-99: Comprehensive Investigation of the Stable Nocturnal Boundary Layer. *Bull. Amer. Meteor. Soc.* **83**, 555-581.

Simpson, J.E., 1982: Gravity Currents in the Laboratory, Atmosphere, and Ocean. *Annual Review of Fluid Mechanics*. **14**, 213-234

Soler, M.R., C. Infante, P. Buenestado, and L. Mahrt., 2002: Observations of Nocturnal Drainage Flow in a Shallow Gully. *Boundary-Layer Meteorol.* **105**, 253-273.

Sorbjan, Z., 2006. Local Structure of Turbulence in Stably Stratified Boundary Layers. *J. Atmos. Sci.* **63**, 1526-1537.

Stull, R. 1988: An Introduction to Boundary Layer Meteorology. Kluwer Academic Publishers. Dordrecht, Netherlands.

Wendler, G and K.. Jayaweera, 1972: Some measurements of the development of the surface inversion in Central Alaska during winter. *Pure and Applied Geophysics*. **99**, 209-221.

Chapter 2: Flow Variability and the Atmospheric Boundary Layer Structure during Winter in the Interior of Alaska[1]

2.1 Abstract

In the framework of the Winter Boundary Layer Experiment in Fairbanks, Alaska (2009-2011) an intensive observing period was dedicated to document the flow variability and the atmospheric boundary layer (ABL) structure by means of thermodynamic radiosonde observations collocated with a monostatic Phased Array Doppler Sodar, hereafter referred as sodar (sound detection and ranging). Fifty-six cases were selected representing the transition to winter (October to November, 2009) and middle of the winter (January to February, 2010). It was found that wind speed and direction measured by the radiosonde and sodar fully overlaps within $\pm$ 2σ in $\pm$ 3 hr interval at 00 and 12 UTC for all synoptic and free atmosphere conditions.

The flow variability was deduced by combining both observational platforms. The results were clustered by synoptic meteorological condition. The ABL wind speed and direction in anticyclone conditions were found to be 2.6 $\pm$ 0.4 ms^{-1} ($138^o \pm 77^o$) while for cyclone conditions they were 5.0 $\pm$ 0.6 ms^{-1} ($156^o \pm 13^o$). In the case of synoptic transients (i.e., Arctic front, low-level jets), the wind speed and direction were found to be 3.3 $\pm$ 0.4 ms^{-1} ($144^o \pm 56^o$). The C_T^2 sodar profile was observed to reproduce the thermodynamic structure of the ABL. And, under specific synoptic conditions, a good

---

[1] Mayfield J. and G. J. Fochesatto, 2011. Flow Variability and the Atmospheric Boundary Layer Structure during Winter in the Interior of Alaska. Preparation for submission *Journal of Applied Meteorology and Climate*

agreement was found between sodar methodologies for ABL detection and the thermodynamic radiosonde profile.

2.2 Introduction

During winter in interior Alaska the structure of the Atmospheric Boundary Layer (ABL) remains in a stable phase for long periods (days and weeks) and is not affected by the diurnal cycle. A near-neutral state and quiescent flows in the ABL are not uncommon, and can occur under weak pressure gradient forces or when the synoptic flow pattern is changing. One remarkable characteristic of the ABL at high latitude, particularly in sub-Arctic interior Alaska, is, in the absence of sunlight, a surface-based inversion forms over ice and snow-covered surfaces, driven by strong surface radiative cooling (Bowling et al., 1968; Andre and Mahrt, 1982; Hartmann and Wendler, 2005; Mayfield and Fochesatto, 2011).

Changes in the ABL state during mid-winter are basically driven by well-defined synoptic situations. One such situation is the anticyclone (i.e., Siberian High and Canadian High) that imposes a strong radiative cooling rate and therefore a deficit of surface net radiation under clear skies (Wexler, 1941; Bowling et al., 1968; Andre and Mahrt, 1982), resulting in the formation of strongly-stratified ABLs. The opposite situation is found during synoptic transients when, for example, the Arctic front migrates northward bringing cyclonic activity (i.e., a warm and moist air mass) to interior Alaska (Willis and Grice, 1977). This meteorological configuration introduces a dynamic-radiative coupling that forces the surface net radiation to rise to near equilibrium, or reach positive values. This warming of the surface is a well-known feature in the Arctic and is

manifested by a lifting of the ABL structure that erases surface stratification when the cyclone structure is fully established (Mayfield and Fochesatto, 2011). On the other hand, a different ABL state is present under a weak pressure gradient force (PGF) at the synoptic scale. The weak PGF establishes quiescent flows (extremely low flow speeds of ≤ 1 ms^{-1} in the ABL) and under these conditions stratification can be initiated in the ABL from negative heat fluxes from the ground. Close to the mountain slopes stratification can also occur when local drainage flow dominates the ABL circulation. This weak synoptic forcing situation enables the local topography which shelters the Fairbanks area to control the ABL circulation and determine specific thermodynamic structures (i.e., surface stratification and increase of turbulent heat fluxes towards the surface (Wendler and Jayaweera, 1972). Conversely, under a strong PGF a larger meso-synoptic structure is established. This structure can develop, for example, a low-level jet when the Arctic front moves northward. The movement of the Arctic front warms the low levels modifying the ABL thermodynamic structure (Willis and Grice, 1977; Mayfield and Fochesatto, 2011).

In this context, the ABL is characterized by an atmospheric flow that can range widely. Low-speed winds (e.g., <1.0 ms^{-1}) are locally quasi-laminar, meandering in direction, regionally stagnant forced by local-scale circulation, and prone to strong radiative cooling (Wexler, 1941; Bowling et al., 1968; Benson, 1969; 1970 a, b; Benson and Weller 1970). In contrast, strong flows may develop on top of the ABL, shaped by the development of low level jets (wind speed >10 ms^{-1} in some cases). In the former case, the ABL structure is characterized by the formation of a strong surface-based

inversion (SBI) forced by negative surface net radiation balance which decouples the ABL flow from the rest of the atmosphere (Wexler, 1941; Andre and Mahrt, 1982). This ABL configuration places severe restrictions on air pollution dispersion due to the increasing effectiveness of the ABL at trapping pollutants and infrared (IR) active gases. These emissions, which originate in urban areas in a stratified ABL, cause an increased concentration of pollutants and noxious gases and give rise to dangerous air pollution events that can last for several days (Benson, 1969, Benson and Weller, 1970; Reichardt and Reidy, 1980). On the other hand, the latter case gives rise to the advection of warm air on top of the ABL which will, in turn, change the surface radiation balance, erasing local stratification and lifting the inversion. This dynamic situation, in which pollutants from different emission sources mix (i.e., car exhausts and home heating sources and power plants emissions), introduces an important uncertainty in the source apportionment of contaminants and important particulates when assessing an air pollution problem.

In the case of an ABL dominated by quiescent flows, the formation of a single inversion layer or stratified inversion layers can also be disrupted by changes in the wind direction and/or acceleration of the flows in the lower troposphere (Wendler and Jayaweera, 1972). Similarly, interaction of flows at different scales in the ABL is particularly noticeable when, for example, the structure of the stable stratified ABL is thermodynamically transformed by warm air advection which introduces an elevated inversion that brings warm and moist air to heights of ~ 1 to 2 km (Willis And Grice, 1977; Mayfield and Fochesatto, 2011). The radiative coupling of the upper air layer to the ABL flow will ultimately warm the surface, overriding the thermal stratification in the

ABL. Similarly, a low-level jet driven by a northward-moving Arctic front can develop strong wind speeds >10 ms^{-1} above the ~925 hPa ABL level, causing low-level warming and changing the ABL structure (Willis and Grice, 1977; Hartmann and Wendler, 2005; Mayfield and Fochesatto, 2011).

Based on the local and synoptic drivers of ABL states at high latitude in interior Alaska as described, this paper investigates the statistical configuration of wind speed and direction profile structures and their variability in the ABL and in the free atmosphere (FA). The thermodynamic ABL state under specific flow conditions was determined using acoustic backscatter (C_T^2) profiling. The C_T^2 profiles were analyzed, and their variability was related to the flow and thermodynamic configuration of the ABL.

This article is organized as follows: section 2 describes the methodology and the retrieved data base profiles, and presents a side-by-side comparison of direct wind speed and direction measurements by an in-situ radiosonde system and remotely-sensed wind speed and direction profiles retrieved by the sodar instrument. Section 3 presents the analysis of flow variability in the ABL and in the FA in terms of wind speed and direction, clustered by synoptic periods using sodar data. Section 4 presents the ABL structure in specific synoptic situations and the corresponding morphology and variability of C_T^2. Section 5 summarizes a discussion of the observational results in terms of ABL states and the effect and influence of synoptic flows on ABL thermodynamics of interest in mesoscale modeling of a stable ABL and in the study of air pollution meteorology at high latitudes.

2.3 Methodology

The intensive observing period (IOP) within the Winter Boundary Layer Experiment (Wi-BLEx) took place in Fairbanks, Alaska in two different periods: transition to winter, October-November, 2009, and mid-winter, January-February, 2010. The radiosonde launches were conducted regularly (00 and 12 UTC) by the National Weather Service – National Oceanic and Atmospheric Administration (NWS-NOAA) PAFA (70261) service station in Fairbanks. A Phased Array Doppler Sodar Remtech PA-2 (sodar) was collocated to the radiosonde launches.

The sodar (Remtech PA2) remotely sense the atmosphere by emitting acoustic tone pulses of 200 msec duration at up to five frequencies around 2.25 kHz with a pulse repetition period larger than ten seconds. The instrument's monostatic antenna contains 196 speakers distributed in four blocks totaling 1.3 m x 1.3 m covered by an acoustic cuff. The antenna is switched sequentially between emission and reception modes.

The sound pulse transmitted by the sodar is backscattered continuously from the atmosphere; the sound wave time-of-flight back to the antenna indicates the height at which the backscatter occurred. The background noise is measured and subtracted automatically by means of four speakers working continuously in receiver mode localized at each corner of the instrument's antenna.

The backscattering intensity depends on the turbulent structure of the ABL. Higher intensities are received from layers of strong, thermally-driven turbulence or from layers with enhanced mechanical turbulence (e.g., wind shear); lower intensities are associated with weak turbulence levels associated with near-isothermal layers. Thus, the

power of the backscattered signal is the un-calibrated coefficient of temperature turbulence structure (C_T^2) and is a relative measure of small-scale air temperature fluctuations **(**Gilman et al., 1946; McAllister et al., 1969; Brown and Hall, 1978; Coulter and Kallistratova, 2004; Remtech, 2011).

The components of the three-dimensional wind field (u, v, w) are derived by measuring the frequency shift of the backscattered acoustic pulse due to the Doppler Effect **(**Coulter and Kallistratova, 2004**)**. In order to achieve the wind measurement, the PA2 sodar electronically controls the speakers in such a way that the sound waves generated are phased to the intended direction via acoustic wave interference. Vertical emission is achieved when all speakers emit in phase, while tilted beams (max. 30° from the vertical) are achieved by internally phasing the array of speakers. Thus the horizontal wind components (u, v) are calculated from the frequency shifts of the signals backscattered from tilted beams, and the vertical velocity (w) from that of the vertical beam. In order to compensate for the temperature dependence of the speed of sound, the emission frequencies are automatically adjusted to temperature changes and the backscattered beam is corrected by spherical solid angle, although it is not corrected for water vapor attenuation. The information obtained from sodar is averaged in space and time, providing continuous information about wind speed, average direction, and fluctuations and turbulence structure in the lowest few hundred meters of the ABL during an integration period of minutes. The sodar used in this work determined the vertical ABL structure during the extreme Fairbanks, Alaska winter at temperatures ranging from

0 to -35 ^{o}C and gave an operative range of from 20 m to 400 m at 5-10 min integration time for semi-continuous operations.

This instrumentation has been successfully used in experiments to study ABL structure (Neff, 1980 a, b; 1986; Neff and King, 1987; Drobinski et al., 1998; Dupont et al., 1999) and flows and to relate these fields to scale-averaged turbulent fluxes to validate large-scale circulation models (Neff, 1980 a, b; Menut, 1997; Menut et al., 1999). These instruments are also used for operational support in international airports to identify the presence of vortices and turbulence during operations, in monitoring pollution dispersion in nuclear power plants, and in monitoring urban and suburban ABL heights for air-pollution studies (Dupont et al., 1999). In these studies the backscatter echo was related to atmospheric structures as interpreted from the backscattering signals to determine the evolution of the nocturnal ABL, the temporal variation of ABL height during the day, the presence of convective cells, and the secondary circulation in the ABL (Drobinski et al., 1998). Determining atmospheric stability by directly measuring temperature fluctuations has been correlated with sodar profiles (von Gogh and Zib, 1978; Beyrich and Weill, 1993; Singal, 1997). In studies of the nocturnal ABL using collocated radiosonde and sodar and under prevalent light wind over flat terrain that experienced strong surface nocturnal cooling, the sodar profiles were related to increasing atmospheric stability (Parry et al., 1975; Holmgren et al., 1975; Tyson and von Gogh, 1976, von Gogh and Zib, 1978).

On the other hand, sodar has been used to determine ABL wind profile structures over an extended period of time Seibert (1998) and Baumann and Piringer (2001) to help

calibrate and validate dispersion models. At high latitudes, however, past ABL experiments using sodar detailed stably-stratified structures, wave activity, multiple stratification levels, and stability changes with height under strong surface stratification (Beran et al., 1973; Holmgren et al., 1975; Cheung, 1991; Anderson, 2003). A comprehensive review highlights the importance of sodar in retrieving both the thermodynamic and the dynamic structure of the ABL, and can be found in Brown and Hall (1978). A more recent comparison and review summarizes current sodar technologies in Crescenti (1997) and Coulter and Kallistratova (2004)**.** A consistent relationship between the acoustic reflectivity and the ABL structure was presented in Dimitrios (1990) and later on in Menut (1997).

As mentioned in section 1, the ABL in sub-Arctic interior Alaska responds to the combined action of specific synoptic pattern, local flows, and surface radiative and turbulent fluxes. In order to better understand this complex relationship between local and non-local variables and their influence on the ABL, an assessment of the collocated measurements was first conducted during Wi-BLEx to determine the reliability and representativeness of the remote-sensing acoustic profiler measurements in terms of the in-situ radiosonde measurements. To ensure minimum possible differences in observing the ABL structure and flows, both instruments were located in a common atmospheric volume at the radiosonde launch site operated by the NWS-NOAA in Fairbanks. Two period of observation were performed: October to November 2009 and January to mid February 2010. The sodar-retrieved wind profile accuracy was $\pm$ 0.2 ms^{-1} for wind speed and $\pm$ 3° for wind direction according to Remtech (2011). Other studies providing

accuracies and precision using similar instrumentation can be found in: Chintawongvanich et al. (1989), Grant (1994), Seibert (1998), and Baumann and Piringer (2001).

Specific cases have been selected to assess the performance of both instruments under the most relevant and well-defined atmospheric situations. Figure 1 details the radiosonde and sodar profiling of wind speed (left panels) and wind direction (right panels). Superimposed on the in-situ radiosonde measurements are the sodar-retrieved average profile collected over an interval of $\pm$ 3 hrs centered in the radiosonde launch and, in the shaded area, the profile measurement variability bounded by $\pm$ 2σ. Figure 1a illustrates the case of a low-level jet that developed wind speed higher than 5 ms^{-1}. Figure 1c shows a profile of wind speed lower than 3 ms^{-1} under surface snow conditions and in the presence of fog. Figure 1e presents a wind speed profile under clear-sky conditions.

Figure 1a illustrates the case of 23 October 2009 at 00 UTC. The ABL is in the presence of a low-level jet aimed by a strong PGF established in interior Alaska according to the NWS meteorological charts. The structure of the flow indicates a wind speed maximum determined using sodar profiling at ~350 m height, while radiosonde measurement detects the wind speed maximum at ~410 m. A maximum in the wind speed profile was also measured by the radiosonde at 7.1 ms^{-1} at a height of 410 m and the same 7.1 ms^{-1} speed was detected by sodar measurements at 410 m. In this particular case, the in situ measurements by radiosonde verified a 300 m gap between points which renders these measurements insufficient for determining flow structure.

Figure 1c shows the case of 1 February 2010 at 12 UTC. On-site observations showed low wind speed, light snow, and fog conditions near the experimental site. The ABL wind speed measured by the radiosonde was greater than 2 ms^{-1} and the sodar wind speed measured over 72 profiles corresponding to $\pm$ 3 hrs averaged above 3 ms^{-1}. The radiosonde sample showed a wind speed of ~1.5 ms^{-1} at 700 m, while sodar measurements provide a more detailed wind speed structure.

Figure 1e presents the case on 3 February 2010 at 12 UTC. Wind profile measurements showed the presence of a high-pressure system in interior Alaska, according to 6-hour NWS meteorological data, with decreasing PGF. Wind speed in the ABL was higher than 1.5 ms^{-1} according to sodar and radiosonde measurements below 200 m. Close to the surface, at approximately 50 m height, the observed flow variability within $\pm 2\sigma$ is 0.5 ms^{-1} while the closest radiosonde measurement is at ~40 m and gives a wind speed of 1 ms^{-1}. On-site reported observations indicate the presence of broken fog at 200 m height at 00 UTC and throughout the following 3 hrs with flow variability below 0.5 ms^{-1} and mean wind speed below 3 ms^{-1} in the ABL.

A quantitative assessment of the instrument comparison is summarized in Table I; there, the maximum absolute error per radiosonde point and the sodar mean and standard deviation are presented for comparison with current operational techniques from the profiles illustrated in Figure 1 (See Figure 1 and Table 1).

2.4 Flow Variability

The flow structure in the ABL and the FA was studied in the two Wi-BLEx IOPs. Statistical parameters were obtained to characterize flow variability under specific

synoptic conditions. The procedure used for this analysis began with identifying the ABL height (h) using the thermodynamic radiosonde. The sodar data were then grouped into intervals of $\pm$ 3 hrs centered on the radiosonde launch and $\pm$ 200 m below and above the actual value of h. From a total number of 87 cases in which the ABL presence was verified, 56 measurement cases were used to determine the variability of the sodar wind speed and wind direction under specific synoptic conditions. The boundary layer was identified through the thermodynamic profile from the radiosondes during the study period. The statistical analysis was grouped into the two temporal periods described in the following paragraphs.

2.4.1 Period I: October to December 2009

2.4.1.1 Period I-I: 11 to 18 October 2009

During 13 October 2009, a well-developed surface high pressure was localized in central Alaska. Sodar measured an average 6 hr ABL wind speed of ~3 ms^{-1} with $\sigma < 1$ ms^{-1} of variability. The ABL wind direction variability was less than 90° and decreased over time (See Figures 2a, 2b). Throughout the selected period a north-south stationary front moved through central Alaska without changing the ABL wind speed appreciably, but constraining the wind direction variability.

2.4.1.2 Period I-II: 13 to 25 October 2009

A surface low-pressure system was centered over the northern portion of the Aleutian Islands; the associated warm front remained south of the Fairbanks region, and a strong PGF developed in central Alaska. This synoptic situation resulted in a mean ABL wind speed that was variable within 3 – 5 ms^{-1} at $\leq$400 m height, and a flow direction

from the east veering to the southeast with a maximum amplitude variation less than 10°. However, the FA mean wind speed of 6 ms^{-1} – 7 ms^{-1} (Figures 2C and 2D) was larger than that in the ABL, and the mean FA wind direction was from the south-southeast. The first period of measurement in the ABL on October 18, 12 UTC shows a 3 ms^{-1} (east-southeast) wind speed and later on a sudden jump to ~4 ms^{-1} (east-northeast) was detected, confirming the presence of a strong PGF at a regional level.

2.4.1.3 Period I-III 1 to 8 November 2009

The Arctic Front was located in the south sector of continental Alaska, along the Alaskan coastline. Throughout this period the PGF in continental Alaska was building and the ABL wind speed increased from 2.5 ms^{-1} to 5 ms^{-1} on average, while the FA wind speed increased from 3.2 ms^{-1} to 7 ms^{-1}. Furthermore, when the PFG was established in interior Alaska the wind direction variability became confined to the northeast sector (45°) indicating the presence of an Arctic air mass (see Figures 2C and 2D).

2.4.1.4. Period I-IV 20 to 24 November 2009

During this period, the mean ABL wind speed ranged from 2.5 ms^{-1} to 4 ms^{-1}. The wind speed fluctuated from a maximum value of 2 ms^{-1} to less than 1 ms^{-1}, and wind direction variability was < 67.5°. The mean wind direction in the ABL flow was from the east, changing to the south-southeast and returning back to the southeast during the period I-IV (See Figures 2a and 2b). At the same time, a surface high was present in interior Alaska; a low-pressure system in the Gulf of Alaska grew stronger, increasing the PGF, and the wind direction remained variable while wind speed steadily decreased throughout this period.

2.4.2 Period II: January to February 2010

2.4.2.1 Period II-I 10 to 17 January 2010

A surface low-pressure system was centered south of the Gulf of Alaska and a surface high-pressure system was centered over the northern coast of Alaska and the northern part of the Northwest Territories. In interior Alaska the PGF was strong and sustained throughout this period. At the beginning of the period under study the wind direction in the ABL was from the northeast; as the period progressed it changed to the southeast. Wind direction variability was less than 10°. The wind speed in the ABL ranged from 3-7 ms^{-1}, forced by the presence of the PGF (see Figures 2a and 2b). Conversely, the FA flow direction was east to east-southeast at highly variable wind speeds in the range of 3 ms^{-1} to 9 ms^{-1} (see Figure 2c and 2d).

2.4.2.2 Period II-II 21 to 24 January 2010

A surface low-pressure system was centered in the Gulf of Alaska; a weak pressure gradient existed over Fairbanks, combined with a surface high-pressure system to the northeast. During 21 to 24 January 2010 the mean ABL wind speed decreased from 4 ms^{-1} to ~2 ms^{-1} and the standard deviation decreased from 2 ms^{-1} to less than 1 ms^{-1} (Figure 2a and 2b). The mean FA wind speed also decreased from 4 ms^{-1} to less than 2 ms^{-1}. This dynamic configuration is a characteristic of a synoptic forcing that indicates an anticyclone system in interior of Alaska. The FA and ABL wind profiles exhibit the same characteristic of meandering, weaker winds with speed <3 ms^{-1} (see Figure 2c and 2d).

2.4.2.3 Period II-III: 31 January to 7 February 2010

The ABL wind speed was verified to be variable and lower than 2 ms^{-1} with a standard deviation less than 1 ms^{-1}. The mean wind direction changed from the south to the southeast during the period under consideration. The ABL wind direction variability was calculated to be ~67.5° throughout the measurements period. The Aleutian Low moved northward during this time (see Figures 2a and 2b).

Figures 2 (a-d) illustrates that the October to November 2009 transition to the winter period was characterized by significant synoptic activity as demonstrated in the wind speed and direction data. Conversely, in the central winter period from January to February 2010, the lapse time between synoptic changes (i.e., changes between different synoptic states, including cyclonic, transient, and anticyclone forcing) is longer than in the previous October – November 2009 period and the wind speed variability is less. Moreover, according to Table II, the wind speed variability data collected within the ABL during the six-hr evaluation period centered on the radiosonde launch showed that 36.5 % of the stable ABL wind was $\leq$ 3.0 ms^{-1} and 34.8 % of the ABL wind speed was below $\leq$ ms^{-1}. This result indicates that under a synoptic high-pressure system in central Alaska the ABL winds were stagnant in the presence of a stable ABL. In the FA, however, during the study period under inversion conditions, 44.5 % of all measured wind speeds exceeded 5 ms^{-1}. In summary, the anticyclone period from 21 to 24 January 2010 was characterized by low wind speed (< 3 ms^{-1}) and high wind direction variability. At the other extreme, the case in which a strong PGF was identified from 23 to 25 November 2010 saw increased wind speed and wind direction that was confined to a very

low range of variability. During the cyclonic event from 10 to 17 January 2010 the wind speeds in both the ABL and the FA were > 3 ms^{-1} and the wind direction variability was < 10°. (See Table 2)

2.5 ABL Structure

This section presents the ABL structure measured by continuous sodar operation under the conditions of the synoptic periods described in section 3. To perform this study, combined sodar and radiosonde observations were used to relate ABL thermodynamics to the morphology of acoustic backscattering. ABL h and evolution were calculated based upon referred methodology by Beyrich and Weill (1993), and applied only under very specific flow situations.

ABL h can be defined as the height of the atmosphere at which turbulent transfers of heat, mass, and momentum are produced. Based upon the mechanism that dominates during stable ABL formation, ABL h can best be described as: 1) the height at which ABL winds reach maximum. This is the case when the ABL forms in the presence of a jet without significant advection of synoptic origin (Clarke, 1970); 2) the height at which the vertical temperature gradient becomes isothermal (Melgarejo and Deardorff, 1975); 3) The height at which the vertical potential temperature gradient becomes adiabatic (Melgarejo and Deardorff, 1975); 4) the height at which the turbulent kinetic energy flux becomes negligible compared with values at the surface (Businger and Arya, 1975); and 5) the height at which the winds become geostrophic (Mahrt et al., 1979). According to experimental work (Founda et al., 1997), ABL h was determined with much more confidence whenever wind profile measurements are available, while others Beyrich and

Weill (1993) and Menut (1997) found a weak correlation when determining the ABL height by applying methodologies 1, 2, and 3 described above. On the other hand, prognostic equations based on similarity theory have been present in the literature since the late 1970s; applying these methods requires surface turbulent fluxes and tower meteorological input. Instead, sodar determination of the stable ABL h is based on finding the maximum negative slope of the acoustic backscattering profile. This point indicates a height in the atmosphere after the maximum of backscattered signal where the thermal turbulence reduces considerably. The sodar backscatter cross section is sensitive to the potential temperature stratification and the tri-dimensional coefficient of C_T^2; both change in the vertical (Neff and King, 1987; Neff, 1988). Therefore, when stratification increases the temperature fluctuations in the ABL are sensitive to surface heat fluxes under stagnant situation and local turbulence. The temperature fluctuations under a dynamic situation are sensitive to changes in turbulence formed by the dynamics. The C_T^2 profile displays an exponential decrease representing the free atmosphere. If the C_T^2 profile shows a second maxima this can either represent a stratified layer or a elevated inversion layer. According to the acoustic cross-section equation (see Neff (1988) for more details) a maximum backscatter signal will be found before ABL h when a single inversion is considered, and multiple local maxima will be found when layers are stratified. Different threshold values after the backscatter maximum have been evaluated and tested using second-order closure turbulence simulation combined with sodar experiments (Beyrich and Weill, 1993; Beyrich et al., 1996; Founda et al., 1997) and radiosonde collocated with sodar measurements (Parry et al., 1975; Tyson and von Gogh,

1976; von Gogh and Zib, 1978; Keder, 1999). Still, the determination of stable ABL h by sodar acoustic profiling alone is not straightforward in all cases, especially at high latitude where stratified inversions, elevated inversions, and shear layers Neff (1980 a, b) are present, producing complicated acoustic profile morphologies due to the presence of multiple local maxima below the actual inversion height; local maxima detected above the inversion height indicate the presence of the mentioned elevated inversions. Therefore, based on well-identified synoptic forcing that have been discussed in sections 2 and 3, a more restrictive selection of the periods was conducted to ensure that the ABL flow was well defined and without significant changes over time. Using those identified periods, the maximum gradient of the backscatter pulse was found in order to determine the stable ABL h using the ensemble of sodar profiles; this h was then compared to the radiosonde measurements. The selected cases are: I) 23-25 October 2009, ABL under the influence of a low-level jet; II) 22-24 November 2009, ABL under a synoptic transient; and III) 26-27 January 2010, stagnant anticyclone condition.

2.5.1 Case I: 23-25 October 2009 (low-level jet)

During 23-25 October 2009 the air mass in interior Alaska was dominated by a strong synoptic disturbance with a well-defined cyclonic pattern and strong PGF. A well-established, persistent low-level jet at an average height of 350 m occurred throughout the period, with an average speed of 8 ms^{-1} at the experimental site. Starting at 00 UTC on 23 October the ABL wind direction was north-northeast turning east. Up to the ABL height defined by the thermodynamic profile at 160 m the wind direction changed less than 5 ° and the wind maximum rose to 6 ms^{-1} at 100 m height. Conversely an 8 ms^{-1} low-

level jet was present in the FA at a height of 350 m with main orientation axis from the southeast. The height of the ABL h derived from the maximum gradient of acoustic backscatter was determined to be 230 m, while the thermodynamic profile based on the radiosonde in situ measurements gave h = 160 m. The wind speed profile in the ABL is well defined by the strong PGF.

A subsequent sounding at 12 UTC on 23 October revealed that the low-level jet had increased its speed to an average of 10 ms^{-1}. The wind profile was characterized by an eastern component at 20 m rotating to the south-southeast as high as 200 m with a wind direction variable within 23°. ABL h retrieved by sodar was 310 m and by radiosonde was 305 m, with an average wind speed of 4 ms^{-1}. At 00 UTC on 24 October the configuration of the low-level jet was found at a lower elevation of 250 m with an average wind speed of 6 ms^{-1} and a direction that continued from the southeast, while at 12 UTC on 24 October the low-level jet was observed to decrease in height to 210 m at an average speed of 8 ms^{-1}. Figure 3 illustrates an example from this analysis period: the case of 24 October at 00 UTC, the wind speed and direction profile measured by sodar, the C_T^2 from sodar, the radiosonde temperature and the standard deviation of the wind speed, wind direction, and C_T^2. Time variations of C_T^2 are observed above the temperature inversion at 248 m, driven by the increasing vertical wind speed variability caused by the low-level jet (see Figure 3 lower panels).

During the described period of time h was deduced from sodar profiles, and the methodology described in Menut (1997) agrees well with the sodar measurements. The specific h from radiosonde (sodar) in sequence are: 23 October 00 UTC: h = 160 m (230

m), 23 October 12 UTC: h = 305 m (310 m), 24 October 00 UTC: h = 248 m (290 m), and 24 October 12 UTC: h = 227 m (250 m) (see Figure 3).

2.5.2 Case II: 22-24 November, 2009 (synoptic transient)

Figure 4 presents a graphic representation of these results. On 22 November at 12 UTC the flow at the observational site was quiescent; a weak PGF was verified in interior Alaska with no major synoptic disturbances. This interval of time represents a transitional period from a synoptic-dominated continental Arctic airmass to a maritime polar airmass. For approximately half of the time interval between 21 November at 12 UTC and 22 November at 12 UTC the ABL was under a stagnant flow situation; the average ABL wind speed was < 3 ms^{-1}. At 00 UTC on 22 November 2010 the surface layer became slightly unstable, lifting the ABL; however, the wind direction changed to the north, reestablishing the ABL surface layer stability. The near-neutral state on 22 November 2010 at 00 UTC is indicated by a weak temperature turbulence yielding low C_T^2 values of, on average, <100 a.u. in echo strength with a slight increase in signal at the lifted inversion level. The wind direction profile measured by sodar indicates a high variability in the ABL (i.e. in the interval of 25 ° to 90 °). The methodology following Dimitrios (1990) and Menut (1997) produced the maximum gradient of C_T^2 at a height of 250 m; this result agrees within ~30 m with the observed thermodynamic profile at a height of 282 m.

The atmosphere warmed aloft, affecting the thermodynamic structure of the ABL and therefore its height. The same methodology Dimitrios (1990) and Menut (1997) was applied to process the C_T^2 during this warming period. The C_T^2 profile changed over time.

The situation was initially stagnant; a warm advection developed, then the stagnant situation returned. The ABL stratification after 23 November at 00 UTC eroded due to the advection of warm air from the southerly sector. Above 200 m the thermodynamic ABL height increased as the stratification decreased between 200 m and 300 m. On 22 November at 12 UTC the wind direction was fully established from the northeast direction. The average ABL wind speed was < 3 ms^{-1} (see Figure 4), and the wind direction in the first 100 m was from the east. The σ_{CT}^2 exhibited a local maximum at ~ 75 m where a stratified level can be identified in the temperature profile. A 90 ° change in the wind direction and σ_{WD} increase in the immediate upper levels indicated wind shear. Similarly an increase in the σ_{CT}^2 was observed after ~ 300 m in response to the increasing wind shear above that height. The specific h from radiosonde (sodar) in sequence are: 22 November at 00 UTC: h = 509 m (520 m), 22 November at 12 UTC: h = 306 m (210 m), 23 November at 00 UTC: h = 282 m (190 m), and 23 November at 12 UTC: h = 389 m (210 m). If C_T^2 minimum is used as a criteria to locate the unstable ABL height then the heights are: 22 November at 00 UTC: h = 150 m, 22 November at 12 UTC: h = 510 m, 23 November at 00 UTC: h = 570 m, and 23 November at 12 UTC: h = 510 m (see Figure 4).

2.5.3 Case III: 26-27 January 2010 (Anticyclone Situation)

The atmospheric flow in interior Alaska during this period remained under low wind speed with a weak PGF and there were no major synoptic disturbances. The polar air mass blocked large-scale synoptic motion. The ABL wind speed during the period under study was < 3 ms^{-1} and the wind direction at some heights in the ABL were highly

variable, from 10-70 ° of standard deviation. In the period from 26 January at 12 UTC to 27 January at 00 UTC two stratified layers were verified to occur at 100 m and 200 m in the ABL, with vertical temperature gradient of 3.2 °C / 100 m and 5.45 °C / 100 m, respectively. The two stratified layers evolved into a single layer from 100 m to 200 m high with a temperature gradient of 4.9 °C / 100 m. The C_T^2 sodar profiles from 26 January at 12 UTC, 18 UTC and from 27 January at 00 UTC displayed important variability in this layer. Because the wind speed throughout the entire period was < 3 ms^{-1} advection did not play a major role in ABL thermal changes. In this context, therefore, C_T^2 will reflect little turbulence due to temperature changes caused by IR radiative cooling. In the period from 26 January at 12 UTC to 27 January at 00 UTC a stratified layer formed between 64 m and 105 m with a temperature gradient of 3 °C / 100 m. The development of the stratified layer was followed through time. On 26 January at 12 UTC the C_T^2 verified values of 220 a.u. at 80 m, 195 a.u. at 90 m, and 184 a.u. at 100 m; at the same heights on 27 January 00 UTC the C_T^2 increased to 440, 392, and 333 a.u., yielding a steeper temperature gradient of 10 °C / 100 m. Therefore, the observed layer stabilized with increasing stratification, and C_T^2 provided a good description of changes in that stratification. The wind direction was highly variable (~ 135 ° standard deviation) below 100 m in the ABL, which indicates a stagnant flow situation.

As mentioned earlier, under the conditions during this evaluation period the C_T^2 revealed a complex morphology which responded directly to changes in the ABL thermal gradient as the lower layer cooled via radiation loss. Nevertheless, thermodynamics indicated an ABL height of 367 m which, in turn, corresponded to the minimum thermal

turbulence activity, i.e. the absolute minimum after the displayed local maximal C_T^2, indicating a stratified layered structure. See Figure 5 for details of the C_T^2 shape and the temperature profile under low wind conditions. The specific h from radiosonde (sodar) in sequence are: 26 January at 00 UTC: h = 115 m (120 m), 26 January at 12 UTC: h = 367 m (110 m), 27 January at 00 UTC: h = 399 m (100 m), and 27 January at 12 UTC: h = 425 m (120 m). If using the C_T^2 minimum, is used as a criteria to locate the unstable ABL height, 26 January at 00 UTC: h = 330 m, 26 January at 12 UTC: h = 330 m, 27 January at 00 UTC: h= 350 m, and 27 January at 12 UTC: h = 400 m (see Figure 5).

2.6 Discussion and Conclusions

The characteristics of ABL and FA flows during Wi-BLEx were determined for a range of cases during winter 2009/2010 in interior Alaska. Fifty-six cases were selected with sufficient sodar data representing the transition to winter (October to November 2009) and mid-winter (January to February 2010) to perform this study. Sodar measurements of wind speed and direction were found to converge with the in situ radiosonde data within the average $\pm$ 2σ in $\pm$ 3 hrs at 00 and 12 UTC for all synoptic and FA conditions.

Sodar wind profiling reveals an important variability that allowed flow structures to be detected that were impossible to be measured using the in situ radiosonde system. This variability can be measured under very low wind conditions (e.g., < 3 ms^{-1}) while still above the level of instrumental accuracy ($\pm$ 0.02 ms^{-1} and $\pm$ 3°) and despite adverse meteorological conditions (e.g., fog or low-level stratus clouds) and at very low environmental temperatures (down to -35 ^oC).

The experiment found that for well-identified synoptic periods the sodar measurements of wind speed (wind direction) in anticyclone conditions were 2.6 $\pm$ 0.4 ms^{-1} ($138^o \pm 77^o$) while for cyclone conditions they were 5.0 $\pm$ 0.6 ms^{-1} ($156^o \pm 13^o$). In the case of synoptic transients (i.e., Arctic front, low-level jets) the wind speed and direction were found to be 3.3 $\pm$ 0.4 ms^{-1} ($144^o \pm 56^o$).

In terms of the thermodynamic ABL structure, previous research on the stable nighttime ABL that combined sodar and radiosonde indicated convergent arguments in identifying the maximum of C_T^2 using the position of the strong potential temperature gradient and the decaying shape of the C_T^2 (Neff, 1980 a, b; Anderson, 2003; Balsley et al., 2003). For instance, Kallistratova and Kouznetsov (2009) studied the occurrence of strongly stratified layers down to ~ 3 cm thickness in the lower ABL that provided strong acoustic echoes. Experiments by Anderson (2003) detail a correspondence between the position of temperature gradient changes and the C_T^2 profile maximum. Similarly, Balsley et al. (2003) showed a high-spatial-resolution C_T^2 profile measurement that established a consistent agreement between the location of a strong stable layer and the location of peaks in the C_T^2 signal, and also demonstrated a significant drop in C_T^2 by three orders of magnitude at the top of the stable ABL. Beyrich and Weill (1993) simulated the C_T^2 temperature structure and compared it with sodar measurements to demonstrate that h correlates well with its thermodynamic profile counterpart under well-defined meteorological conditions in the framework of a large-scale hydrometeorology experiment Andre et al. (1986). When examining the stable ABL in the presence of low-level jet structures, Vich et al. (2007) described three nights in which the results of a

monostatic sodar showed that C_T^2 time series represent sporadic mixing; in addition, they demonstrated the presence of strongly-stratified ABL layers in the presence of an overnight low-level jet.

High-latitude ABLs during interior Alaska winters exhibit an extremely complex thermodynamic configuration characterized by strong stratifications, presence of elevated inversion layers that radiatively interact with the surface layer Mayfield and Fochesatto (2011), and wind structures that can easily disrupt and promote changes in the ABL state. One outstanding characteristic of the high-latitude winter ABL is the surface radiation balance, in the absence of a diurnal cycle, which is dominated by long-wave surface radiation cooling; therefore, the surface radiative equilibrium is achieved at a very low energy level. Under these conditions the ABL radiative equilibrium is fragile and prone to changes that could be initiated by a diversity of processes ranging from synoptic-scale, such as warm advective layers above the ABL that could lift the inversion, to small-scale drainage flows that could build stratification.

Comparing the existence of the inversion and flow from the south, this study found results that differ from those in the literature Hartmann and Wendler (2005). Case I in section 4, for example, demonstrated a persistent inversion during a southerly flow in the FA. The apparent difference between this result and that of Hartmann and Wendler (2005) might be explained by the fact that the cases evaluated in Hartmann and Wendler (2005) were under more significant advective flows than in Case I discussed in this article. Warming aloft becomes a dominant feature when significant advective flows are in place Mayfield and Fochesatto (2011)**.** On the other hand, in the case of lifted

inversions (i.e., Case II), the results from this work compare well with those obtained by Beyrich et al. (1996). Future research will address the presence of isothermal layers that can be found more consistently in seasons transitioning into and out of the winter. In these cases a strong surface-based inversion will form from a near-adiabatic temperature profile; intermediate isothermal layers will occur at the interface between the ABL and the FA, promoting mixing from the cold layer above the inversions down into the ABL as cooling in lower ABL levels proceeds. Considering case III from 26 January at 12 UTC to 27 January at 00 UTC, in both radiosonde cases it can be verified that near-neutral layers occurred in the upper portion of the ABL. In this case no significant profile structure of turbulence can be obtained from the sodar measurements because of associated slightly-stable layers, a result that was also found by others (Beyrich and Weill 1993). In fact, the C_T^2 profile from Figure 5 shows a maximum gradient at the point where the strongest stable layer existed. The maximum C_T^2 gradient underestimates the ABL h when compared with the radiosonde profiles of 26 January 2010 at 00 UTC and 27 January 2010 at 12 UTC.

This paper demonstrates that under certain conditions, when the PGF is moderate to strong, the ABL height can be determined using acoustic backscatter measurements and this determination is in agreement with the thermodynamic soundings. However, under a low PGF, stagnant meteorological situations, and transient motions, a good agreement between the two methodologies is difficult to find, particularly because the acoustic sounder responds to the temperature turbulence given by the combined action of

shear stress (inducing mixing) and buoyancy in response to the combined dynamic and radiative flow forcing on local and meso-local scales.

2.7 Acknowledgments

This work was supported by the Fairbanks North Star Borough Air Quality Office, the Department of Environmental Conservation of Alaska (grant G00006433-398755), and the College of Natural Sciences and Mathematics of the University of Alaska Fairbanks. The sodar instrument was acquired through the UPOS grant from the Geophysical Institute, University of Alaska Fairbanks. The authors also acknowledge Dr. Nicole Moelders and Dr. Richard Collins from the Department of Atmospheric Sciences, University of Alaska Fairbanks for fruitful discussions and the support of Remtech Inc, France. The authors also recognize the NWS Fairbanks Office for data support and help in deploying the sodar instruments at the NWS facilities.

2.8 References

Anderson, P.S., 2003: Fine-Scale Structure Observed In A Stable Atmospheric Boundary Layer By Sodar And Kite-Borne Tethersonde. *Boundary-Layer Meteorol.* **107**, 323-351.

Andre, J.C and L. Mahrt, 1982: The Nocturnal Surface Inversion and Influence of Clear-Air Radiative Cooling. *J. Atmos. Sci.*, **39**, 864-878.

Andre, J.C., J.P. Goutorbe, and A. Perrier, 1986: HAPEX-MOBILHY: A Hydologic Atmsopheric Experiment for the Study of Water Budget and Exaporation Flux at the Climatic Scale. *Bull. Amer. Met. Soc.*, **67**, 138-144.

Balsley, B., R. Frehlich, M. Jensen, Y. Meiller, and A. Muschinski, 2003: Extreme Gradients in the Nocturnal Boundary Layer: Structure, Evolution, and Potential Causes. *J. Atmos. Sci.* **60**, 2496-2508.

Baumann, K. and M. Piringer, 2001: Two-Years Of Boundary Layer Measurements With a Sodar - Statistics and Applications. *Phys. Chem. Earth Pt B.* **26**, 205-211.

Benson, C.S., 1969: The Role of Air Pollution in Arctic Planning And Development. *Polar Record.* **14**, 783-790.

Benson, C.S., 1970 a: Ice Fog. *Weather*, **25**, 11-18.

Benson, C.S., 1970 b: Ice Fog: Low Temperature Air Pollution. *CRREL Research Report 121.*

Benson, C.S. and G. Weller, 1970: A Study of low-level winds in the vicinity of Fairbanks, Alaska. Geophysical Institute University of Alaska.pp: 26.

Beran, D., W. Hooke and S. Clifford. 1973: Acoustic Echo-Sounding Techniques and their Application to Gravity-Wave, Turbulence, and Stability Studies. *Boundary-Layer Meteorol*. **4**, 133-153.

Beyrich, F., 1997: Mixing Height Estimation From Sodar Data - A Critical Discussion. *Atmos. Environ.* **31**, 3941-3953.

Beyrich, F and V. Kotroni., 1993: Estimation of Surface Stress over a Forest from Sodar Measurements and Its Use to Parameterize the Stable Boundary-Layer Height. *Boundary-Layer Meteor.* **66**, 93-103.

Beyrich, F. and A. Weill, 1993: Some Aspects of Determining the Stable Boundary-Layer Depth from Sodar Data. *Boundary-Layer Meteor.* **63**, 97-116.

Beyrich, F., U. Weisensee, D. Sprung, and H. Gusten, 1996: Comparative Analysis of Sodar and Ozone Profile Measurements in a Complex Structured Boundary Layer and Implications for Mixing Height Estimation. *Boundary-Layer Meteor.* **81**, 1-9.

Blackadar, A.K., 1957: Boundary Layer Wind Maxima and Their Significance For The Growth of Nocturnal Inversions. *Bull. Amer. Met. Soc.* **38**, 283-290.

Bourne, S.M., U.S. Bhatt, J. Zhang, and R. Thoman, 2010: Surface-based Temperature Inversions In Alaska From A Climate Perspective. *Atmos. Res.* **95**, 353-366.

Bowling, S.A., T. Ohtake, and C.S. Benson, 1968: Winter Pressure Systems and Ice Fog in Fairbanks, Alaska. *J Appl. Meterol. Clim.*, **7**, 961-968.

Brown, E.H. and F.F. Hall Jr., 1978: Advances In Atmospheric Acoustics. *Rev. Geophys.*, **16**, 47-110.

Businger, J.A., and S.P.S. Arya, 1975: Height of the Mixed Layer in the Stably Stratified Planetary Boundary Layer. In *Advances in Geophysics*, Frenkiel, F.N.; Munn, R.E., Eds.; Elsevier: **18**, Part A, pp 73-92.

Cheung, T. K., 1991: Sodar Observations of the Stable Lower Atmospheric Boundary Layer at Barrow, Alaska. *Boundary-Layer Meteor.* **57**, 251-274.

Chintawongvanich, P., R. Olsen and C.A. Biltoft, 1989: Intercomparison of Wind Measurements from Two Acoustic Doppler Sodars, a Laser Doppler Lidar, and In Situ Sensors. *J. Atmos. Ocean. Tech.* **6**, 785-797.

Clarke, R.H., 1970: Observational Studies in the Atmospheric Boundary Layer. *Q. J. Roy. Met. Soc.* **96**, 91-114.

Coulter, R. L. and M.A. Kallistratova, 2004: Two Decades of Progress In Sodar Techniques: A Review of 11 ISARS Proceedings. *Meteorolo and Atmos Phys.* **85**, 3-19.

Crescenti, G.H., 1997: A Look Back On Two Decades of Doppler Sodar Comparison Studies. *Bull. Amer. Met. Soc.* **78**, 651-673.

Dimitrios, M., 1990: Sodar Estimates of Surface Heat Flux and Mixed Layer Depth Compared with Direct Measurements. *Atmos. Env. Part A. General Topics.* **24**, 2847-2853.

Drobinski, P., R.A. Brown, P.H. Flamant, and J. Pelon, 1998: Evidence of Organized Large Eddies By Ground-Based Doppler Lidar, Sonic Anemometer, and Sodar. *Boundary-Layer Meteor.* **88**, 343-361.

Dupont, E., L. Menut, B. Carissimo, J. Pelon, and P. Flamant, 1999: Comparison Between the Atmospheric Boundary Layer in Paris and Its Rural Suburbs During the ECLAP Experiment. *Boundary-Layer Meteor.* **33**, 979-994.

Founda, D., M. Tombrou, D.P. Lalas, and D.N. Asimakopoulos, 1997: Some Measurements of Turbulence Characertistics Over Complex Terrain. *Boundary-Layer Meteor.*, **83**, 221-245.

Gilman G.W., H.B. Coxhead, and F.H. Willis, 1946: Reflection of Sound Signals in the Troposphere. *J. Acoust. Soc. Am.,* **18**, 274.

Grant, A. L. M., 1994: Wind Profiles in the Stable Boundary-Layer, and the Effect of Low Relief. *Q. J. Roy. Meteoro. Soc.* **120**, 27-46.

Hartmann, B. and G. Wendler, 2005: Climatology of the winter surface temperature inversion in Fairbanks, Alaska. *Eight Conference on Polar Meteorology and Oceanography 2005, JP2.26, 1-7.*

Holmgren, B., L. Spears, C. Wilson, and C.S. Benson, 1975: Acoustic Soundings of the Fairbanks Temperature Inversions. *Climate of the Arctic*, Geophysical Institute, University of Alaska, 293-*306.

Kallistratova, M. A. and R. D. Kouznetsov, 2009: A Note On Sodar Return Signals In The Stable Atmospheric Boundary Layer." *Meteorol. Z.* **18**, 297-307.

Keder, J., 1999: Detection of Inversions and Mixing Height by REMTECH PA2 Sodar in Comparison with Collocated Radiosonde Measurements. *Meteorol. Atmos. Phys.,* **71**, 133-138.

Mahrt, L.; R.C. Heald, D.H. Lenschow, B.B. Stankov, and I.B. Troen, 1979: An Observational Study Of The Structure Of The Nocturnal Boundary Layer. *Boundary-Layer Meteor.* **17**, 247-264.

Mayfield, J. and G.J. Fochesatto, 2011: Influence of Synoptic Setup on the Small Scales flow occurrence The Layered Structure of the Winter Atmospheric Boundary Layer in the Interior of Alaska. *J. Appl. Meteorol. Clim. In Review.*

McAllister, L.G., J.R. Pollard, A.R. Mahoney and P.J.R. Shaw, 1969: Acoustic sounding—A new approach to the study of atmospheric structure. *Proceedings of the IEEE*, **57**, 579- 587.

Melgarejo, J.W. and J.W. Deardorff, 1975: Revision to Stability Functions for the Boundary-Layer Resistance Laws Based Upon Observed Boundary-Layer Heights. *J. Atmos Sci.*, **32**, 837-839.

Menut, L., 1997: Etude experimentale et theorique de la couche limite atmospherique en agglomeration Parisienne. Universite Pierre et Marie Curie, Paris. France.

Menut, L., C. Flamant, and J. Pelon, 1999: Evidence of Interaction Between Synoptic and Local Scales in the Surface Layer over the Paris Area. *Boundary-Layer Meteor.* ***93***, 269-286.

NOAA, 1997: Federal Meteorological Handbook No. 3: Rawinsonde and Pibal Observations. FCM-H3-1997. Silver Spring, Maryland. USA.

Neff, W.D. 1980 a: An Observational And Numerical Study Of The Atmospheric Boundary Layer Overlying The East Antarctic Ice Sheet. Ph.D. Thesis University of Colorado, Boulder, Colorado.

Neff, W.D. 1980 b: Observation and Modeling of the Boundary-Layer Overlying the East Antarctic Ice Sheet. *Bull. Amer. Met. Soc.* **61**, 1501-1501.

Neff, W.D., 1988: Observations of Complex Terrain Flows Using Acoustic Sounders: Echo Interpretation. *Boundary-Layer Meteor.* 1988, **40**, 363-392.

Neff, W.D. and C.W. King, 1987: Observations of Complex-Terrain Flows Using Acoustic Sounders - Experiments, Topography, and Winds. *Boundary-Layer Meteor.,* **40**, 363-392.

Parry, H. D., M. J. Sanders Jr., and H.P. Jensen, 1975: Operational Applications of a Pure Acoustic Sounding System. *J. Appl. Met.* **14,** 67-77.

Reichardt, P.B and S.K. Reidy, 1980: Atmospheric Polycyclic Aromatic-Hydrocarbons - an Aspect of Air-Pollution in Fairbanks, Alaska. *Arctic*. **33**, 316-325.

Remtech, 2011: Remtech Sodar Technical Manual. DC02/012 Vélizy, France.

Seibert, P., 1998: Long-time comparison of Remtech PA2 sodar wind and turbulence measurements with Cabauw tower data. Proc. 9th Int. Symp. on Acoustic Remote Sensing and Assoc. Techniques of the Atmos. and Oceans. Österr. Beiträge zu Meteorologie u. Geophysik, **17**, 136-139

Singal S., 1997: Acoustic Remote Sensing Applications. "Influence of the Nocturnal Low-Level-jet on The Vertical and Mesoscale Structure of the Stable Boundary Layer As Revealed from Doppler-Sodar-Observations." Springer**.** In Singal, S., Ed. Springer Berlin / Heidelberg. **69**, pp 236-246.

Tyson, P.D. and R. G. von Gogh, 1976: The use of a monostatic acoustic radar to assess the stability of the lower atmosphere over Johannesburg. *S. Afr. Geogr. J.*, **58**, 57-67.

Vich, M., M.A. Jimenez, and J. Cuxart, 2007: A Study of Three Well-Defined Temporal Intervals In a Stably Stratified Night. *Tethys*. *4*, 35-45.

von Gogh, R.G. and P. Zib. 1978: Comparison of Simultaneous Tethered Balloon and Monostatic Acoustic Sounder Records of The Statically Stable Lower Atmosphere". *J. Appl. Meteor*., **17**, 34-39.

Weller, G. and S.A. Bowling, 1975: Climate of the Arctic, Geophysical Institute, Fairbanks, Alaska.

Wendler, G and K. Jayaweera, 1972: Some measurements of the development of the surface inversion in Central Alaska during winter. *Pure and Applied Geophysics*. **99**, 209-221.

Wexler, H., 1941: Observation of Nocturnal Radiation at Fairbanks, Alaska and Fargo, North Dakota. *Mon. Wea. Rev. Supplement N°. 46, pp: 21.*

Willis, R.A and G.K. Grice, 1977: The Wintertime Arctic Front and Its Effect on Fairbanks, Alaska. *Mon. Wea. Rev.* **105**, 78-85.

2.9 Figures

Figure 1. Comparison of collocated in situ radiosonde and remote sensing Doppler sodar vertical profiling of wind speed (WS, Figures 1a, 1c, 1e) and wind direction (WD, Figure 1b, 1d, 1f) during Wi-BLEx 2009-2010. The black dots represent in situ radiosonde measurements. The continuous dotted line is the average sodar measurement profile. The shaded area encloses the $\pm$ 2σ standard deviation calculated over 37 profiles at 10 min averaging time and 10 m vertical resolution centered on the radiosonde launch for an interval of $\pm$ 3 hrs. Figure 1a and 1b represent 23 October 2009 at 00 UTC, Figure 1c and 1d represent 1 February 2010 at 12 UTC, and Figure 1e and 1f represent 3 February 2010 at 12 UTC.

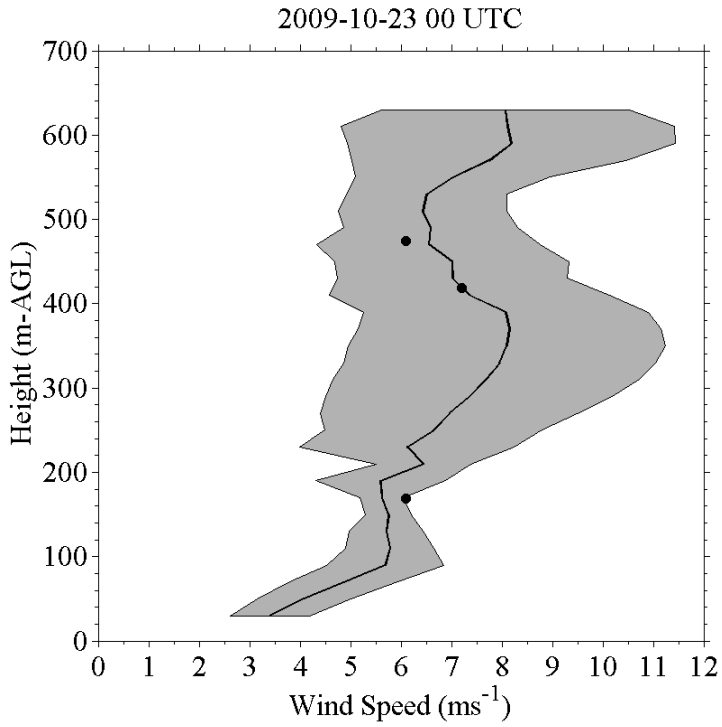

Figure 1a

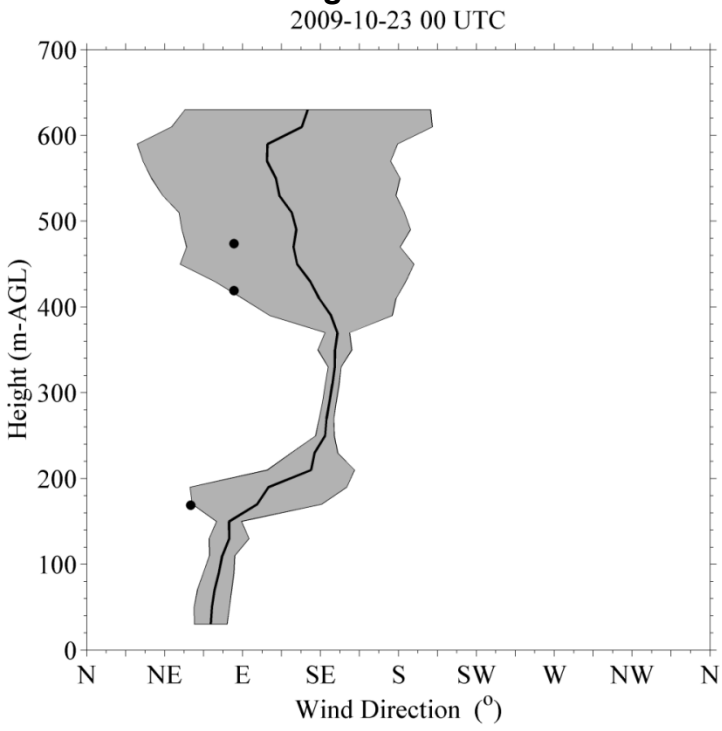

Figure 1b

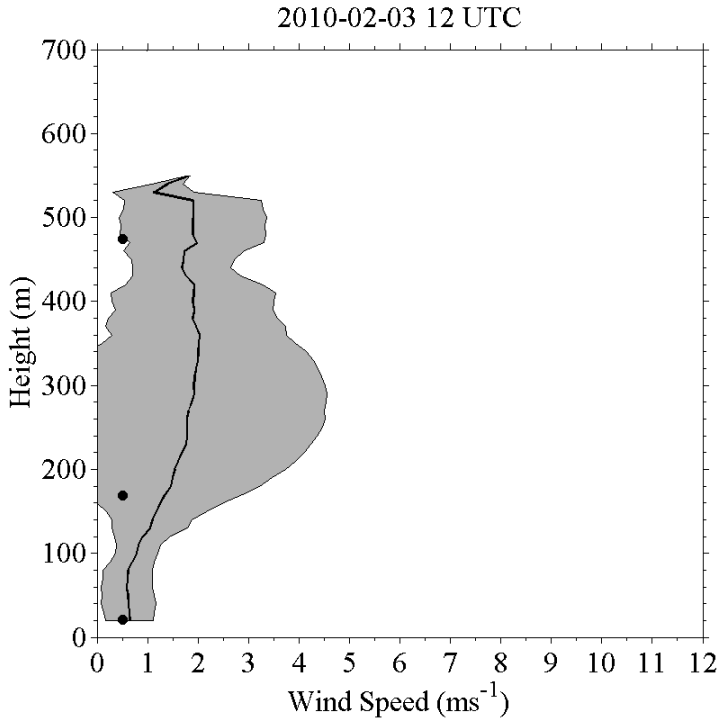

Figure 1c

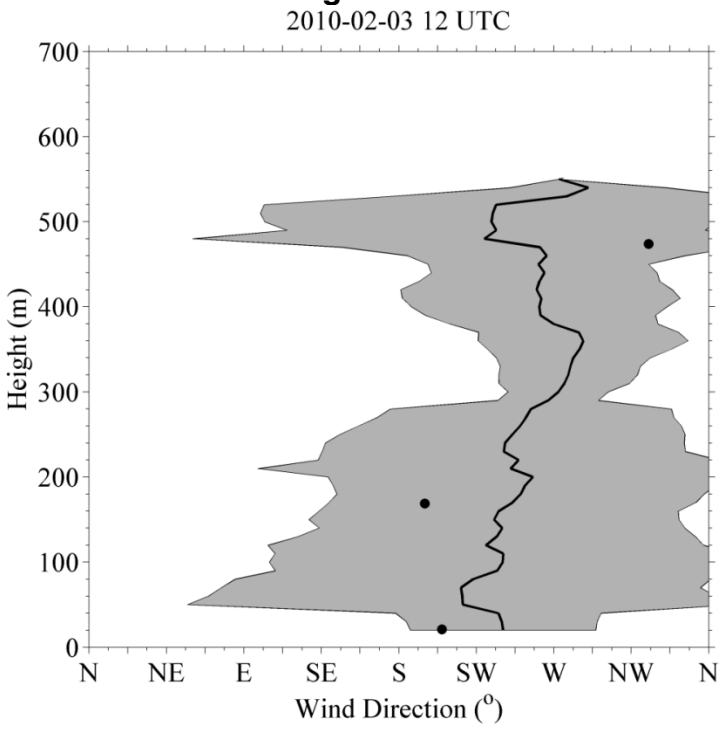

Figure 1d

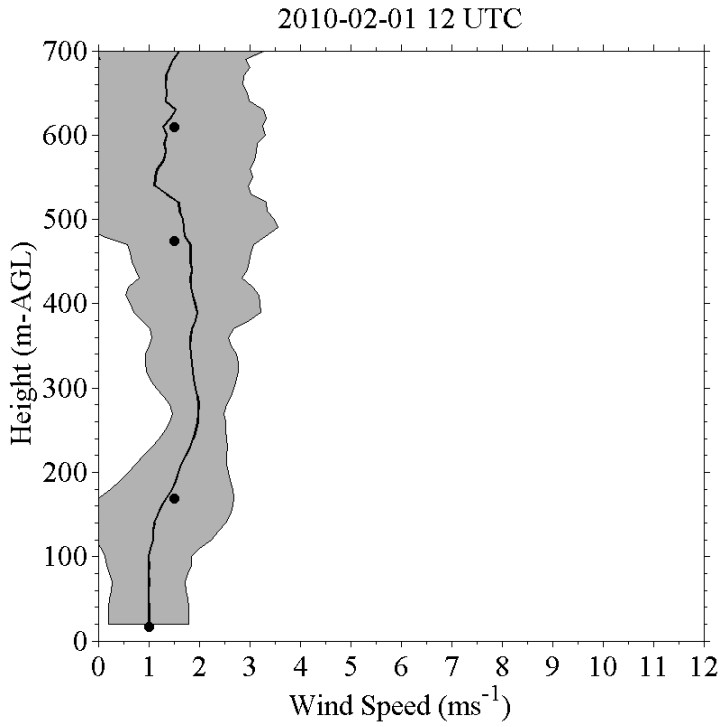

Figure 1e

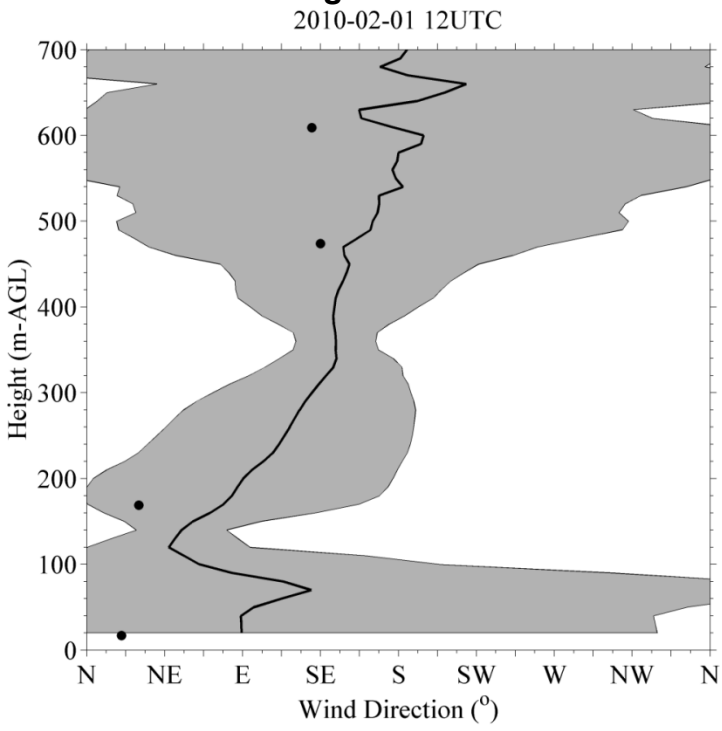

Figure 1f

Figure 2. Summary of the ABL and FA winter flow variability (wind speed and direction). Figure 2a illustrates the ABL wind direction; Figure 2b represents the ABL wind speed variability; Figure 2c corresponds to the FA wind direction variability; Figure 2d displays the FA wind speed variability. Vertical lines represent the amplitude of the standard deviation 1σ for a $\pm$ 3 hrs evaluation and solid black diamond '♦' represent the $\pm$ 3 hours mean.

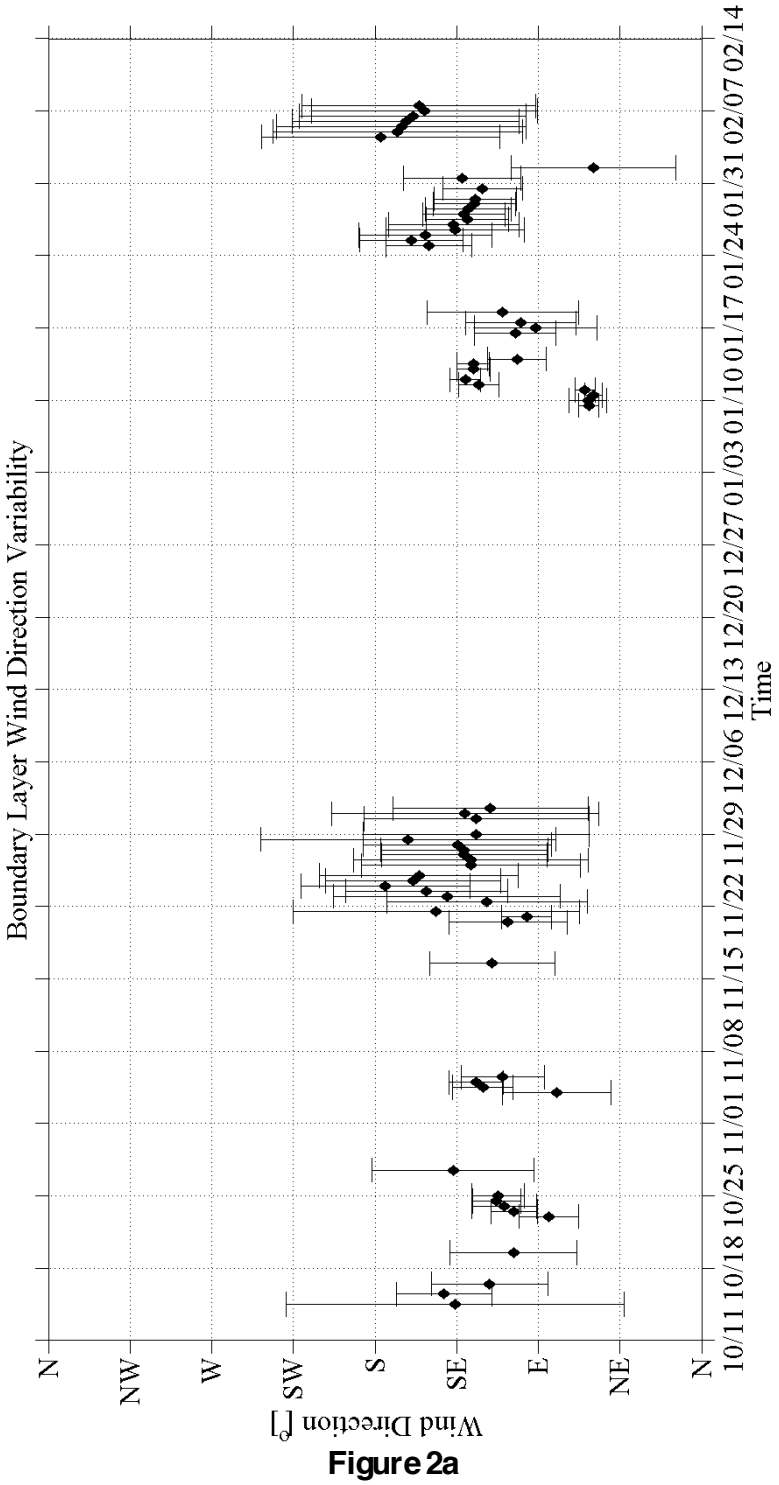
Boundary Layer Wind Direction Variability
Wind Direction [°]
N
NW
W
SW
S
SE
E
NE
N
10/11 10/18 10/25 11/01 11/08 11/15 11/22 11/29 12/06 12/13 12/20 12/27 01/03 01/10 01/17 01/24 01/31 02/07 02/14
Time

Figure 2a

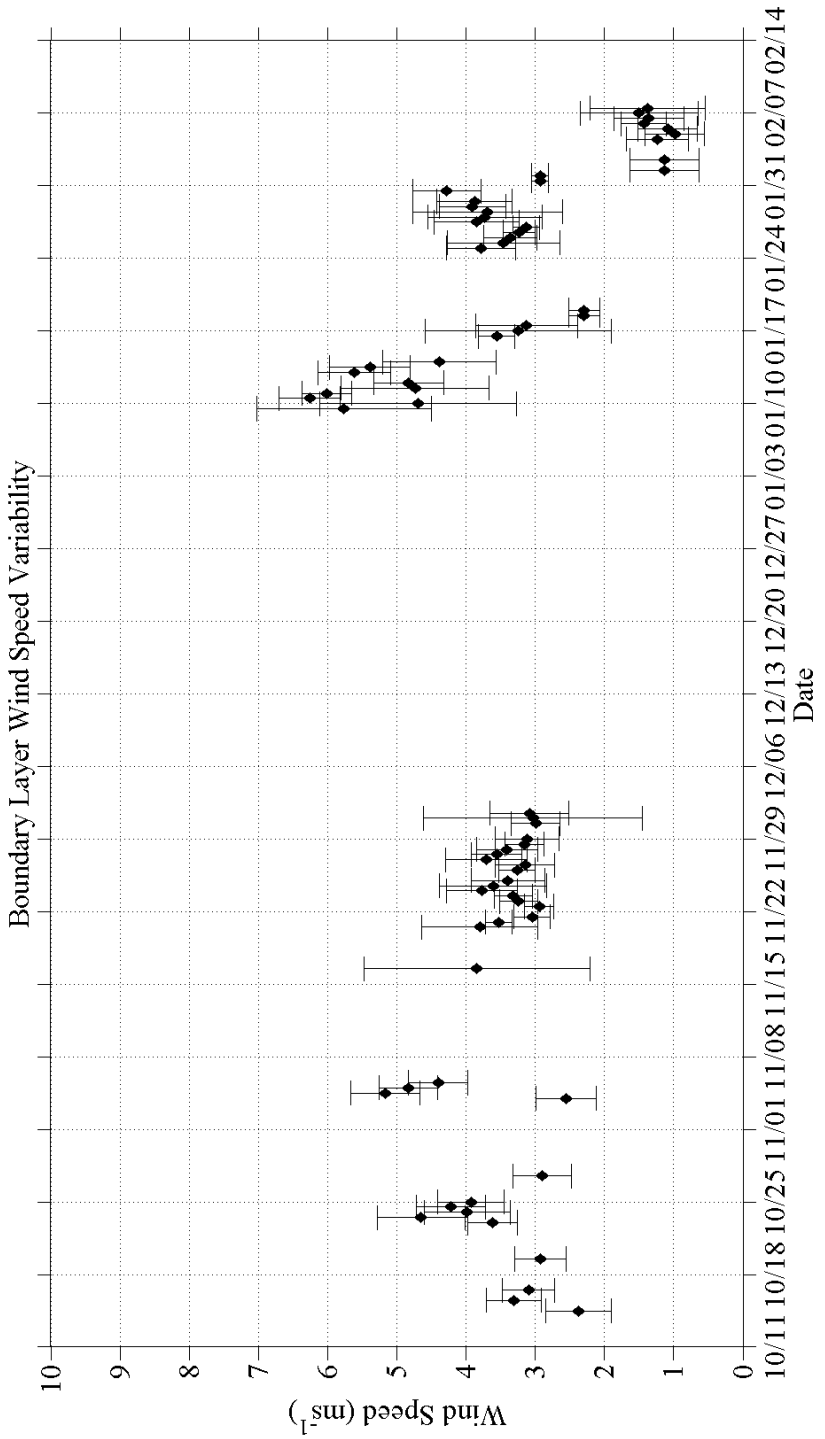
Boundary Layer Wind Speed Variability
Wind Speed (ms-1)
Date
0
1
2
3
4
5
6
7
8
9
10
10/11
10/18
10/25
11/01
11/08
11/15
11/22
11/29
12/06
12/13
12/20
12/27
01/03
01/10
01/17
01/24
01/31
02/07
02/14

Figure 2a

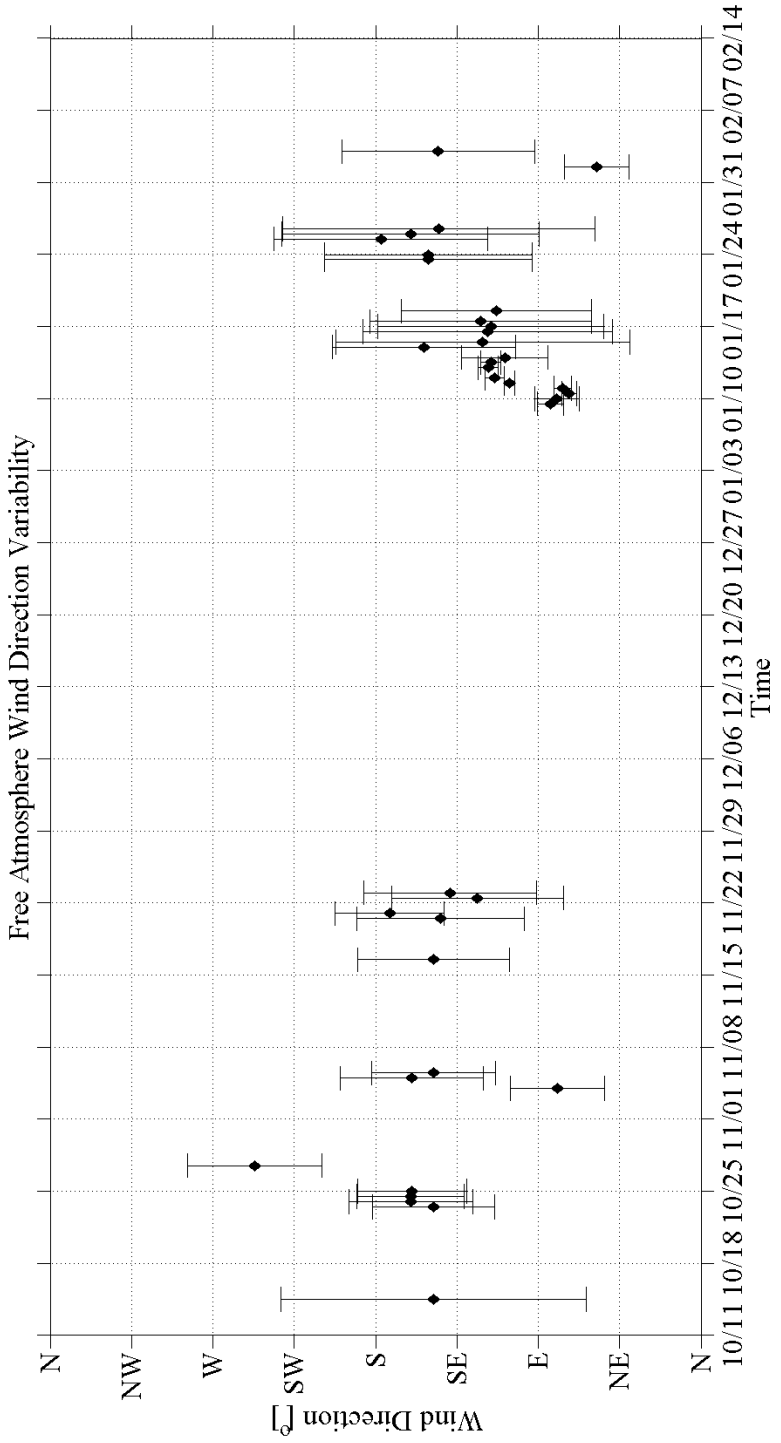
Free Atmosphere Wind Direction Variability
Wind Direction [°]
N
NW
W
SW
S
SE
E
NE
N
Time
10/11 10/18 10/25 11/01 11/08 11/15 11/22 11/29 12/06 12/13 12/20 12/27 01/03 01/10 01/17 01/24 01/31 02/07 02/14

Figure 2c

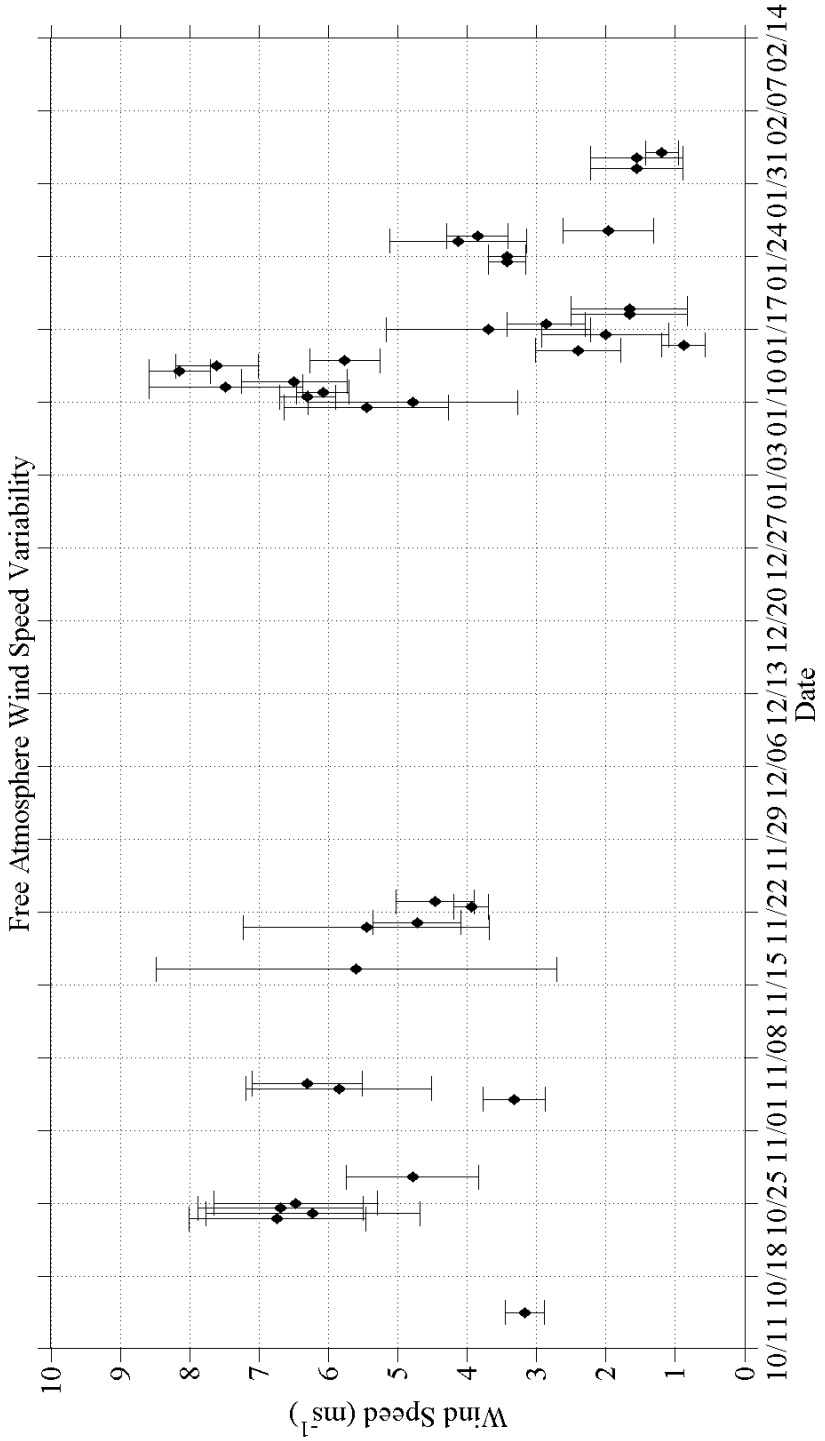
Free Atmosphere Wind Speed Variability
Wind Speed (ms-1)
Date
0
1
2
3
4
5
6
7
8
9
10
10/11
10/18
10/25
11/01
11/08
11/15
11/22
11/29
12/06
12/13
12/20
12/27
01/03
01/10
01/17
01/24
01/31
02/07
02/14

Figure 2d

Figure 3. Case I: 23-25 October 2009. The figures illustrate 24 October 2009 at 00 UTC. Figure 3a represents the sodar wind speed (light trace) and wind direction (dark trace), Figure 3b represents the standard deviation of wind speed (σ_{WS}, light trace), Figure 3c the acoustic backscatter (C_T^2), Figure 3d is the radiosonde temperature profile, and Figure 3e represents sigma C_T^2 (σ_{CT}^2) calculated over $\pm$3 hrs interval. The height is indicated on the vertical axes in m above ground level.

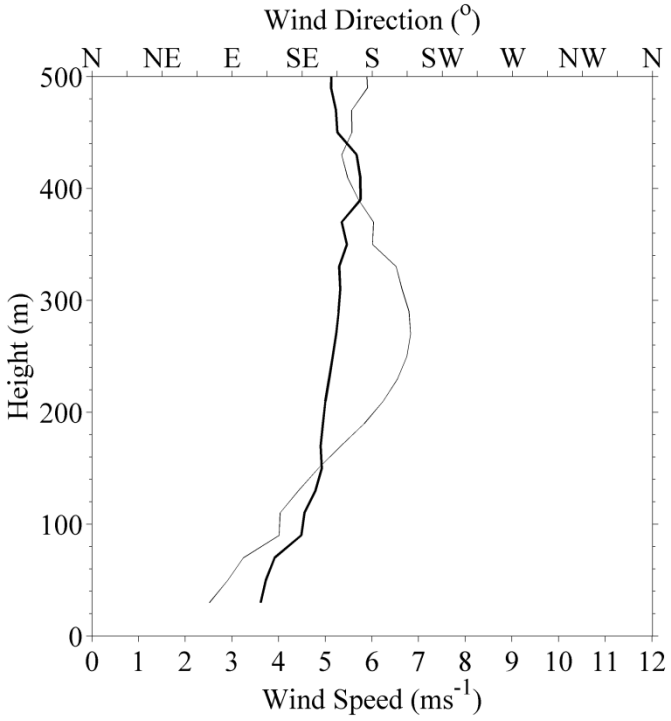

Figure 3a

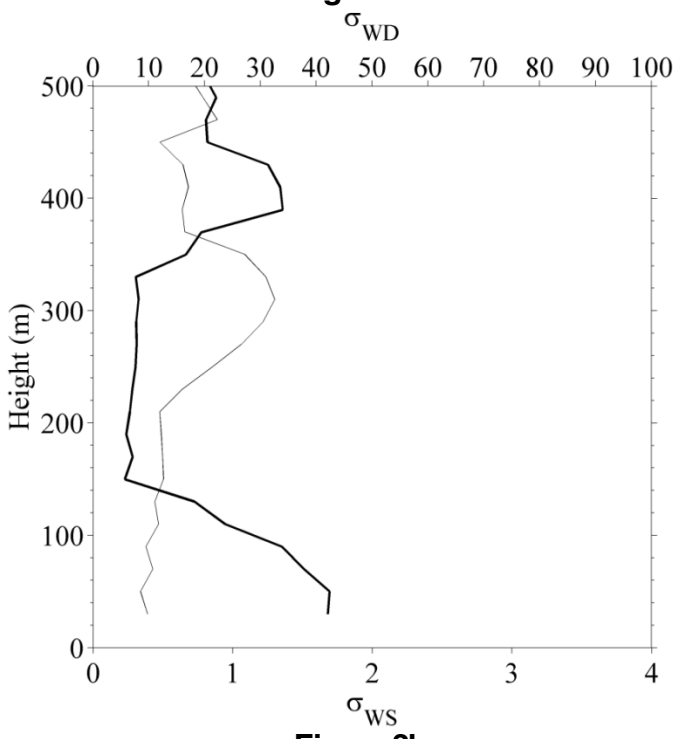

Figure 3b

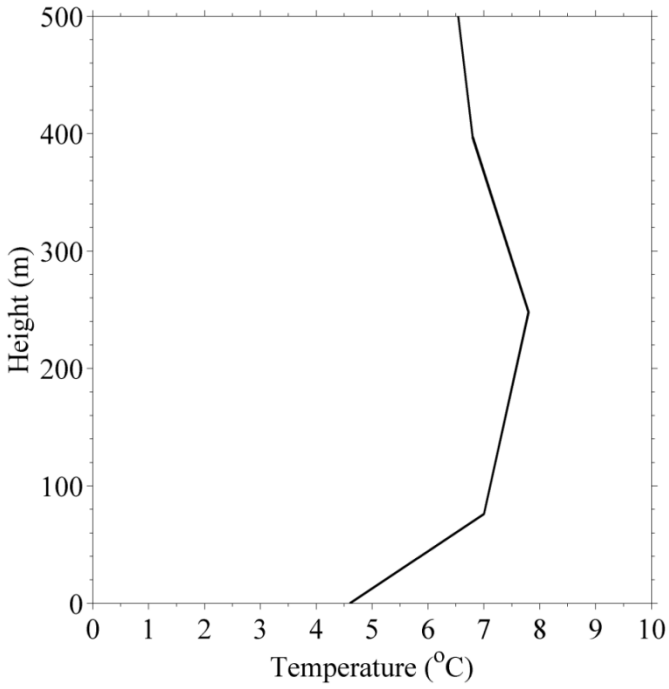

Figure 3c

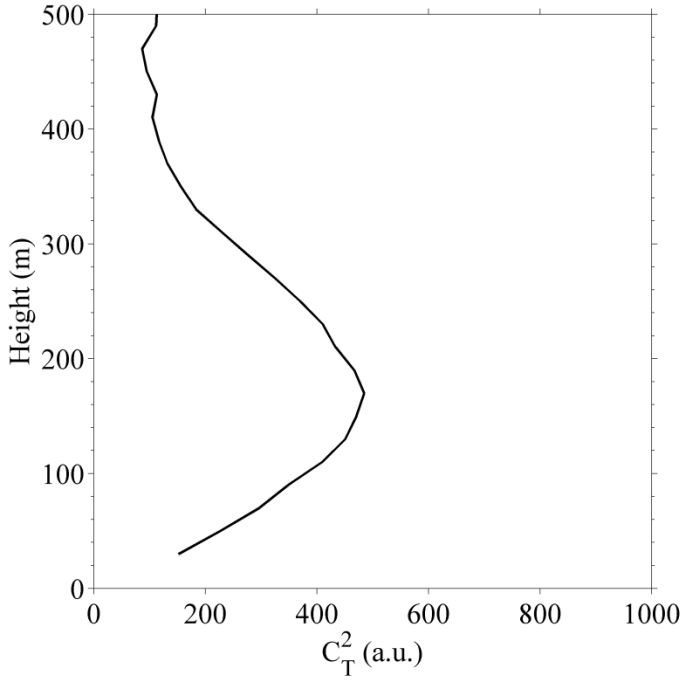

Figure 3d

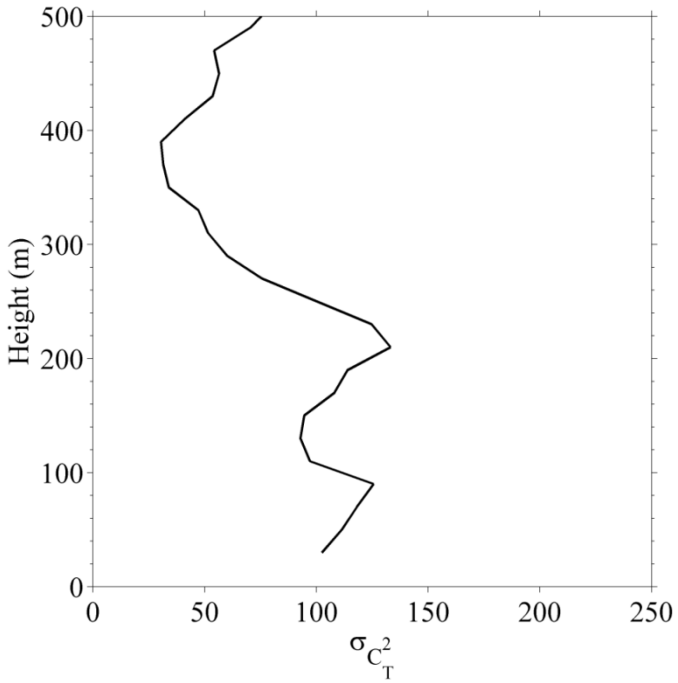

Figure 3e

Figure 4. Case II: 22-24 November 2009. The figures illustrate the case of 23 November 00 UTC. Figure 4a represents the sodar wind speed (light trace) and wind direction (dark trace), Figure 4b represents the standard deviation of wind speed (σ_{WS}, light trace), Figure 4c the acoustic backscatter (C_T^2), Figure 4d is the radiosonde temperature profile, and Figure 4e represents sigma C_T^2 (σ_{CT}^2) calculated over $\pm$3 hrs interval. The height is indicated on the vertical axes in m above ground level.

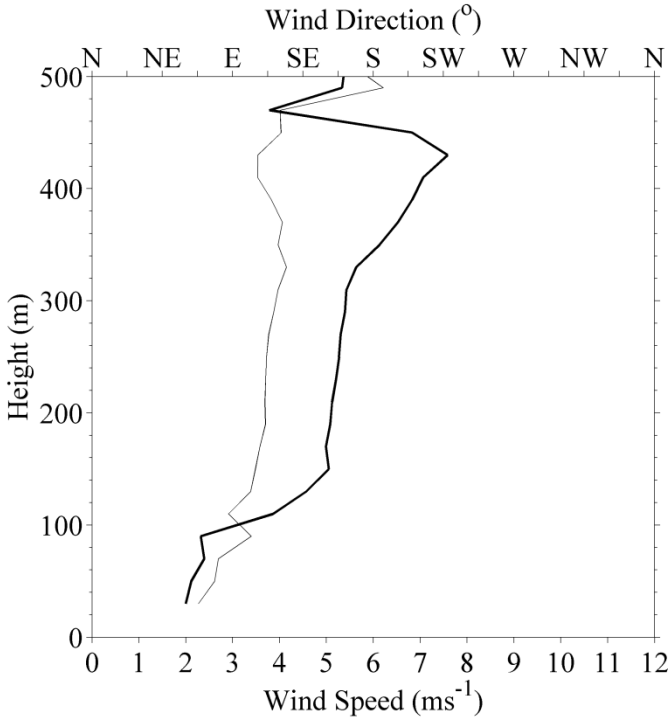

Figure 4a

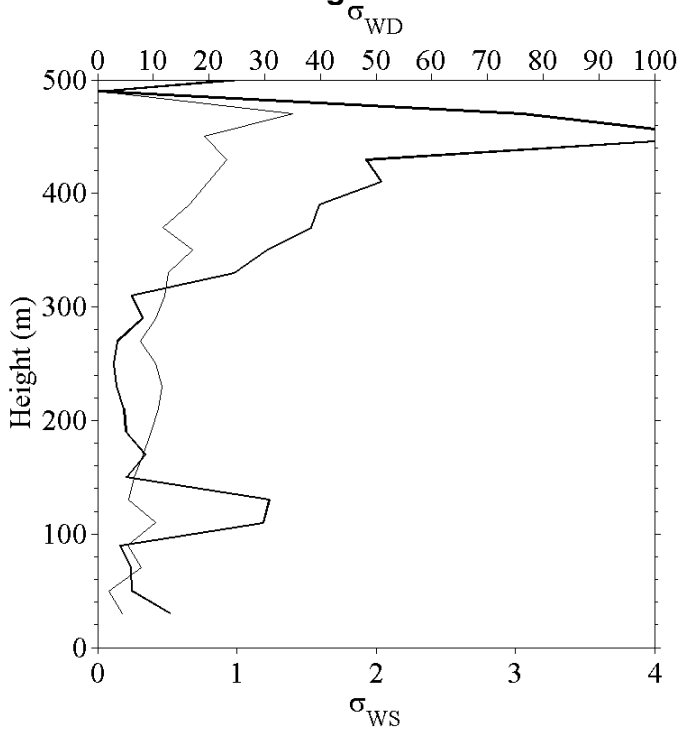

Figure 4b

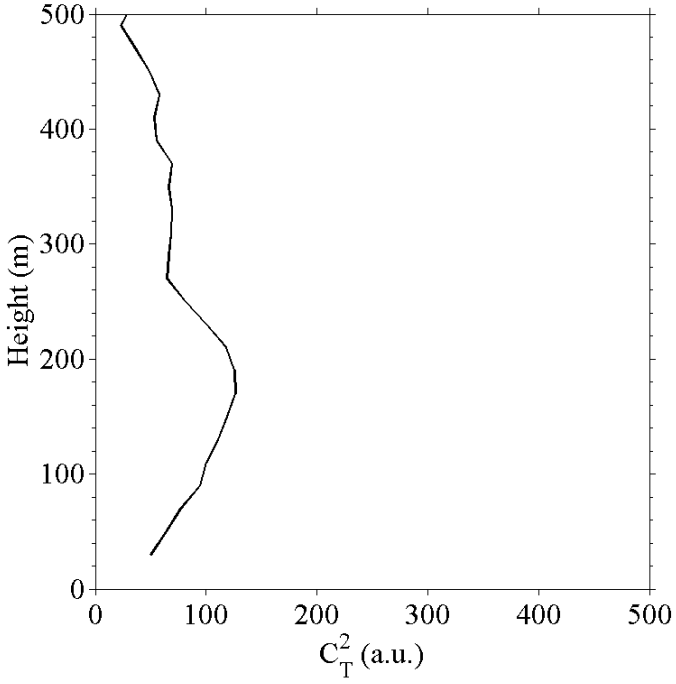

Figure 4c

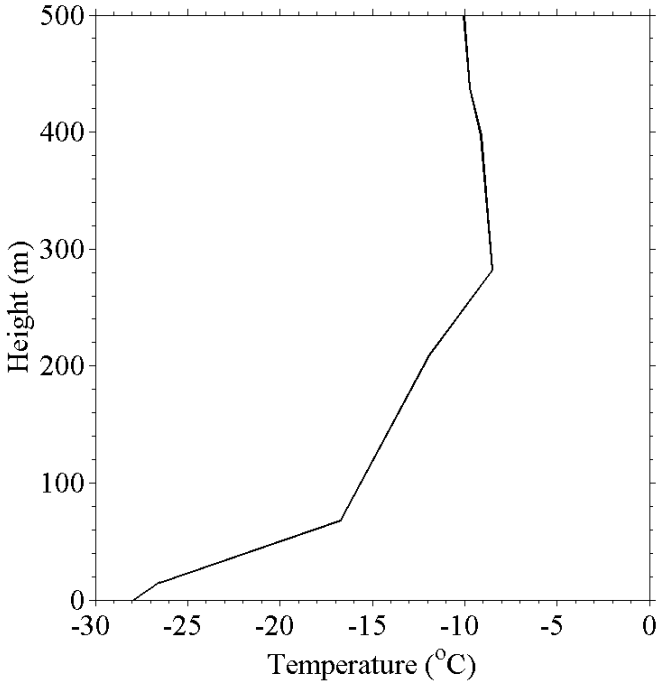

Figure 4d

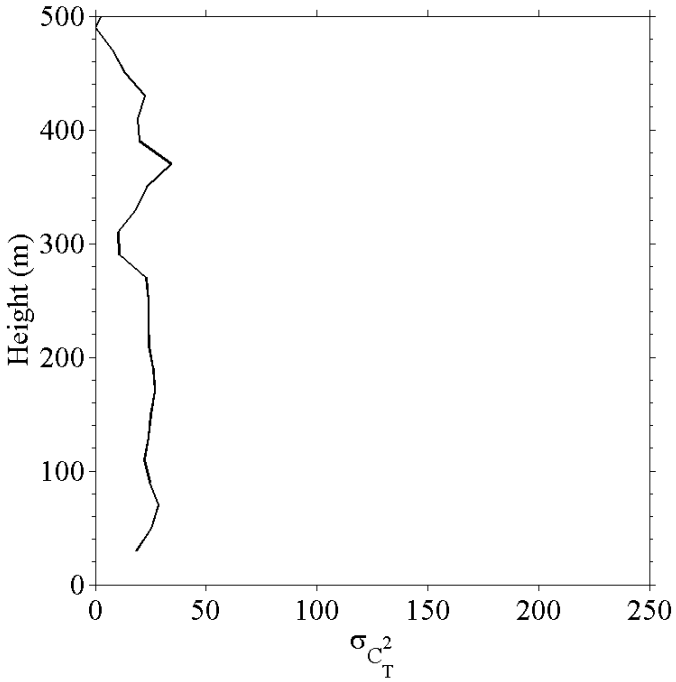

Figure 4e

Figure 5. Case III: 26-27 January 2010. The figures illustrate the case of 26 January 12 UTC. Figure 5a represents the sodar wind speed (light trace) and wind direction (dark trace), Figure 5b represents the standard deviation of wind speed (σ_{WS}, light trace), Figure 5c the acoustic backscatter (C_T^2), Figure 5d is the radiosonde temperature profile, and Figure 5e represents sigma C_T^2 (σ_{CT}^2) calculated over $\pm$3 hrs interval. The height is indicated on the vertical axes in m above ground level.

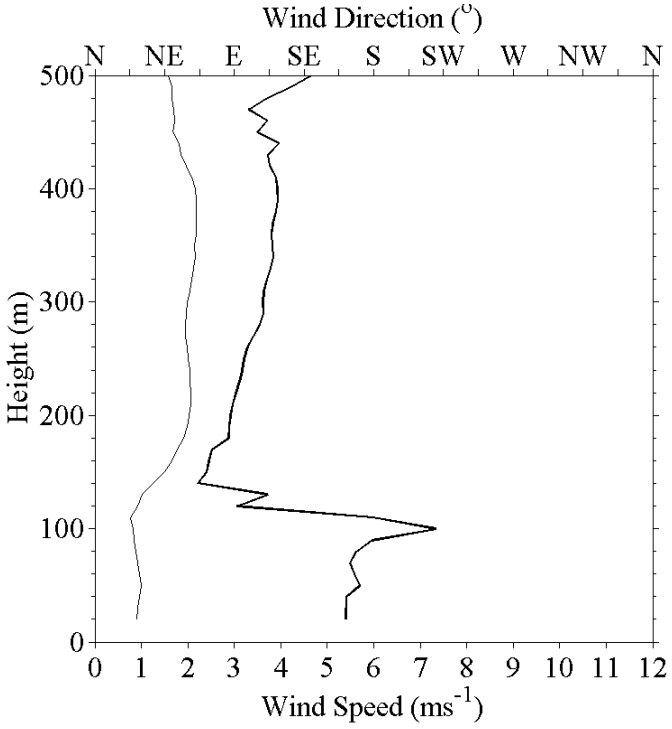

Figure 5a

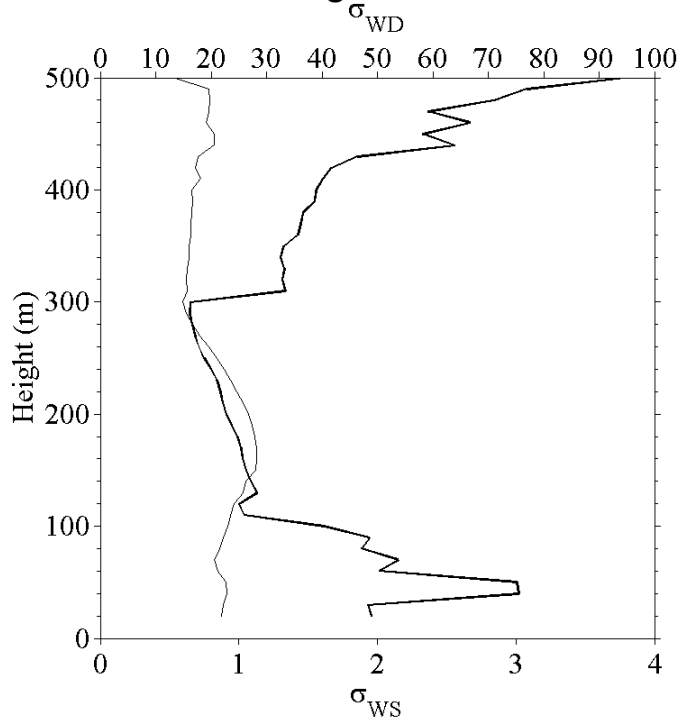

Figure 5b

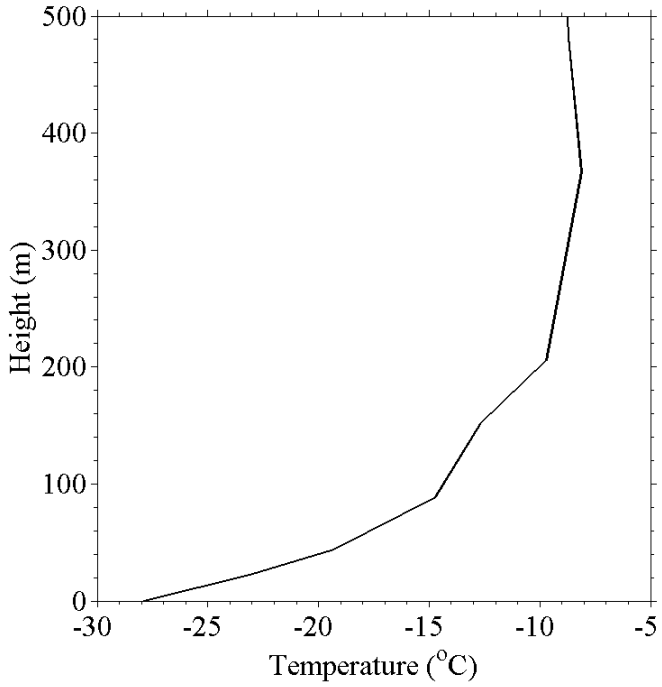

Figure 5c

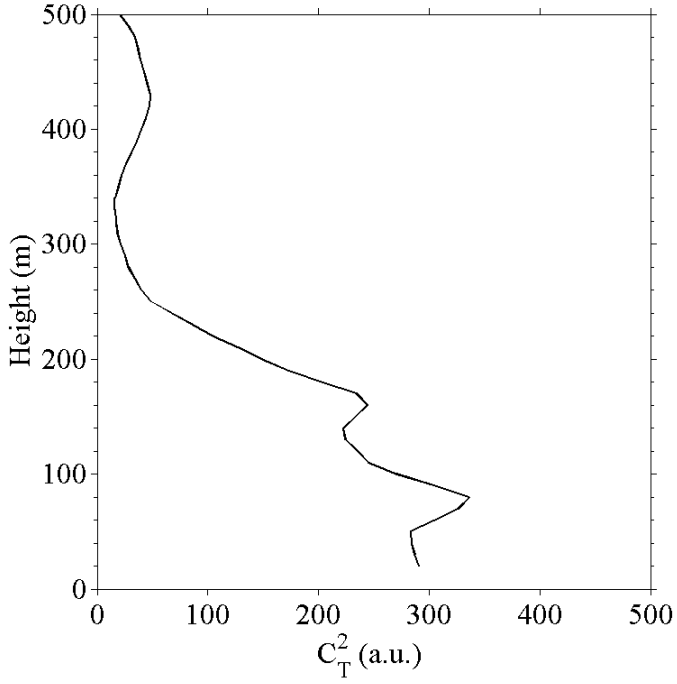

Figure 5d

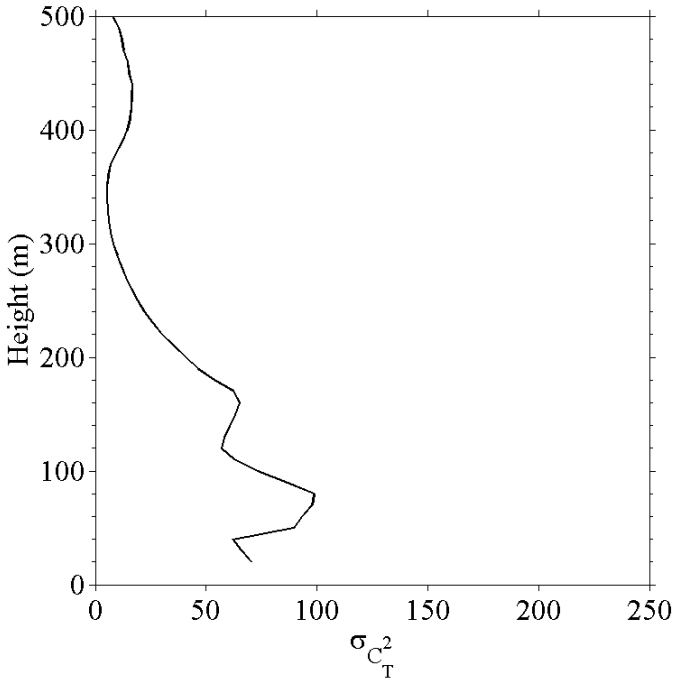

Figure 5e

2.10 Tables

Table 1. Absolute error between in situ radiosonde and remote-sensing sodar measurements. Column values are: z (radiosonde measurement height), <ws> and σ_{ws} (mean and standard deviation of sodar wind speed over $\pm$3 hrs interval at the closest z height within 10 m resolution), ws and wd (in situ radiosonde wind speed and direction measurements), Δws and Δwd (absolute errors of wind speed and direction from sodar measurements compared to the radiosonde system), <wd> and σ_{wd} (mean and standard deviation of wind direction retrieved by sodar profiling). Accuracy of radiosonde system: $\pm$1.5 ms^{-1} and $\pm$5 deg (NOAA, 1997) and accuracy of sodar system: $\pm$0.2 ms^{-1} and $\pm$3 deg (Remtech, 2011)

#	z (m)	<ws>	σws	ws	Δws	<wd>	σ_{wd}	wd	Δwd
23 October 2009, 00 UTC									
1	169	5.6	2.6	6.1	-0.5	98	30.0	70	38
2	419	7.3	2.3	7.2	0.1	134	40.2	85	49
3	471	6.5	2.1	6.1	0.4	119	56.2	85	34
1 February 2010, 12 UTC									
1	17	1	0.1	1	0	89	75.8	20	69
2	169	1.4	0.06	1.5	-0.1	79	0.4	30	49
3	474	1.7	0.2	1.5	0.2	156	25.8	135	21
4	609	1.3	0.33	1.5	-0.2	176	10.55	130	46
5	779	2.4	0.27	1.5	0.9	151	14.1	235	-84
3 February 2010, 12 UTC									
1	169	0.6	0.04	0.5	0.1	241	147.7	205	36
2	419	0.6	0.8	0.5	0.1	246	176.4	195	51
3	471	1.9	0.2	0.5	1.4	230	156.6	325	-95

Table 2. Relative frequency (%) of occurrence of ABL and FA wind speed intervals

WS (ms^{1})	≤ 1.0	1.0-2.0	2.0-3.0	3.0-4.0	4.0-5.0	5.0-10	10-15
BL	10.8%	7.8%	17.9%	22.0%	12.8%	28.2%	0.5%
FA	3.9%	10.2%	8.0%	15.9%	17.5%	42.3%	2.2%

Chapter 3: Influence of Drainage Flow in the Wintertime Atmospheric Boundary Layer at High Latitude[1]

3.1 Abstract

We present observational evidence of mixing followed by stratification in the Stable Atmospheric Boundary Layer (SABL) due to the penetration of drainage flows during the Winter Boundary Layer Experiment (Wi-BLEx). The experiment took place in the Tanana Valley, location of the Chena and Tanana river basins surrounding Fairbanks, Alaska. The area is sheltered by nearby hills that rise to 300-500 m on the north with a southern barrier, the foothills of the Alaska Range, ~60 km distant. During winter the adjacent valleys develop strong SABLs; the absence of solar radiation combined with clear skies, snow-covered surfaces, and low pressure gradient forces enable the formation of small-scale drainage flows connecting the north- with the south-facing slopes. Wi-BLEx observations in the winter 2010-2011 documented the penetration of the drainage flow into the SABL from the northwest sector based on sonic anemometer, laser scintillometer, and acoustic vertical sounding. This irrupting small scale cold flow drives a noticeable increase in the thermal turbulence in the structure of the SABL, mixing in the surface layer, and re-stratification at the surface once the flow extinguishes. Moreover, the drainage flow promotes horizontal mixing of cold air from north-facing slopes with the stagnant polluted air mass on the urban side of the valley.

---

[1] Mayfield J. and G. J. Fochesatto. 2011. Influence of Drainage Flow in the Wintertime Atmospheric Boundary Layer at High Latitude. In Preparation for submission to the *Journal of Applied Meteorology and Climatology*

3.2 Introduction

The absence of daylight combined with snow-covered surfaces during the extreme continental Alaska winter sets up a unique meteorological condition in the lower troposphere where radiative cooling is one of the dominant forcing mechanisms causing an extremely stable Atmospheric Boundary Layer (ABL) to form, particularly under anticyclone conditions and clear skies in mid-winter. In these cases and under weak synoptic flow forcing, the topographic configuration and the orientation of mountains in the Fairbanks area constrain the low-level tropospheric circulation. The air flow in the ABL becomes locally quasi-laminar and regionally stagnant and is dominated mainly by local-scale circulation mechanisms and strong radiative cooling. This meteorological configuration sets up several days of strong stable ABLs (SABLs), and a multiply–stratified, strong surface-based inversion layer develops (Bowling et al. 1968; Beran et al. 1973; Holmgren et al. 1975; Brown and Hall 1978). Arctic mountains and hills shelter large cold pools of air between them that are exposed to a higher radiative cooling rate; these conditions allow density flows to develop in the form of drainage flows. Such small-scale flows channeled through the varying terrain morphology connect basins on the north-facing to those on the south-facing sides of the mountains and hills, and profoundly affect the stability of the lower and warmer basins as well as the micrometeorological flux regimes. These flows can be identified as cold down-slope winds initiated by the temperature contrast between basins and the SABL strong stratification that is built locally at the basin scale (Clements et al. 2003).

Extreme winter conditions in Fairbanks have been known for several decades to represent a very complex air pollution problem (Benson, 1965; Bowling et al., 1968; Wendler and Jayaweera, 1972) due to the development of a strong surface cooling rate and, consequently, the formation of low-level surface-based inversions, often with multiple stratified layers, under specific synoptic conditions (e.g., calm winds and stagnant quiescent synoptic flows) (Bowling et al., 1968; Holmgren et al., 1975) over a period of several days (Mayfield and Fochesatto, 2011). These conditions and the complexity of the ABL structure impose stringent modeling restrictions on ABL representation in air pollution models (Moelders and Kramm, 2010). The first observation of the winter ABL in Fairbanks using a bi-static sodar instrument from the National Oceanic and Atmospheric Administration (NOAA) Wave Propagation Laboratory discovered important dynamic aspects of the SABL, such as propagation of waves, inertial oscillations, strong multilayered structures, "braided" structures within the ABL depth, and formation and destruction of inversion and stratified layers (Holmgren et al., 1975; Brown and Hall, 1978). Despite the importance of these observations no further efforts have been dedicated to continuing these investigations of particular and important environmental conditions at high latitude. An explanation of the strongly-stratified and stagnant low-level flow dynamic in the Fairbanks valley was conceptualized as follows: during the extreme winter a heavier air mass lies close to the ground where a surface-based inversion forms as the result of a strong radiative cooling rate, pronounced in the absence of sunlight, and extremely low wind speed, often less than ~1 ms^{-1}. In these conditions, katabatic flows normally found in mid-latitude settings are suppressed by the

extreme cold pool of the Tanana Valley air mass and the lack of shortwave radiation to override the slope stratification (Benson 1970 a, b; Benson and Weller 1970).

In this study, we provide observational evidence that during the winter period the valley ABL is penetrated by a small-scale cold flow from the north-northwest of the observational site (see Figure 1). This flow has been observed to interact with the local SABL under specific prescribed stagnant anticyclone conditions, and to dominate the thermodynamic structure and circulation of the SABL for specific periods of time close to the hill slopes around Fairbanks.

It is generally accepted that inversions, especially in the Fairbanks area, are forced by a strong radiative cooling in the absence of solar radiation and therefore no diurnal cycle is present (Benson, 1965). However, this paper presents observational evidence of a different mechanism, including mixing and re-stratification at the surface layer and increasing thermal turbulence at the top of the SABL close to mountain and hill slopes at high latitudes induced by penetrative drainage flows. This flow originates upstream in sheltered cold pools of air, where the combination of geographic orientation and very low solar elevation angle during the winter allows for a more efficient radiative cooling than in the central valley region, i.e., the south facing slopes of the Tanana Valley (see Figure 1).

In this paper, we analyze three drainage flow cases by combining local scale surface layer turbulence observations made with sonic anemometers with turbulence at basin scale observed with a laser scintillometer (520 m beam path across the basin) and upper-level ABL structure and turbulence measured using an acoustic phased-array

Doppler sodar. Section 2 presents the experimental setup, section 3 describes the meteorological situation during the observations, and section 4 introduces the observations of drainage flows and ABL structure. Section 5 discusses the cases and determined the influences of the drainage flow in the SABL and outlines conclusions in the context of the high latitude ABL in interior Alaska.

3.3 Experiment and Methodology

The Winter Boundary Layer Experiment (Wi-BLEx) is devoted to investigating the structure and turbulence of the SABL in the interior of Alaska. The observational program took place at the University of Alaska Fairbanks (UAF) Experimental Farm located in the south-facing basin in the foothills of the Cranberry Hills on the UAF campus. The specific sets of observations discussed in this paper were carried out from 1 November, 2010 to 30 March, 2011.

The instrumentation consisted of two 3D-sonic anemometers installed at 2 m and 4 m height on a meteorological mast in the center of the farm (see Figure 2). The sonic anemometers acquired, at 10 Hz, three components of the velocity field as well as the sonic virtual temperature (this includes temperature and relative humidity) to calculate the turbulent quantities u', v', w', and T'. These surface-layer observations were combined with data from an ABL profiler. The acoustic phased-array Doppler sodar (Remtech PA-0) was installed 130 m north of the sonic anemometer tower. The sodar profiled the ABL from 20 m to 500 m to determine the coefficient of turbulent structure parameter C_T^2 (known also as the un-calibrated acoustic backscatter), wind speed, wind direction, and vertical velocity at 10-min time intervals and 10 m vertical resolution. A Boundary Layer

Scintillometer (Scintec BLS 900) was set across the basin to acquire the refractive index turbulence structure parameter (C_n^2). The layout of the instruments is superimposed upon an aerial photo of the University Farm (see Figure 2). The sonic anemometers were calibrated before being placed in the field. Previous to field deployment the anemometers were installed in a closed chamber, and calibrated for the zero speed velocity measurement on the three components of the wind speed and temperature against the Väisälä T-RH probe HMT-330. Similarly the sampling rates of the sonic anemometer and the high-speed data logger were controlled for sampling rate synchronization and time stamp acquisition. The methodology used to signal-process and extract the turbulence data from the sonic anemometers followed the high pass filtering technique giving by the streamline coordinate rotation method (Kaimal and Finnigan, 1994; Wilczak et al., 2001). In this case, the time interval to apply this methodology and preserve the drainage flow events was determined to be over a window of 5 min. This time-window allowed achieving the best compromise between sampling error of turbulent magnitudes and the representation of the wind measurement in terms of minimizing the probability of change in the wind direction (Vickers and Mahrt, 1997). The temperature data was processed using the same time-window interval (5 min.) and using a low pass autoregressive moving average digital filter to extract the low frequency component (Lee et al., 2004).

Based on the retrieved turbulent magnitudes the combining auto-covariance of wind speed components and their cross-covariance the turbulent kinetic energy (TKE) Eq(1), the surface friction velocity (u*) Eq(2), the surface shear stress (τ_0) Eq(3) and the flux Richardson number (Ri_f) Eq(4) were calculated.

$$\mathrm{TKE} = \frac{1}{2}\left(\overline{(u')^2} + \overline{(v')^2} + \overline{(w')^2}\right) \quad (1)$$

$$u^* = \left(\overline{u'w'}^2 + \overline{v'w'}^2\right)^{1/4} \quad (2)$$

$$\tau_0 = u'v' \quad (3)$$

$$\mathrm{Ri_f} = \frac{-\frac{g}{T}\overline{w'T'}}{\overline{u'w'}\frac{du}{dz} + \overline{v'w'}\frac{du}{dz}} \quad (4)$$

The BLS was operated at 125 Hz in the laser emission and one-minute averaging in the receiver at approximately 520 m distance across the basin. The acquired data were processed to recalculate C_n^2 according to Eq. (5) at 1 min resolution over a flat, snow-covered surface.

$$C_n^2 = 1.22 \cdot D^{\frac{7}{3}} \cdot L^{-3} \cdot {\sigma_{In(I)}}^2 \quad (5)$$

where D is the diameter of the receiver's optical lens, L is the length (m) of the laser's path, and ${\sigma_{In(I)}}^2$ is the calculated variance of the intensity (I), the laser's intensity over the time period (Kleissl et al., 2008). Temperature and pressure data acquired at approximately the center of the BLS beam were used to estimate the heat fluxes using the Monin-Obukhov similarity corrected by the stability functions depending of the Obukhov stability parameter (z/L) (De Bruin et al. 2002).

3.4 Meteorological and Mean Flow Conditions during Observations

Three cases were selected from the experiments carried out during Wi-BLEx, two cases from middle of the winter, cases I and II, and a third case representing the late

winter conditions: Case I: 18-19 January 2001; Case II: 7 February 2011 and Case III: 6 March 2011.

Case I: A surface high-pressure system was centered over the central Yukon and built surface pressure strength to 1040 hPa. A surface high (1043 hPa) over Siberia maintained the anticyclone motion of air masses in interior Alaska. The ABL was in a stagnant flow condition in Fairbanks under a weak pressure gradient force (PGF), resulting in weak winds and clear skies which drove radiational cooling of the basins in the observational area. Figure 3 (a) illustrate the wind direction panel and the wind speed in Figure 3 (b) over the site. These plots are a combination of surface and upper ABL levels measured by sonic anemometer 4 m above the surface and Doppler sodar in upper levels in the ABL and the free atmosphere (FA) measured by sonic anemometer 4m height and Doppler Phased array Sodar at 55 m and 165 m.

Case II: The observations during Case II were made under the influence of a surface high-pressure system that covered the Yukon and central Alaska regions (~1037 hPa). The PGF was weak over interior Alaska, resulting in weak ABL winds at the observational site. Low-level cloud coverage was suppressed by the presence of the high-pressure system. The surface layer flow verified the occurrence of nighttime drainage events in sequences of 270 min, followed by a drainage event of 120 min and five subsequent short-period intermittent flows in decreasing wind speed each one lasting less than 60 minutes. Figure 4 (a) illustrate the wind direction and Figure 4 (b) the wind speed over the site. These plots are a combination of surface 4 m height sonic anemometer 10

min averaged wind direction and wind speed and Doppler sodar in upper levels in the ABL and the free atmosphere (FA).

Case III: Observations during late winter verified the presence of a surface ridge to the south, ~40 km from the observational site with tight isobars over southeast Alaska. Surface high pressure (1036 hPa) centered over the Alaska/Yukon border established a PGF that weakened as the surface high pressure moved over the Brooks Range. The ABL state in the Tanana Valley was forced by the high pressure located around the southern Yukon and the ridge to the southwest. The winds at the geostrophic level were from the west and northwest during the night, while during the day they were from the east-southeast. Figure 5 (a) illustrate the wind direction and Figure 5 (b) the wind speed over the site. Surface 4m height wind direction and speed are obtained from 10 min averaged sonic anemometer and upper level are derived from Doppler sodar at the ABL 55 m and the free atmosphere (FA) 165 m.

3.5 Drainage Flow Events – Turbulent variables

3.5.1 Case I

Wind direction observations at the surface observations showed a constant northwest wind direction between 15:00 UTC on 18 January and 15:00 UTC on 19 January as described in Figure 3 (a and b). At the beginning of the event the temperature in the surface layer ~ -22 C is observed to decrease in three hours to ~ -29 C as depicted in Figure 6 (a); vertical velocity (w) slowly increases Figure 6 (b) as the drainage start to penetrate the ABL turning the surface wind direction from the northwest Figure 6(c).

Significant changes are observed in the surface turbulent obtained by auto-covariance of turbulent velocities and cross-covariances to calculate TKE, u^* and τ_0. These variables are shown in Figure 7 (a) displaying the TKE (m^2s^{-2}), the increase of u^* (ms^{-1}) Figure 7(b) and surface shear stress (τ_0) on Figure 7(c). At the beginning, previous to the penetration of the drainage flow, the surface layer static stability was maintained to 1 °C / m of stratification. During drainage flow penetration (15:00 UTC – 21:00 UTC) the TKE increased to 0.15 m^2s^{-2}, u^* increased to 0.15 ms^{-1}, and τ_0 increased to 0.02 m^2s^2. The surface wind speed increased to 3.5 ms^{-1} and the temperature decreased by ~ 4 ° C. At 00:00 UTC, the temperature steadily decreased from -27.5 °C to -30 °C. After flow penetration the surface layer became stable as indicated by the calculation of the Ri_f number. The surface parameters remained approximately constant throughout the duration of the drainage flow penetration (see Figure 7).

The vertical structure of the ABL from the 00:00 UTC 18 January shows a surface-based inversion at 108 m from the radiosonde measurements at the NWS-NOAA station with winds from the south in the SABL and the FA. This height can also be retrieved in the backscatter signature of the sodar profile by searching the point of maximum gradient indicating the decaying of thermal turbulence structure in the ABL by the C_T^2 (see Figure 8). The ABL structure indicates the penetration of the drainage flow on 18 January at ~15:00 UTC. The flow lasted until 19 January at 15:00 UTC. The ABL wind speed in the period from 15:00 to 22:30 UTC did not exceed 2 ms^{-1}, but in the second period from 22:30 UTC to 17:30 UTC on 19 January, the wind speed exceeded 3 ms^{-1}. During the first period the drainage flow was 100 m deep while during second

period it was 95 m deep. Figure 8 displays the ABL vertical structure measured by sodar, from 20 m to 200 m, during the occurrence of the drainage flow. The color scale indicates an increase of the thermal turbulence C_T^2 as the drainage flow penetrates the ABL.

The C_T^2 coefficient in Figure 8 displays a variable structure in space-time indicating increasing stratification as the drainage flow dominates the flow in the ABL. The temperature turbulence is indicated to occur from the surface to a level below 40 m height and then reappears after 40 m up to a range between 80 m to 120 m. These spatial structures of turbulence in temperature responded differently to the drainage flow penetration since the lowest one is also forced by friction at the surface. Both turbulent structures overlap overtime in the period after 12:00 to 15:00 and between 21:00 and 00:00 and split for about six-hours before 06:00 to 12:00. Some short periods of time also display a complete disappearance of the thermal turbulence for example from 19:00 to 20:00

3.5.2 Case II

As sunset occurred around 01:20 UTC 7 February the initial ABL state showed a well-established surface-based inversion. The 00:00 UTC radiosonde from the NWS-NOAA radiosonde station PAFA showed an inversion of 98 m. The sodar showed ABL winds from the west and FA winds from the southeast Figure 4 (a and b). The vertical structure measured by sodar identified a drainage flow penetrating the ABL in the basin at 4:40 UTC. The flow penetration lasted until 07:30 UTC. Surface measurements show a constant west-northwest wind direction between 03:00 UTC and 07:30 UTC.

Wind direction observations at the surface observations showed an intermittent flow northwest wind direction between 00:00 UTC on 7 February and 00:00 UTC on 8 February as described in Figure 4 (a and b). At the beginning of the event the temperature in the surface layer ~ -8 C is observed to decrease in three hours to ~ -24 C as depicted in Figure 9 (a); vertical velocity (w) slowly increases Figure 9 (b) as the drainage start to penetrate the ABL turning the surface wind direction from the northwest Figure 9(c). Figure 9 (a) The surface turbulent magnitudes τ_0 increased from 0 to 0.04 m^2s^2, as well as the TKE from 0 to 0.1m^2s^{-2}, and u^* from 0.05 to 0.2 ms^{-1} as indicated in Figure 10 (a, b, and c).

The C_T^2 profile showed a C_T^2 minimum at the wind maximum and the C_T^2 maximum occurred at the wind shear layer between 90 m and 110m. The second drainage penetration event was observed by sodar between 09:10 and 11:10 UTC with vertical thermodynamic and wind profiles that were approximately similar to those in the first event.

This drainage episode was characterized by seven intermittent flows. The first event was a local flow penetrating by about ~270 minutes. The wind speed in the surface layer was maintained at 4 ms^{-1}. This flow broke up around 07:30 UTC with a change in surface wind direction from the southwest and a decrease in wind speed to < 1 ms^{-1}. The second drainage flow event occurred from 09:00 UTC to 12:00 UTC. The first half of this period sustained a surface wind speed that reached 4 ms^{-1}, but wind speed decreased to 2 ms^{-1} during the second half of this event. τ_0 increased from ~ 0 to 0.03 m^2s^2, the TKE increased to ~ 0.03 m^2s^{-2}, and u^* increased to 0.02 ms^{-1}. This event despite the shorter

duration, the changes in turbulent magnitudes in the surface displayed approximately the same micrometeorological changes. The five remaining events lasted for less than 30 min developing surface wind speed < 2 ms^{-1}. Calculation of surface turbulent magnitudes retrieved similar behavior to each other as compared to Case I. During the five intermittent pulses in the latter half of the day, strong stratification aloft occurred, indicated by the vertical C_T^2 in Figure 11. Figure 10 shows the changes in the surface turbulence parameters; TKE increased to 0.1 m^2s^2, and τ_0 increased to 0.03 m^2s^{-2}. The vertical structure of the ABL (see Figure 11) increases in C_T^2 as results of the increasing stratification.

In the upper ABL levels the drainage flow levels stratify the layers from 75 m – 125 m in five other intermittent pulses that occurred with wind speed < 2 ms^{-1} at 13:30, 15:20, 16:20, 19:10, and 20:30 UTC. The sodar shows evidence of the drainage pulse with an increase in vertical wind speed and increased C_T^2 values from 20 m – 120 m.

3.5.3 Case III

The sunset on the 6 March 2011 occurred at 03:20 UTC and the surface layer was in a near neutral state; flows in the FA were from the south-southeast and wind speeds at the 400 – 500 m level exceeded 8 ms^{-1}. The surface temperature was -9.5 °C and the surface stratification was 3 °C. The ABL begin its stratification on the surface as ground heating due to solar radiation ceased, giving rise to rapid radiational cooling at the surface and air layers aloft.

The drainage flow penetrated the surface layer with the early nocturnal inversion around 03:40– 03:50 UTC. Surface winds turned to the northwest direction between

06:10 – 06:20 UTC. The surface winds displayed a northwest to west-northwest wind direction between 04:30 UTC and 19:30 UTC. The static stratification immediately increased as the wind speed decreased to < 1 ms^{-1} at the surface. The TKE, u^*, and τ_0 are negligible as shown in Figure 13. During this period of time the surface layer was in a transitional period before it stabilized after the SABL is formed. As the initial drainage flow from the northwest direction penetrated the surface layer the TKE increased from ~0 to 0.2 m^2s^{-2}, u_* increased from ~0.05 to 0.2 ms^{-1}, and τ_0 increased from ~0 to 0.03 m^2s^{-2}, while the temperature decreased from -3 ^oC to -18 ^oC, a 15 ^oC decrease in 15 hours.

The calculated Ri_f resulted highly variable between negative and positive before the onset of the flow. Ri_f decreased and reached a steady value above 1 corresponding to a quasi-laminar flow. The end of the flow was indicated by the change of wind direction to the southeast and a reduction in the wind speed and in the surface micrometeorological parameters of τ_0, TKE, and u^* at 2000 UTC. The sun rose at 16:21 UTC and the surface-layer temperature began to rise at 1700 UTC. The most active turbulent activity was verified to occur between 0900 UTC and 1500 UTC when the surface parameters were at their maximum dynamic extension and wind speed was sustained, while the Ri_f number indicates a dynamic unstable flow. The vertical ABL structure observed by sodar indicates increasing C_T^2 values as shown in Figure 2 from 02:00 – 05:00 UTC and 09:00 – 15:00 UTC when, at the same time, the wind speed was accelerating in the vertical. This is an interruption of the drainage flow. The C_T^2 within the region decreased suddenly at 50 m – 100 m; at the surface high fluctuations occurred in the Ri_f number, TKE, and τ_0, and the wind speed decreased (see Figure 5). The flow re-stabilized

afterwards and became dynamically stable with Ri_f number ~2. After 18:00 UTC the Ri_f number variability increased as the flow broke down. The vertical profile of C_T^2 fluctuated at higher values as the ABL stratified and the flow broke up.

The vertical C_T^2 structure of the SABL, assumed a characteristic pronounced parabolic shape up to the top of the SABL when the drainage penetrates. The C_T^2 profiles from the sodar show a particular morphology, with higher values between 20 m - 60 m, and a minimum at the drainage flow wind speed maximum. A second maximum produced the strongest signal in the acoustic echo and represents a shear layer at 100 m. The extent of the drainage flow varied between 80 m and 120 m height. This shear layer induced stratification, entraining air into the ABL. The depth of the drainage flow penetration exhibited a parabolic shape in the wind speed profile between the surface and 200 m. Between 0900 – 1500 UTC the drainage flow wind speed accelerated from 3 ms^{-1} to 5 ms^{-1} with an increase the C_T^2, reaching a maximum peak wind speed at 6 ms^{-1}. Between 18:00 UTC and 21:00 UTC the flow decelerated from 5 ms^{-1} with an increase C_T^2 (See Figure 14).

3.6 Discussion

The turbulent state of the surface layer was observed by means of two instruments. The large aperture scintillometer across the basin (see Figure 2), able to evaluate the fluxes at a basin scale, and infer indirectly through Monin-Obukhov similarity theory the sensible heat flux (H_{LAS}) and the sonic anemometer calculated 5 min intervals eddy-covariance integration (H_{EC}). The H_{LAS} was averaged over 5 min using u^* and the Obukhov length (L) calculated after sonic anemometers. The LAS path covers a

length of 520 m. This allows probing the development of smalls scale flows and their interaction with the ABL. The H_{EC} and H_{LAS} are therefore compared to determine how the drainage flow interacts with the SABL developing different turbulent scales.

In Case I (See Figure 18), between 15:00 UTC and 00:00 UTC at the initiation of the flow $<H_{EC}>$ is -4 Wm^{-2} and $<H_{LAS}>$ is -8 Wm^{-2} without major flux differences. However in the period from 00:00 – 09:00 UT the time averaged turbulent fluxes values are: $<H_{LAS}>$ is -18 Wm^{-2} and $<H_{EC}>$ is -14 Wm^{-2} showing an increasing divergence between the measurements. This discrepancy is consistent with the increasing probability of wind direction change thus effecting the H_{EC} measurements. The H_{EC} and H_{LAS} measurements are therefore not convergent during this period (See Figure 6 a, 6 b, and 6 c).

In Case II, 7 February 2011 (See Figure 19), the H_{LAS} and H_{EC} decreases to an average value of -20 W/m^2 with the first sustain pulse. The second intermittent pulse has an H_{LAS} and H_{EC} average of -16 Wm^{-2}. The wind speed in the two intermittent pulses changes rapidly over a short period and the covariance requires 5 minutes of data before an integration can be calculated. These two measurements compares very well in time because of the magnitude of the turbulent scales developed in these situations can be captured simultaneously by both instruments. While, they diverge, during the sustained drainage flow case because 5 min EC resulted not enough time for the eddy-covariance system to reach the level of the LAS under a larger scale drainage flow.

H_{LAS} and H_{EC} measurements on Case III (See Figure 20) using 5 min integration diverge during the drainage flow. The average values of H_{EC} and H_{LAS} are -20 Wm^{-2} and

-40 Wm^{-2} during the sustained period. H_{LAS} is larger throughout the period (03:00 – 18:00 UTC) of the drainage flow while H_{EC} is smaller. When the flow is disrupted at ~ 12:00 UTC both H_{LAS} and H_{EC} measurements show similar spikes verifying a disruption in the flow. After the flow is reinitialized the fluxing returns to the initial vales before the disruption.

In the vertical, the drainage flow wind profile displays shear at 20 m – 40 m and at 80 m – 160 m. u^*, the surface friction and vertical wind shear are opposed at the surface by the vertical gradient of temperature or buoyancy. The surface layer is initially dominated by buoyancy given by L values during the initiation ranging for each case in the intervals : (0 – 50), (0 – 3), and (0 – 10). The Ri_f number at the initiation of each case: (-2 – 0), 2 - (-1), a-nd -10 – (-2). During the flow, the Ri_f number increases to ~ -2 in all case studies and the L increase to values between 50 – 100. This represents a shear-driven flow where u_* and vertical shear (< 50m) is an effect of the surface and dominates at the initiation, but is overcome by shear as the flow velocity increase during the case studies.

In terms of stratification occurring at the upper layers due to shear in Figures 15-17, Neff (1980; 1988) relates the scattering cross-section to vertical potential temperature gradient and wind shear. Hootman and Blumen (1983) and Neff and King (1988) showed an echogram facsimile in which drainage flow velocity and the echo intensity increases. Sakiyama (1990) presents another echogram that clearly distinguishes between the echo intensities made by a drainage flow and by the convective plumes that arise from surface

heating. C_T^2 in each drainage case from Neff (1988) is dominated by mixing in terms of coefficient of heat and the vertical potential temperature.

In Case I, the sodar measurements taken on 18-19 January 2011 show an increase of drainage flow wind speed from 00:00 UTC to 03:00 UTC (See Figure 17c-17d). Vertical shear is present between 50 m – 120 m. This shear is not affected by the surface. The stratification represented by the vertical gradient of potential temperature is opposed only by the wind shear in the upper layers. The surface friction has no major effect between 50 m – 120 m. The thermal turbulence dominates the upper layers induced by local wind shear and stratification. At the surface, below 50 m the shear-driven thermal turbulence is driven the surface effect in terms of u^* and wind shear. In Figure 17a, shows an increase of drainage flow wind between 0000 UTC and 0300 UTC. At the edges of the drainage flow away from the maximum wind speed the shear stress caused by the increased wind speed induced a greater amount of thermal turbulence as reflected (See Figure 17c). This indicates an increase in stratification, based on the C_T^2 of the layers below 20 m and between 50 m and 120 m. At the surface layer, temperature decreased and the stratification between 20 m – 40 m increases.

In Case II, the sodar measurements taken on 7 February 2011 show an increase of drainage flow wind speed from 04:00 UTC – 07:00 UTC (See Figure 18a). The thermal turbulence dominates the upper induced by wind driven shear. At the edges of the drainage flow away from the maximum wind speed the shear stress is increased by the acceleration in wind speed, which induces the C_T^2 to rise in certain layers creating greater

thermal turbulence (See Figure 18a). The values of C_T^2 indicate an increase in stratification between 20 m – 40 m and between 50 m and 110 m (See Figure 18c).

In Case III, Figure 19b shows increase in the drainage flow wind speed profile (height of drainage flow ~ 95 m). Above 80 m the wind direction changes rapidly by 180° to the southeast, leading to a greater amount of shear stress from wind shear and an increase in temperature turbulence (See Figure 19 a and b). The surface layer wind speed at 0700 UTC was initially 3.5 ms^{-1} and increased to 4 ms^{-1} at 1100 UTC. The stratification occurred between 20 m - 40 m and between 80 m - 120 m (See Figure 19c).

3.7 Conclusions

This paper presented observational results of surface layer turbulence and ABL structure variations during the occurrence of small-scale ABL drainage flows during winters at high-latitudes. This paper presented three selected cases that developed different temporal behavior and signatures at the surface and throughout the vertical ABL structure. Of particular interest are the near-surface mixing and the thermal turbulence in the vertical structure of the ABL that this small-scale flow introduced. After the drainage flow stopped, the surface layer strongly re-stratified. In all cases the drainage flows observed in the vertical by sodar are represented by a parabolic-like wind speed profile as has been observed in other studies (Doran and Horst, 1983; Horst and Doran, 1986; Sakiyama, 1990).

During the January 18 –19 case study I, the vertical flow grew to an average height of 135 m. The C_T^2 increased throughout the period with the increase of the drainage flow wind speed. The flow increased in height during the first half of this study

and decreased during the second half. The temperature decreased by ~4 ° C and the average heat flux was -10 Wm^{-2} for the first third of the deep-winter case of January 18 – 19. For the rest of this study the average heat flux ranged from ~ 0 Wm^{-2} to -5 Wm^{-2}. The duration of TKE, τ_0, and u_* all increased exponentially and then remained steady at constant values.

During the February 7 case study II the vertical flow first grew to an average height of 125 m. The intermittent flows after 12:00 UTC decreased in height from 105 m to 85 m. Each drainage flow pulse exhibited an increase in C_T^2 and decreases in wind speed and height as time progressed. The first pulse was 3 hours long, the second pulse 1.5 hours long, and the other pulses were shorter. The effectiveness of the drainage pulse is strong for the 7 February case study. The temperature decreased 11° C and the average heat flux was -40 Wm^{-2} during the first intermittent pulse; the other pulses exhibited a lower negative average heat flux in the range of -10 and -5 Wm^{-2}.

During the March 6 case study III the vertical flow grew to an average height of 105 m and was sustained for 9.5 hours. The C_T^2 increases represented a change in flow and drainage flow penetration into the lowest ABL layers. The flow increased in height during the first half of this study period and decreased during the second half. During the 6 March case study the temperature decreased by 19 ° C; the heat flux averaged -20 Wm^{-2} for the first half and -6 Wm^{-2} for the second half. However, a contributing factor in this March 6 case is sustained winds of ~4 ms^{-1} for 9 hours. The TKE, τ_0, and u_* all increased exponentially and steadily at constant values throughout this period, except when the flow was interrupted. In all three cases, the Ri_f number was ~1 or greater during the time

interval when the drainage flow was present, indicating a quasi-laminar and dynamically-stable flow.

In conclusion, the synoptic meteorological configuration for each case presents the possibility of an inter-valley density flow exchange at a local scale. Synoptic influence plays an important role in the occurrence of drainage flow. All cases occurred under a surface high pressure forcing regional clear skies. During the late winter, because of the diurnal effect of solar radiation the study case fundamentally differ from the deep-winter cases. The drainage event under analysis developed during the night of 5 March 2011 and the day of 6 March 2011. This drainage event is representative of drainage flow cases during the late winter, in particular from March 1 to 10. The weak pressure gradient force and synoptic-scale forcing from surface high pressure is characterized by weak winds and clear skies, which in turn strongly drive the radiative cooling in the basins.

The three cases studies described are: Case I is characterized by a sustained flow lasting ~18 hrs in the deep winter, Case II is characterized by intermittent pulses occurred < 3 hrs in the deep winter, and Case III is characterized by a sustained flow lasting for 9 ½ hours in late winter. Together with surface measurements and vertical measurements from a monostatic Doppler sodar it was found that stratification occur in the terms of C_T^2 (i.e. thermal turbulence) resulting from increased flow speed. The drainage flow seen in the first ~ 150 m of the SABL caused stratification and formed different layers within the SABL.

3.8 References

Benson, C.S., 1965: Ice Fog: Low Temperature Air Pollution, Defined with Fairbanks, Alaska as Type Locality. College, Alaska: University of Alaska Fairbanks, Geophysical Institute, pp: 134.

Benson, C. S. ,1970a: Ice Fog. Weather. **25**, 11-18.

Benson, C. S., 1970b: Ice Fog: Low Temperature Air Pollution. CRREL Research Report 121.

Benson, .C.S., Weller, G. 1970: A Study of Low-Level Winds in the Vicinity of Fairbanks, Alaska. Report to Earth Resources Co., Geophyiscal Institute, University of Alaska.

Beran, D., Hooke, W., and Clifford, S. 1973: Acoustic Echo-Sounding Techniques and their Application to Gravity-Wave, Turbulence, and Stability Studies. *Boundary-Layer Meteor*. **4**,133-153.

Bowling, S.A., T. Ohtake, and C.S. Benson, 1968: Winter pressure systems and ice fog in Fairbanks, Alaska. *J. Appl. Meteor.* **7**, 961-968.

Brown, E.H., and F.F. Hall, Jr. 1978: Advances in atmospheric acoustics. *Rev. Geophys. Space Phys*. 16, 47-110.

Clements, C. B., C. D. Whiteman, and J. D. Horel, 2003: Cold-Air-Pool Structure and Evolution in a Mountain Basin: Peter Sinks, Utah. *J. Appl. Meteor*., **42**, 752–768.

De Bruin, H.A.R., W.M.L. Meijninger, A.S. Smedman, and M. Magnusson, 2002: Displaced-Beam Small Aperture Scintillometer Test. Part I: The Wintex Data-Set. *Boundary Layer Meteor.* **105**, 129-148.

Doran, J.C. and T.W. Horst, 1983: Observations and Models of Simple Nocturnal Slope Flows. *J. Atmos. Sci.* **40**, 708-717.

Holmgren, B., L. Spears, C. Wilson, and C.S. Benson, 1975: Acoustic Soundings of the Fairbanks Temperature Inversions. *Climate of the Arctic: Proceedings of the AAAS-AMS conference, Fairbanks, Alaska. 1973. Weller, G. and S.A. Bowling, Eds., Geophysical Institute, University of Alaska,* 293-306.

Hootman, B.W. and W. Blumen, 1983: Analysis of Nighttime Drainage Winds in Boulder, Colorado during 1980. *Mon. Wea. Rev.* **111**, 1052-1061.

Horst, T.W. and J.C. Doran, 1986: Nocturnal Drainage Flow on Simple Slopes. *Bound-Layer Meteor*. **34**, 263-286.

Kaimal, J.C. and J.J. Finnigan, 1994: Atmospheric boundary layer flows: their structure and measurement. Oxford University Press.

Kleissl, J, J. S.H. Gomez, S.H. Hong, J.M.H. Hendrickx, T. Rahn, and W.L. Defoor, 2008: Large aperture scintillometer intercomparison study. *Boundary-Layer Meteor.* **128**, 133-150.

Lee, X., W. Massman, and B. Law, 2004: Editors Handbook of Micrometeorology. A guide for surface flux measurments and analysis. Kluwer Academic Publishers, Dordrecht, Netherlands.

Mahrt, L., 2011: The Near-Calm Stable Boundary Layer. *Boundary-Layer Meteorol*. **140**, 343-360.

Mayfield, J. and G.J. Fochesatto, 2011: Influence of Synoptic Setup on the Small Scales flow occurrence The Layered Structure of the Winter Atmospheric Boundary Layer in the Interior of Alaska. *J. Appl. Meteorol. Clim. In Review*

Moelders, N., and G. Kramm, 2010: A Case Study on Wintertime Inversions in Interior Alaska with WRF. *Atmos. Res.,* **95**, 314-332.

Neff, W.D. 1980: An Observational And Numerical Study Of The Atmospheric Boundary Layer Overlying The East Antarctic Ice Sheet. Ph.D. Thesis University of Colorado, Boulder, Colorado.

Neff, W.D., 1988: Observations of Complex Terrain Flows Using Acoustic Sounders: Echo Interpretation. *Boundary-Layer Meteor.* 1988, 40, 363-392.

Neff, W.D. and C.W. King, 1987: Observations of Complex-Terrain Flows Using Acoustic Sounders - Experiments, Topography, and Winds. *Boundary-Layer Meteor.,* **40**, 363-392.

Sakiyama, S.K., 1990: Drainage Flow Characteristics and Inversion Breakup in Two Alberta Mountain Valleys. *J. Appl. Meteor*. **29**, 1015-1030.

Vickers, D. and L. Mahrt, 1997: Quality Control and Flux Sampling Problems for Tower and Aircraft Data. *J. Atmos. Oceanic Technol*., **14**, 512–526.

Wendler, G. and K.. Jayaweera, 1972: Some Measurements of the Development of the Surface Inversion in Central Alaska During Winter. *Pure and Applied Geophysics*. **99**, 209-221.

Wilczak, J., S. Oncley, S. Stage, 2001: Sonic Anemometer tilt Correction Algorithms. *Boundary-Layer Meteor*. **99**, 127-150.

3.9 Figures

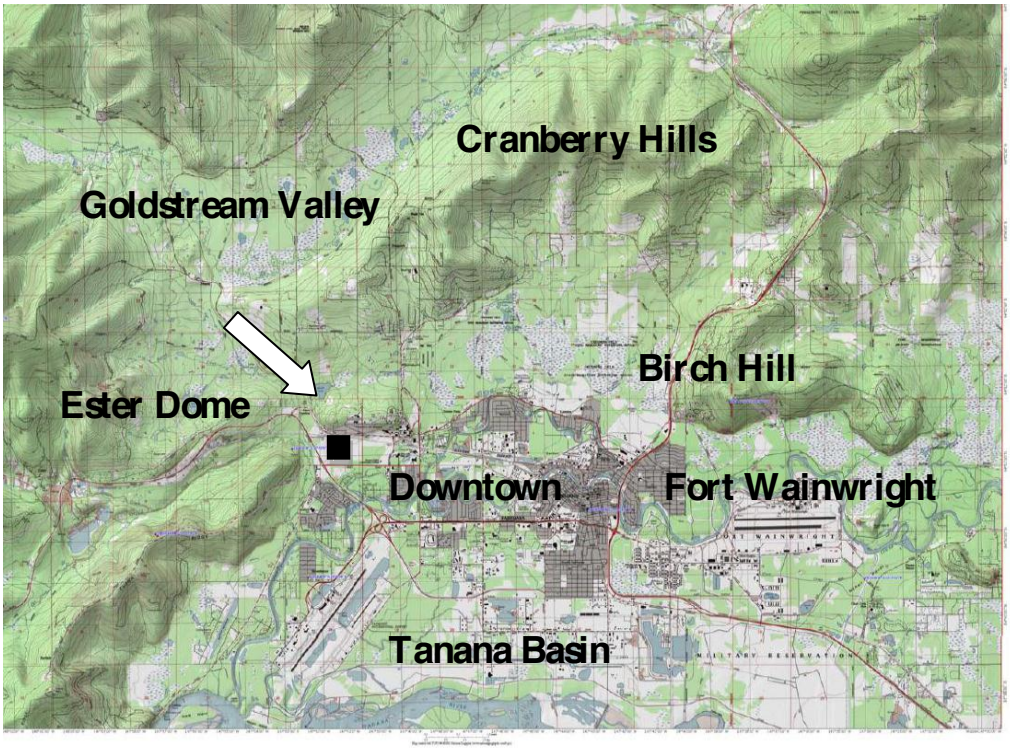

Figure 1. Topographic Map of the Fairbanks Area. '■' represents the Experiment Site. '=>' represents motion of flow.

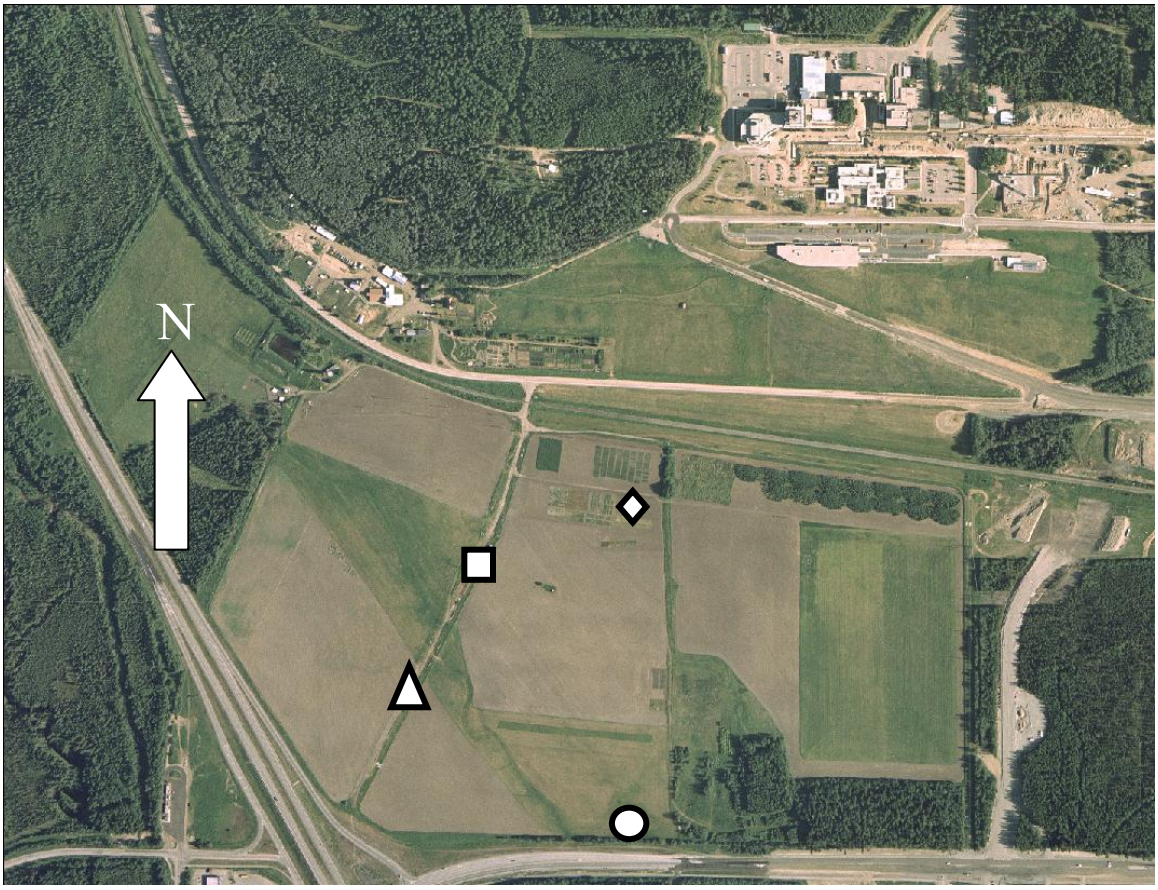

Figure 2. Aerial photo of the UAF campus farm. The UAF Campus Farm extends 1.2 km west-to-east and 700 m north-to-south. The instruments were located ~ 400 m from the major aerodynamic perturbations to the northwest causes by low forested hills to the northwest. ‘‘Δ’ represents the micrometeorogical tower, ‘◊’ represents the BLS transmitter, ‘○’ represents the BLS receiver, and ‘□’ represents the acoustic sounder. Courtesy of Alan Thone UAF Farm Manager.

Figure 3. 18-19 January Mean Wind Direction and Wind Speed Evolution (a) Represents the wind direction 18-19 January 2011 in the surface layer and in upper ABL layers. The black solid line represents 10 min average wind direction measured by sonic anemometer 4m height, the black dash line represent the BL wind speed at 55 m measured by the sodar and the gray line represent the 165 m measured by the sodar. (b) Represents the wind speed 18-20 January 2011 in the surface layer and in upper ABL layers. The black solid line represents 10 min average wind direction measured by sonic anemometer 4m height, the black dash line represent the BL wind speed at 55 m measured by the sodar and the gray line represent the 165 m measured by the sodar.

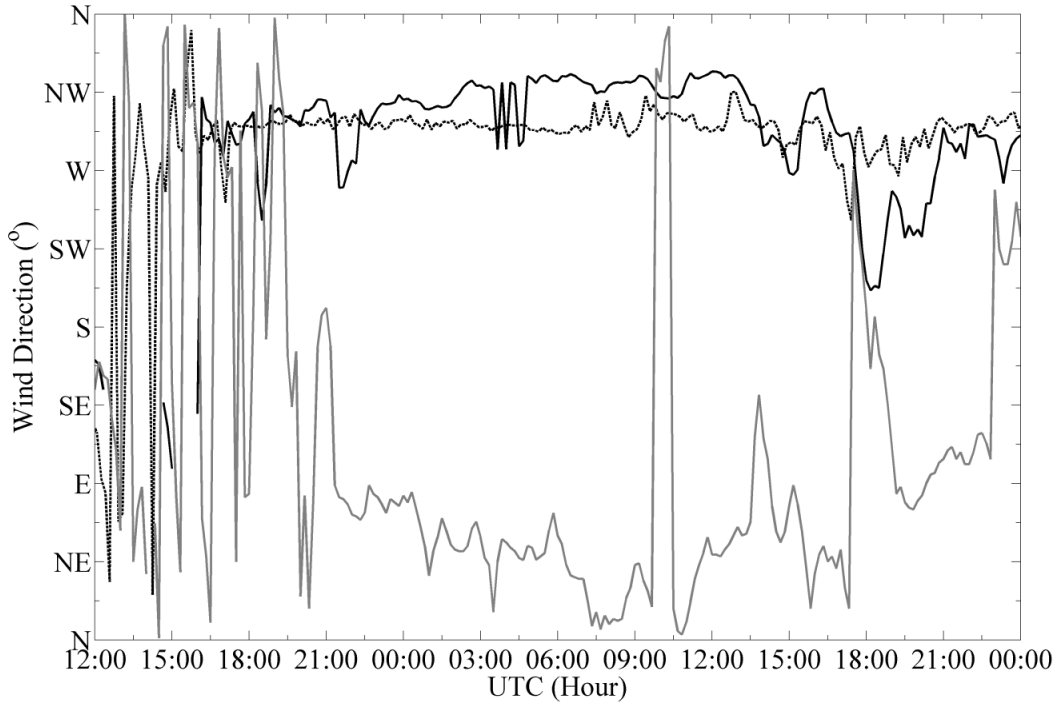

Figure 3a

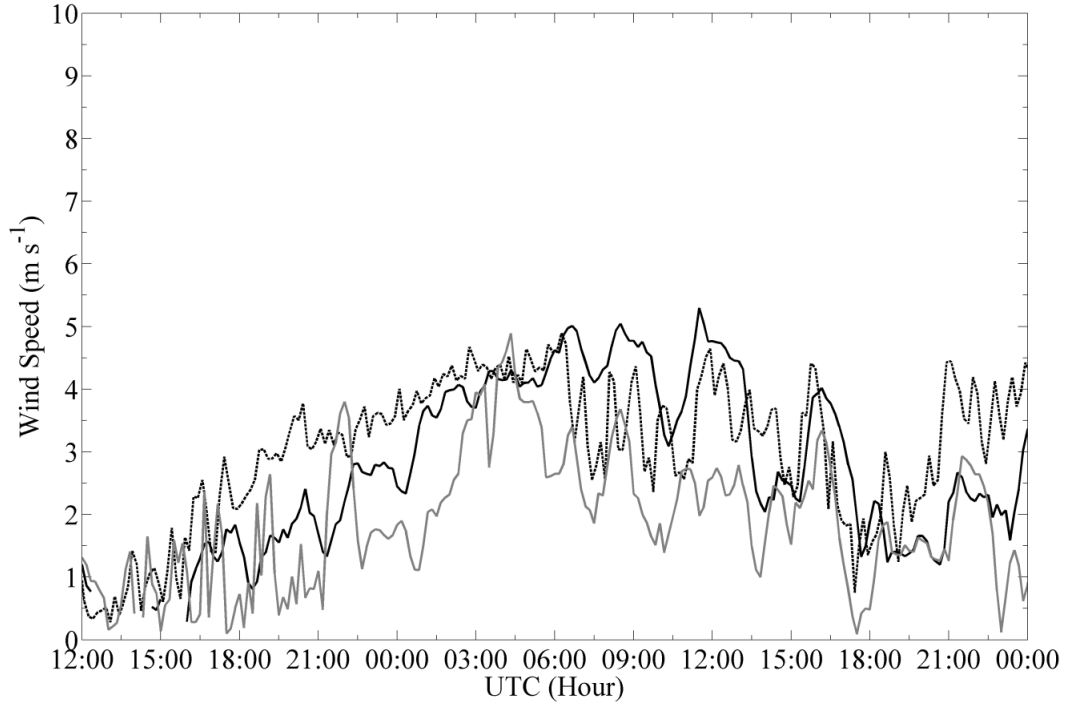

Figure 3b

Figure 4 7 February Mean Wind Direction and Wind Speed Evolution (a) Represents the wind direction 7 Feburary 2011 the surface layer and in upper ABL layers. The black solid line represents 10 min average wind direction measured by sonic anemometer 4m height, the black dash line represent the BL wind speed at 55 m measured by the sodar and the gray line represent the 165 m measured by the sodar. (b) Represents the wind speed 7 Feburary 2011 in the surface layer and in upper ABL layers. The black solid line represents 10 min average wind direction measured by sonic anemometer 4m height, the black dash line represent the BL wind speed at 55 m measured by the sodar and the gray line represent the 165 m measured by the sodar.

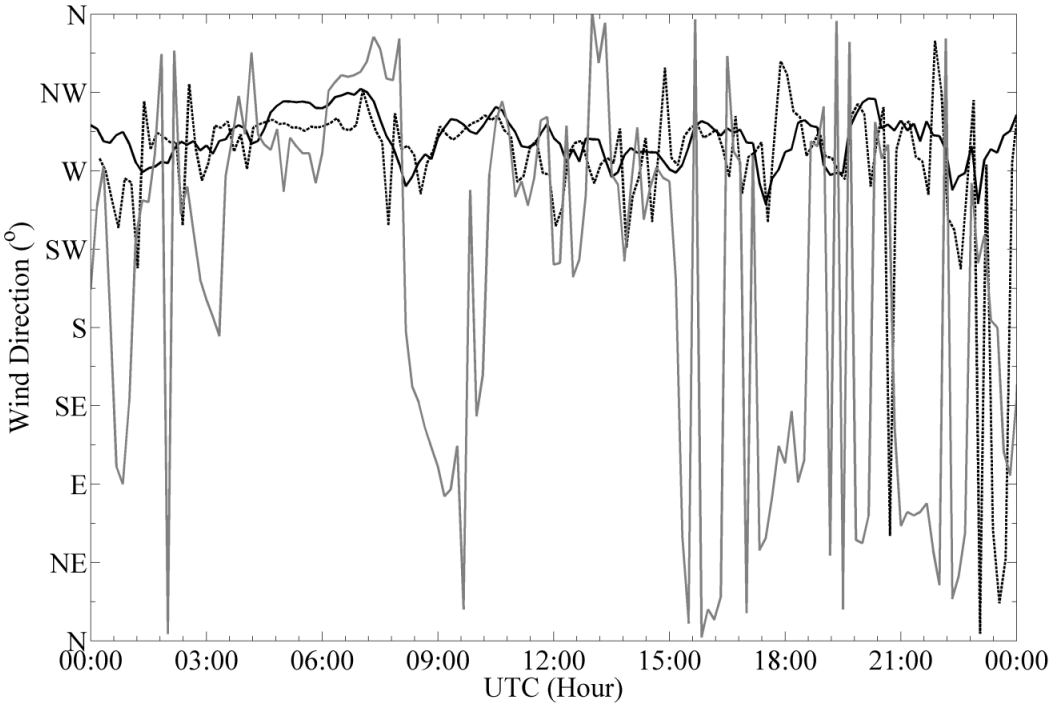

Figure 4a

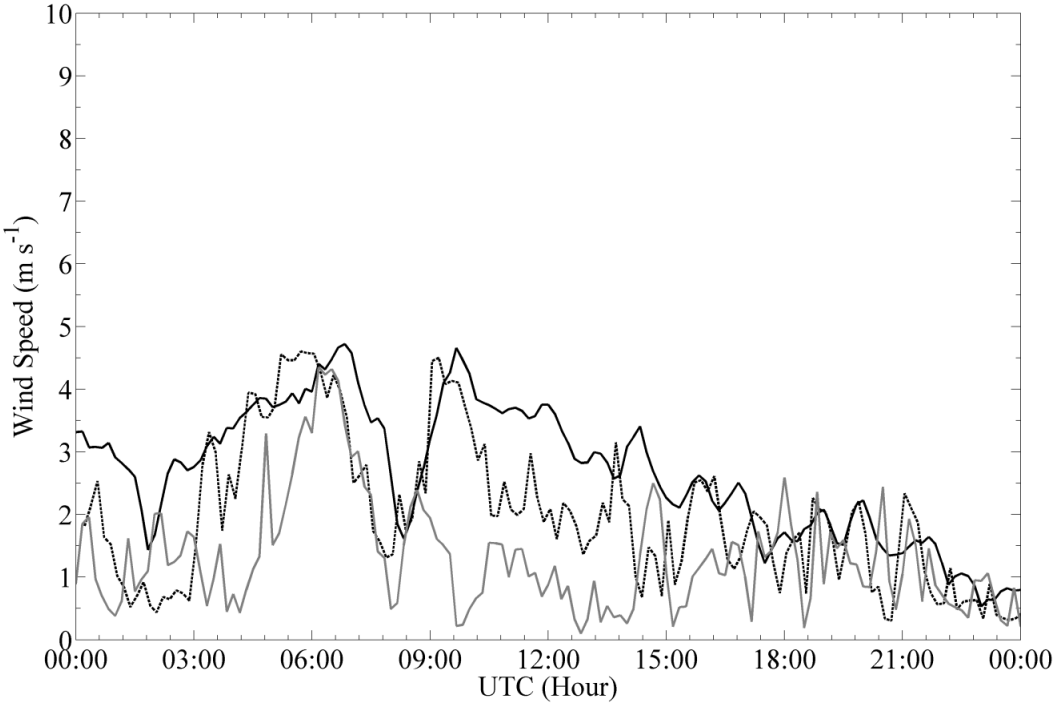

Figure 4b

Figure 5. 6 March Mean Wind Direction and Wind Speed Evolution (a) Represents the wind direction 6 March 2011 in the surface layer and in upper ABL layers. The black solid line represents 10 min average wind direction measured by sonic anemometer 4m height, the black dash line represent the BL wind speed at 55 m measured by the sodar and the gray line represent the 165 m measured by the sodar. (b) Represents the wind speed 6 March 2011 in the surface layer and in upper ABL layers. The black solid line represents 10 min average wind direction measured by sonic anemometer 4m height, the black dash line represent the BL wind speed at 55 m measured by the sodar and the gray line represent the 165 m measured by the sodar.

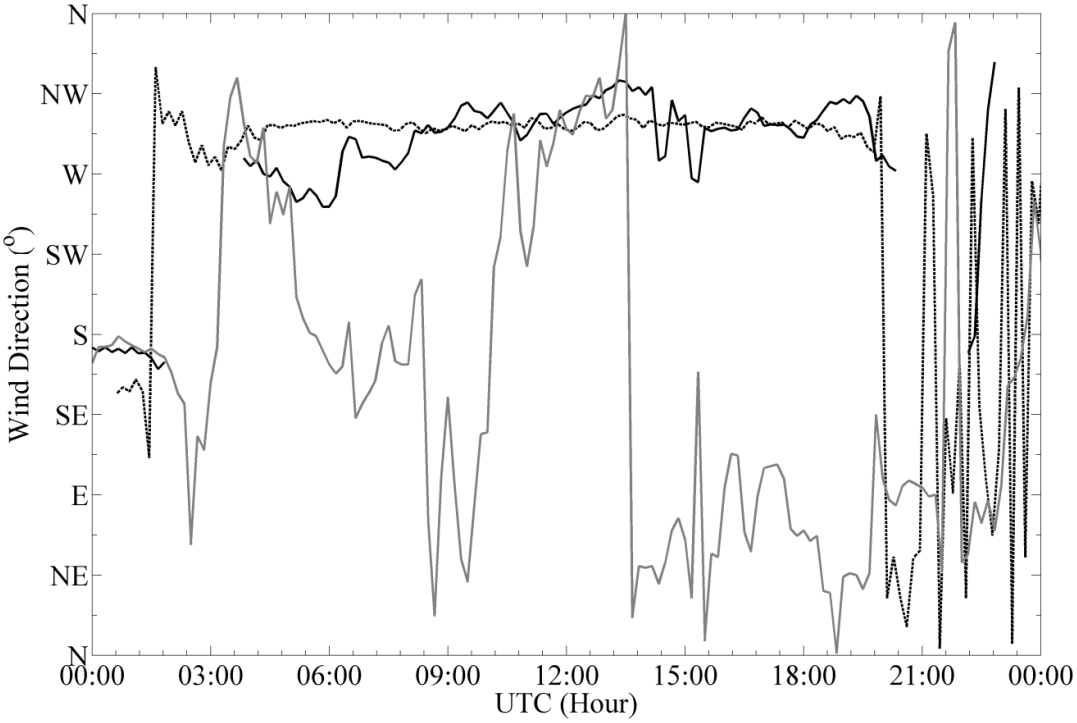

Figure 5a

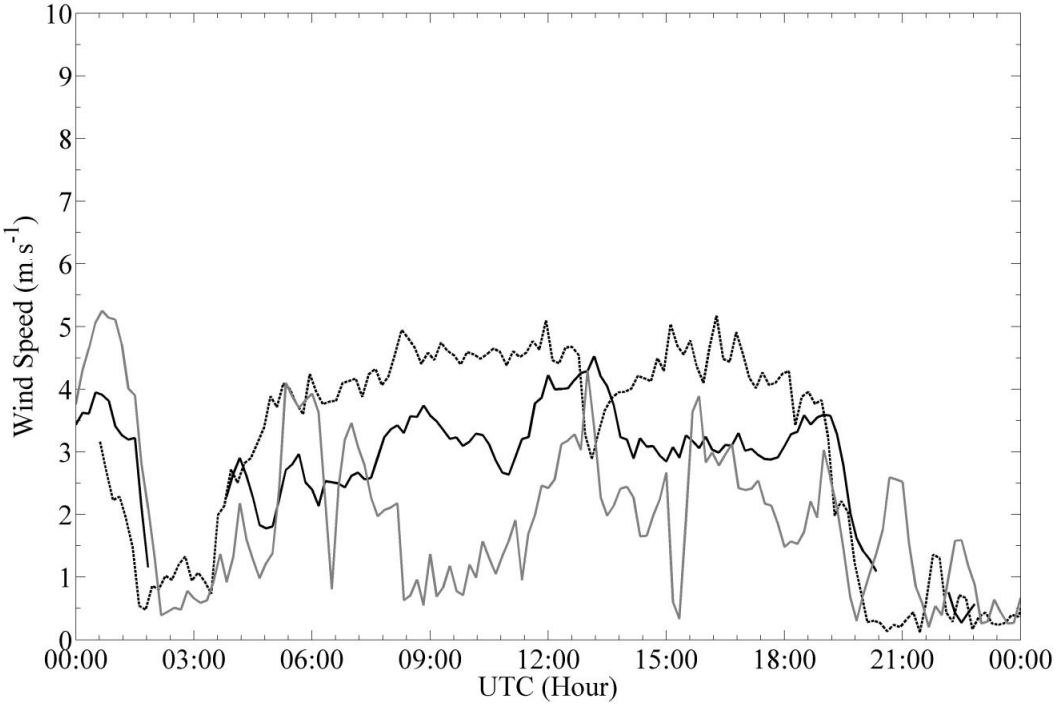

Figure 5b

Figure 6. (a). Surface layer turbulent flows for Case I, measured at 10 Hz, 4 m height sonic anemometer during case I: 18-20 January 2011. Figure 6(a) represents the sonic temperature (equivalent to virtual temperature). Figure 6(b) represents the vertical velocity. Figure 6 (c) presents the components u and v of the horizontal wind speed.

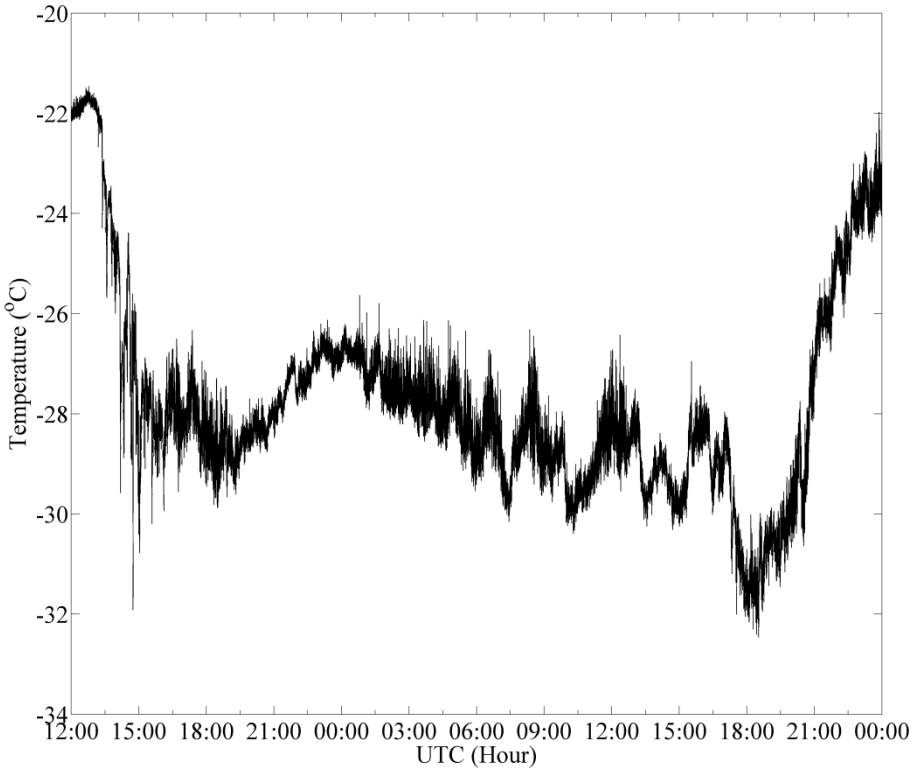

Figure 6a

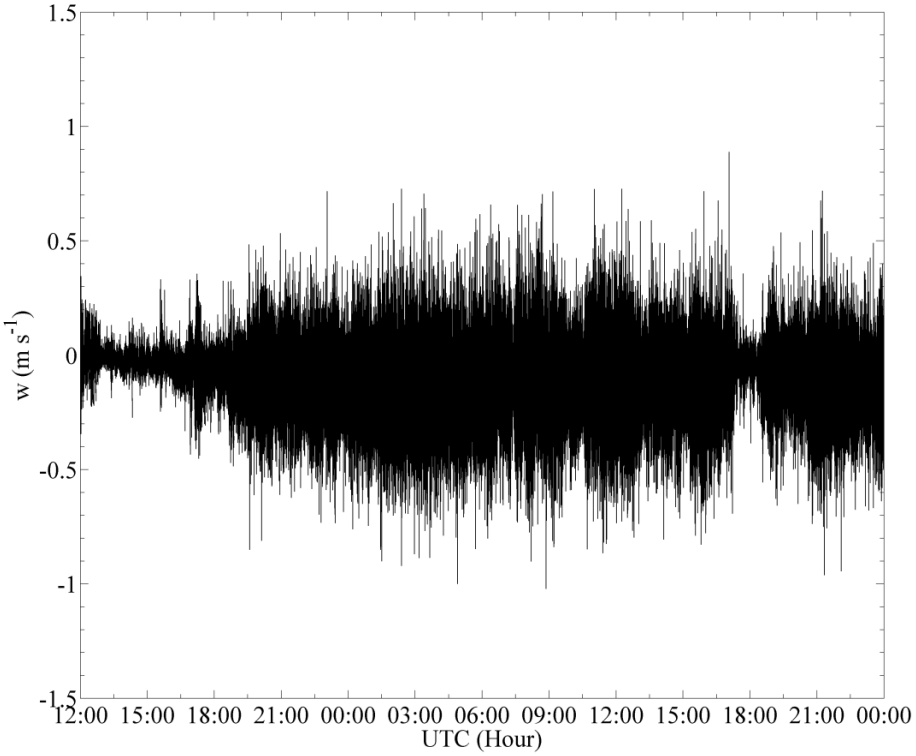

Figure 6b

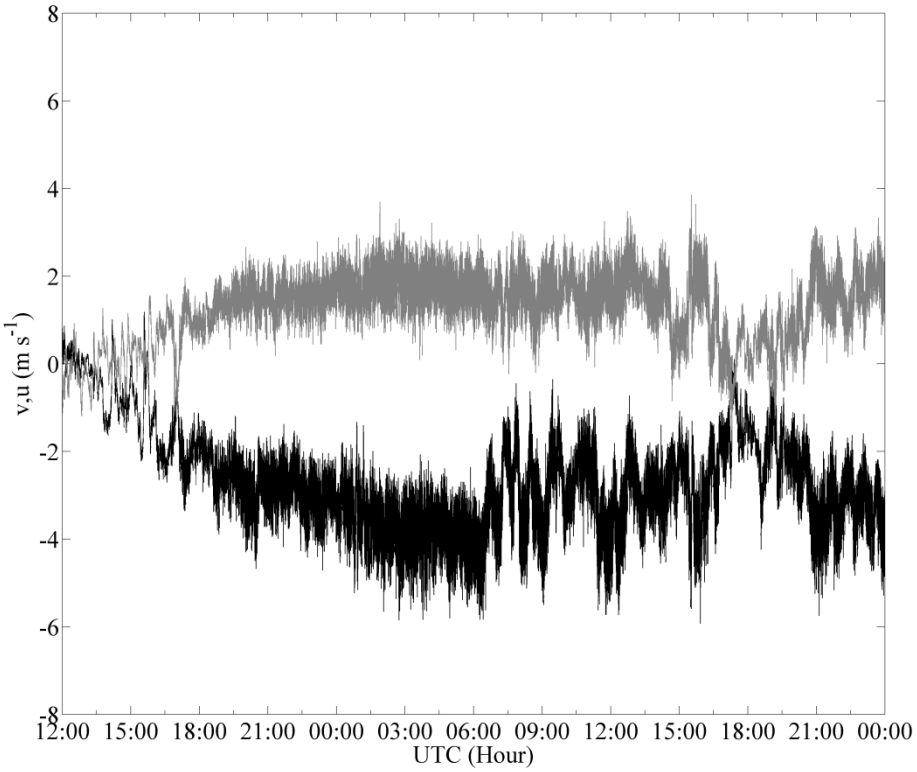

Figures 6 continued Figure 6c

Figure 7. (a) Surface layer turbulent parameters for Case I at 4 m height. Figure 7 (a) represents TKE, Figure 7 (b) represents friction velocity and Figure 7 (c) the surface shear stress.

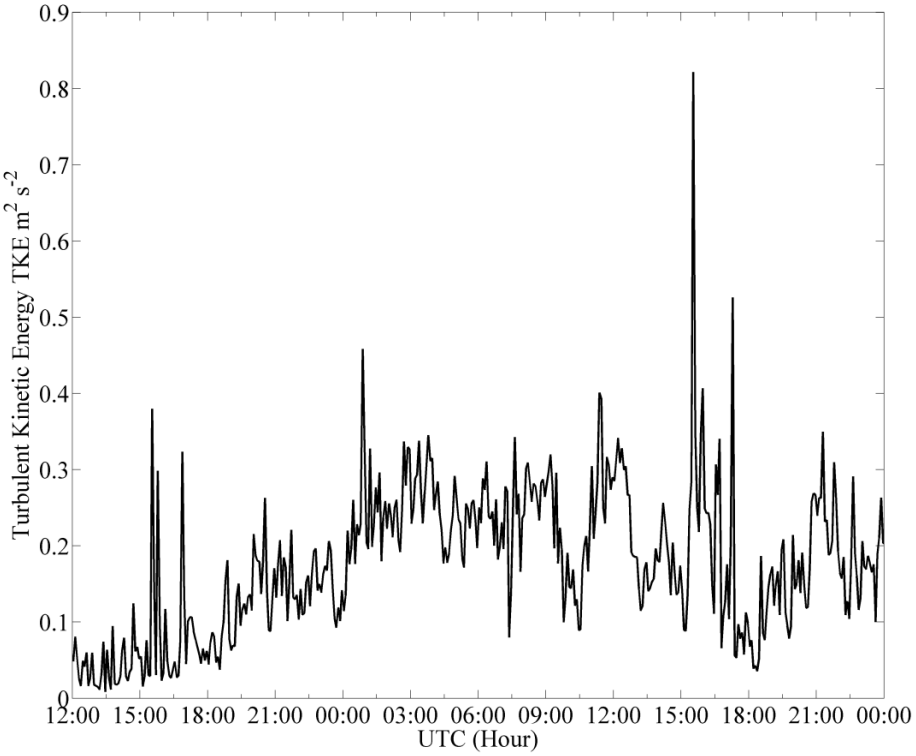

Figure 7a

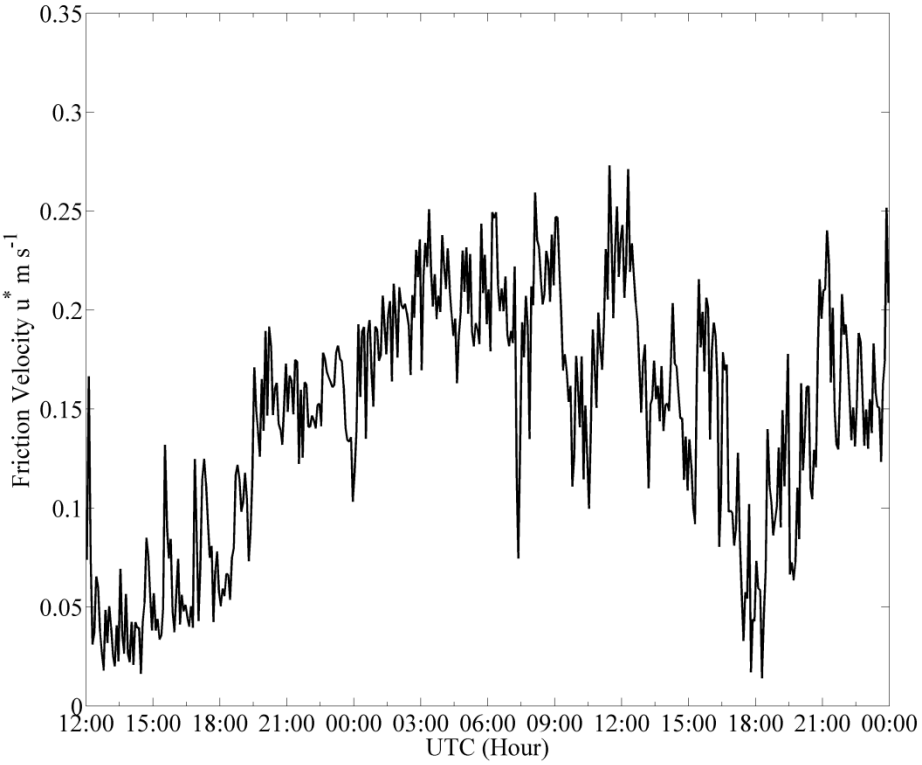

Figure 7b

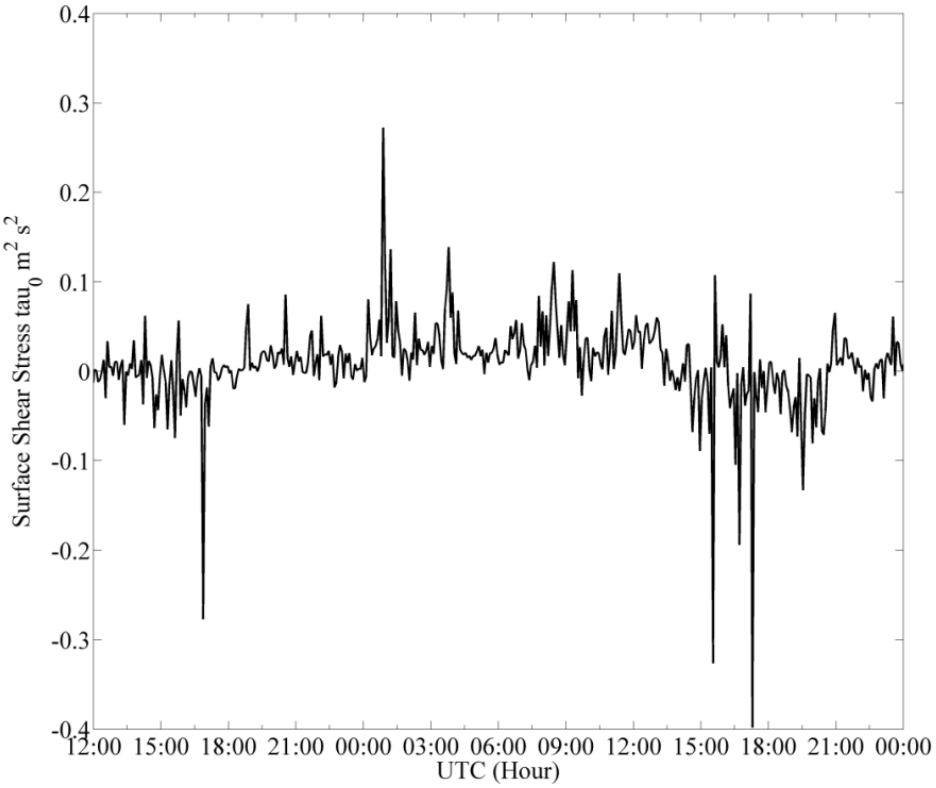

Figures 7 continued Figure 7c

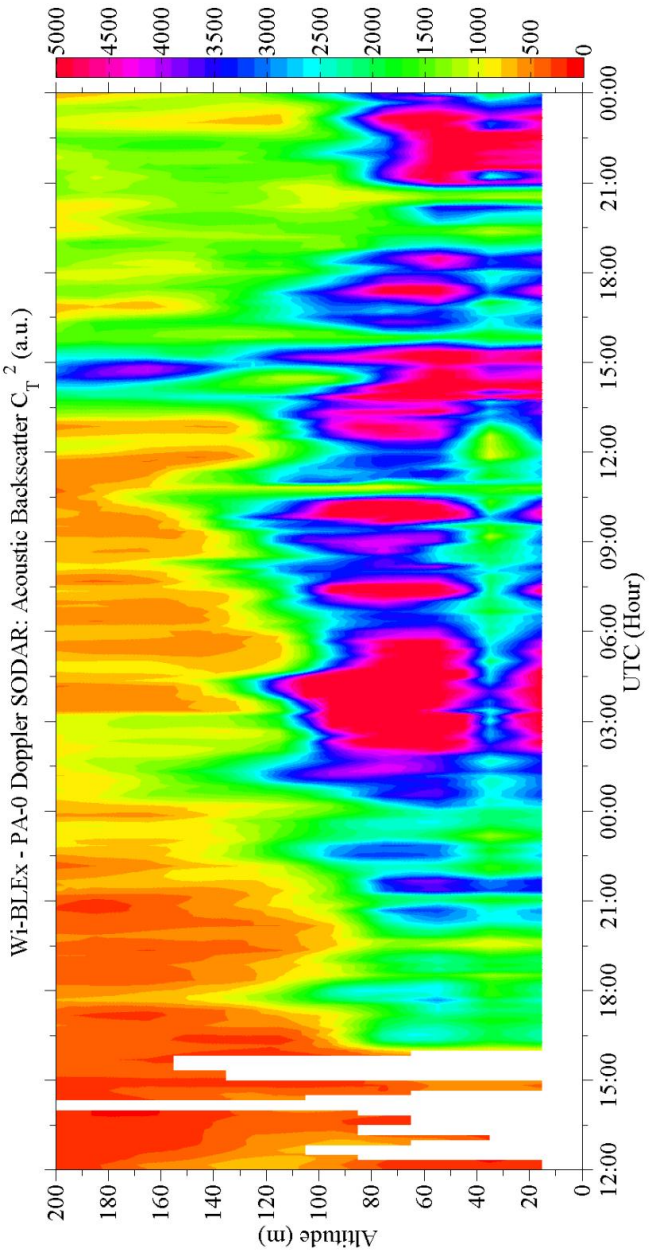

Figure 8. Vertical structure of the ABL from 18 – 20 January. The sodar represents the thermal turbulent structure coefficient C_T^2 in arbitrary units with time resolution of 10 min and vertical resolution of 10 m.

Figure 9. (a) Surface layer turbulent flows for Case II, measured at 10 Hz, 4 m height sonic anemometer during case II: 7 February 2011. Figure 6(a) represents the sonic temperature (equivalent to virtual temperature). Figure 6(b) represents the vertical velocity. Figure 6 (c) presents the components u and v of the horizontal wind speed.

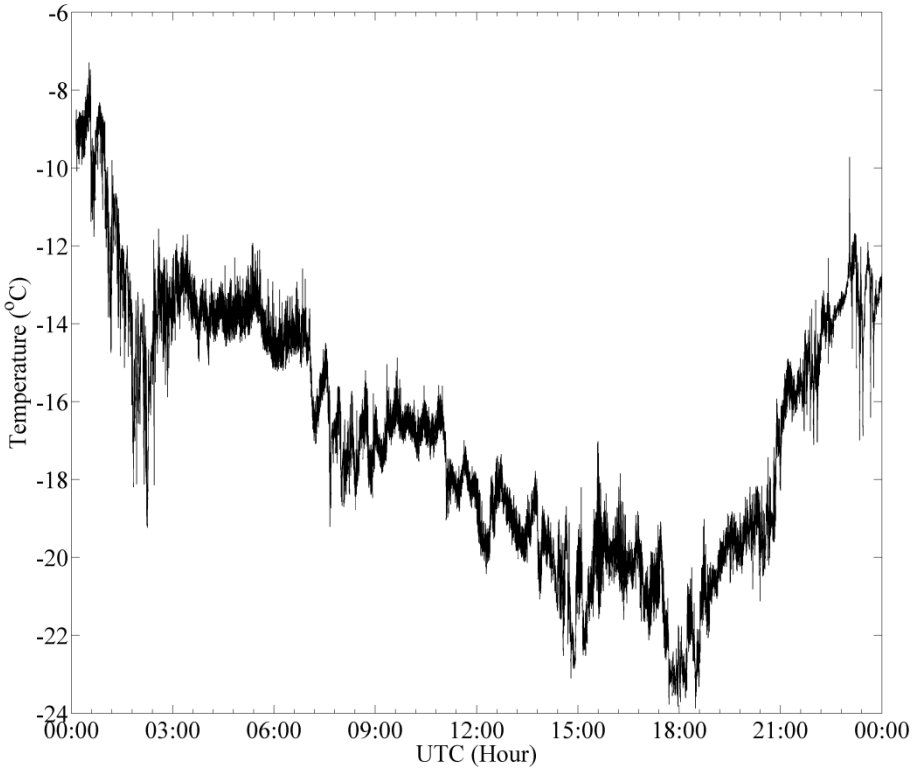

Figure 9a

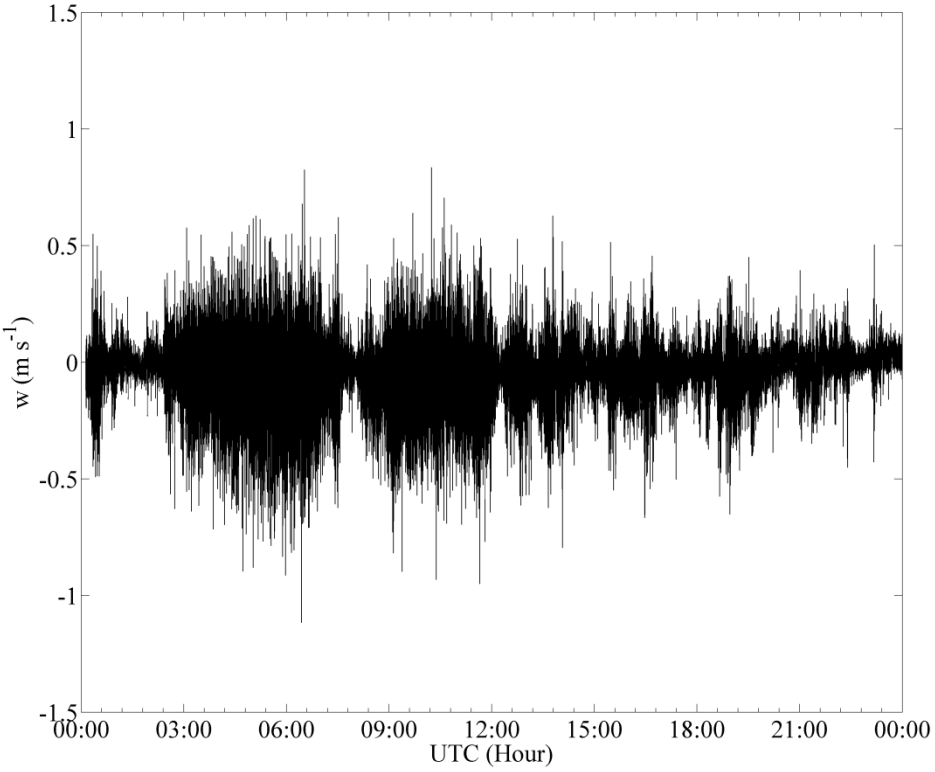

Figure 9b

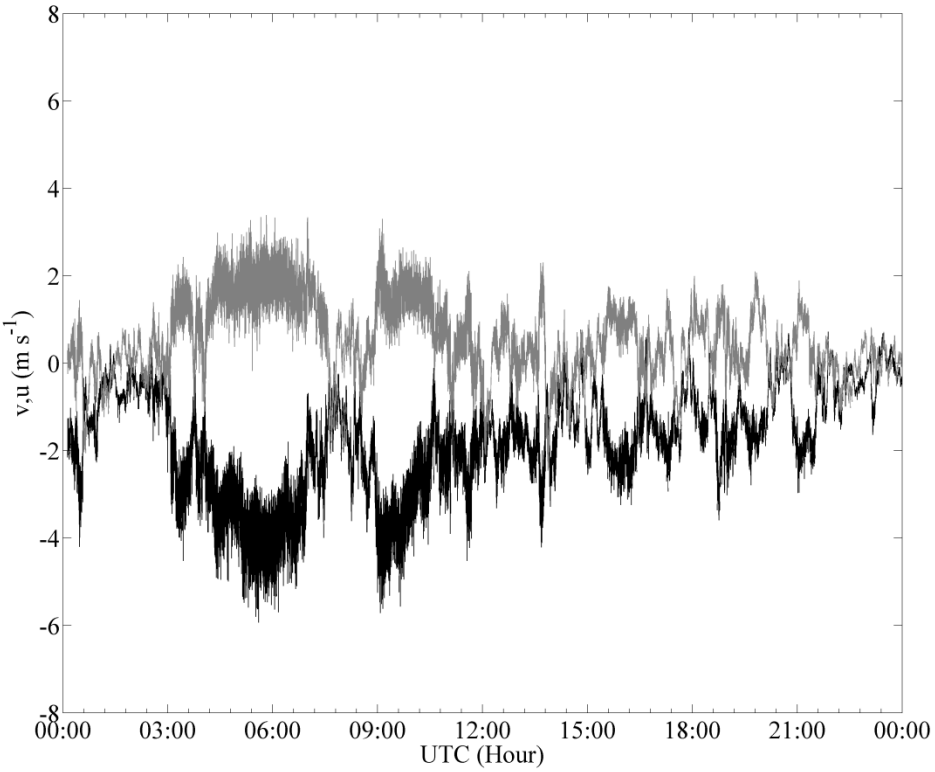

Figures 9 continued Figure 9c

Figure 10. Surface layer turbulent parameters for Case II at 4 m height. Figure 13 (a) represents TKE, Figure 13 (b) represents friction velocity and Figure 13 (c) the surface shear stress.

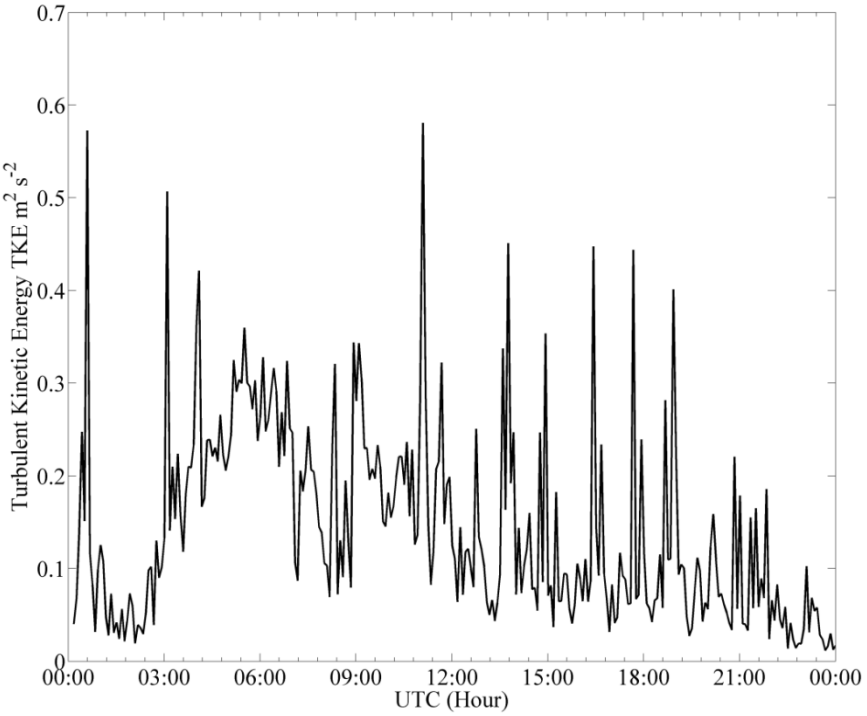

Figure 10a

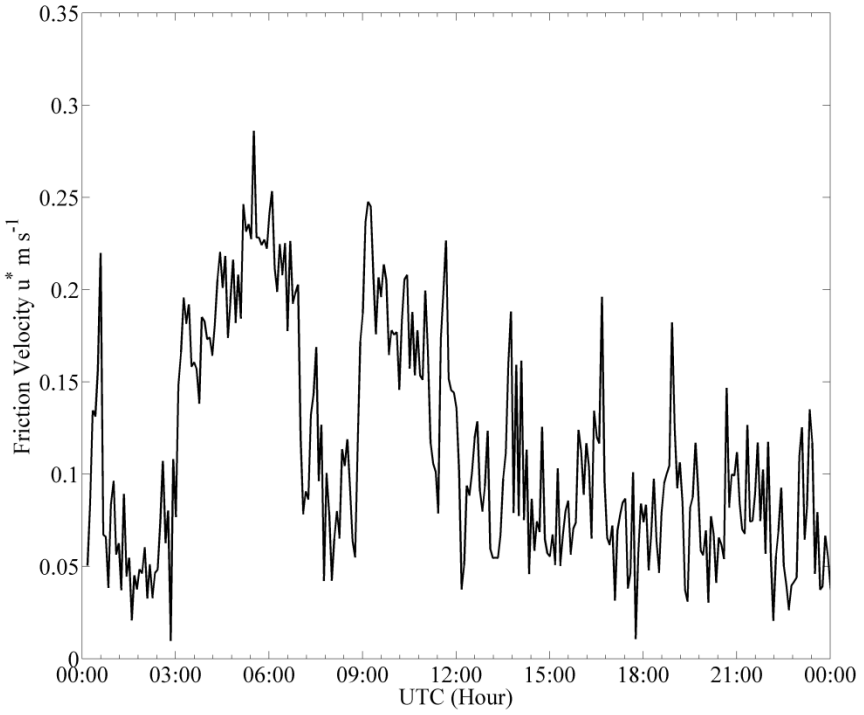

Figure 10b

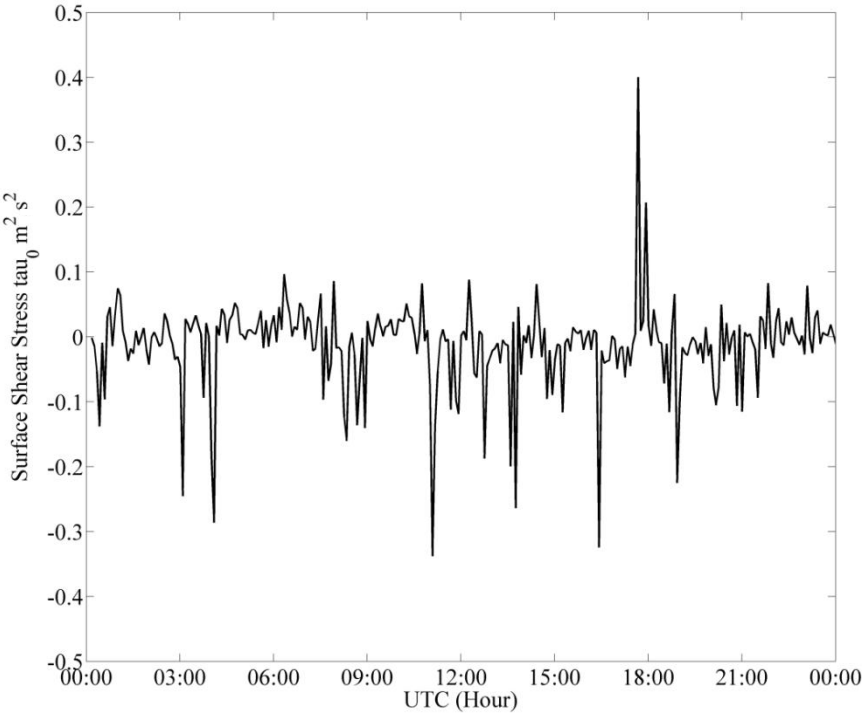

Figures 10 continued Figure 10c

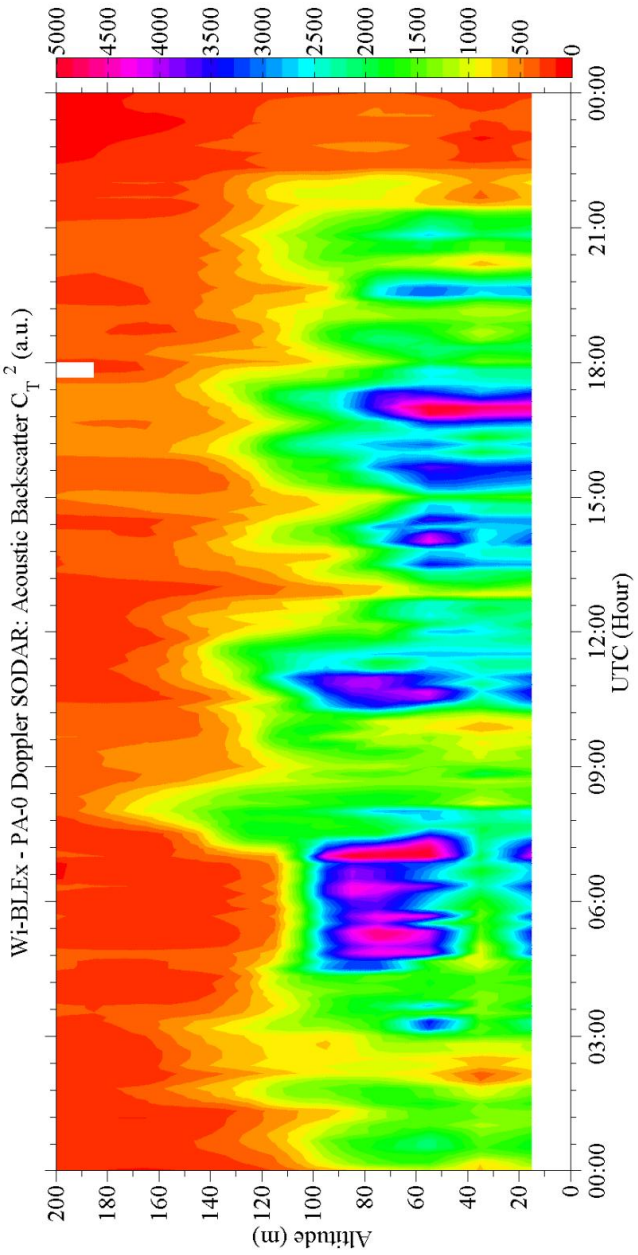

Figure 11. Vertical structure of the ABL from 7 February sodar represented by the thermal turbulent structure coefficient C_T^2 in arbitrary units with time resolution of 10 min and vertical resolution of 10 m.

Figure 12. (a). Surface layer turbulent flow for Case III, measured at 10 Hz, 4 m height sonic anemometer during Case III: 6 March 2011. Figure 6(a) represents the sonic temperature (equivalent to virtual temperature). Figure 6(b) represents the vertical velocity. Figure 6 (c) presents the components u and v of the horizontal wind speed.

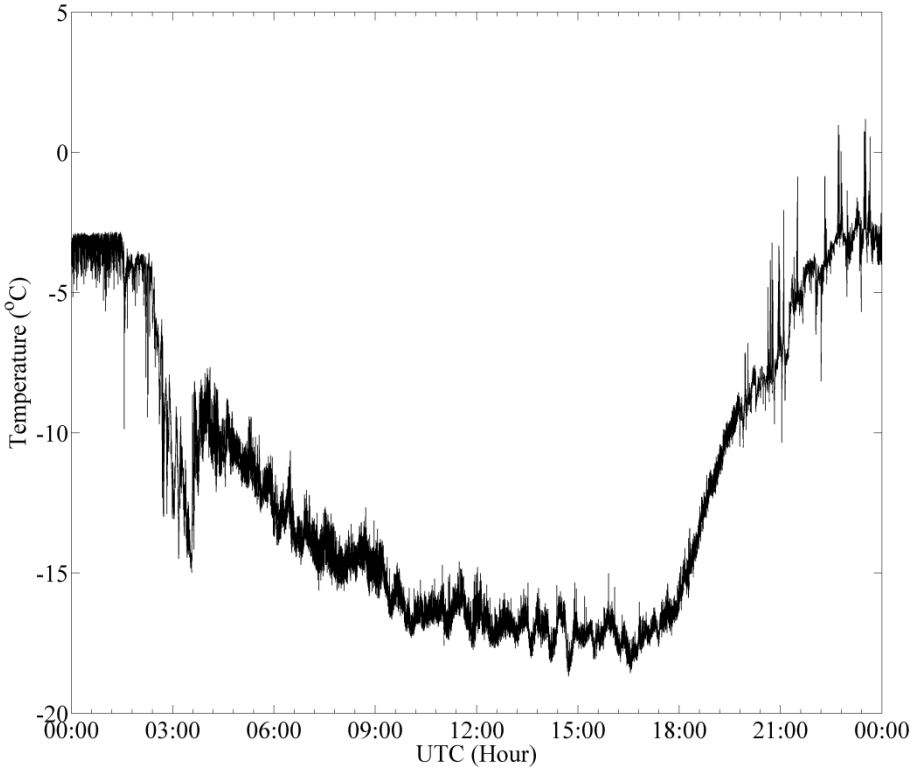

Figure 12a

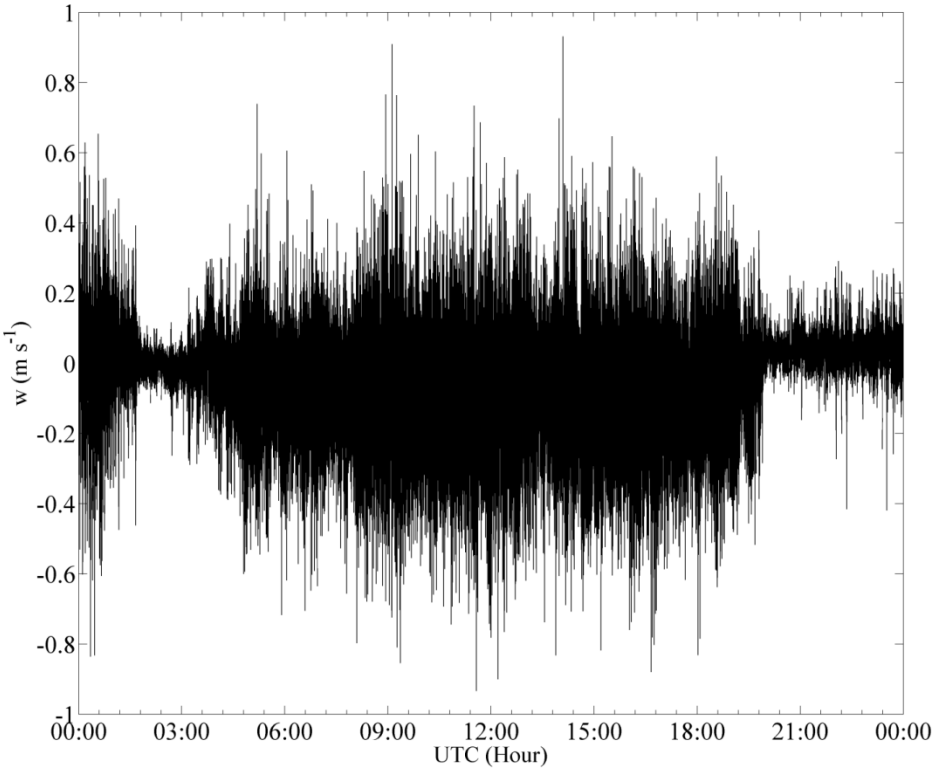

Figure 12b

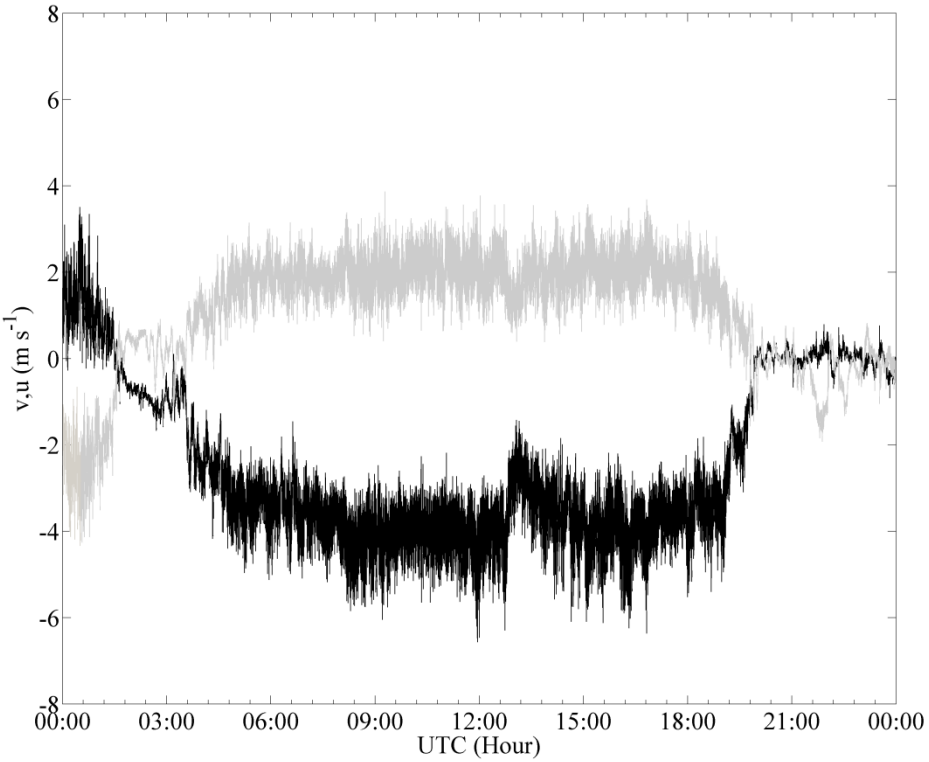

Figures 12 continued Figure 12c

Figure 13. Surface layer turbulent parameters for Case III at 4 m. Figure 13 (a) represents TKE, Figure 13 (b) represents friction velocity and Figure 13 (c) the surface shear stress.

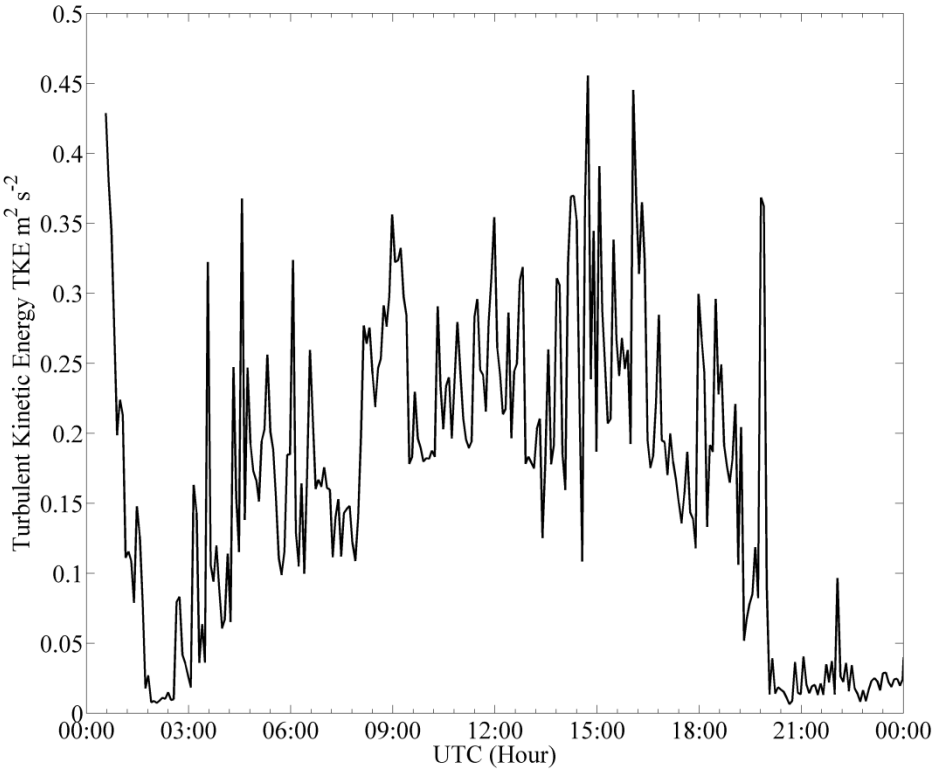

Figure 13a

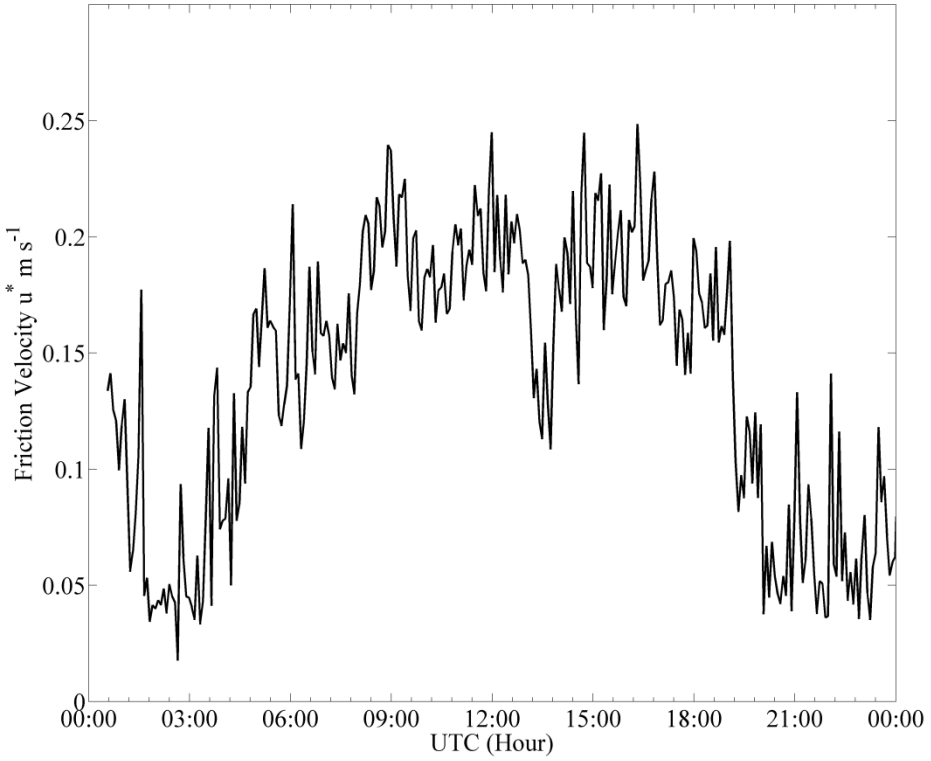

Figure 13b

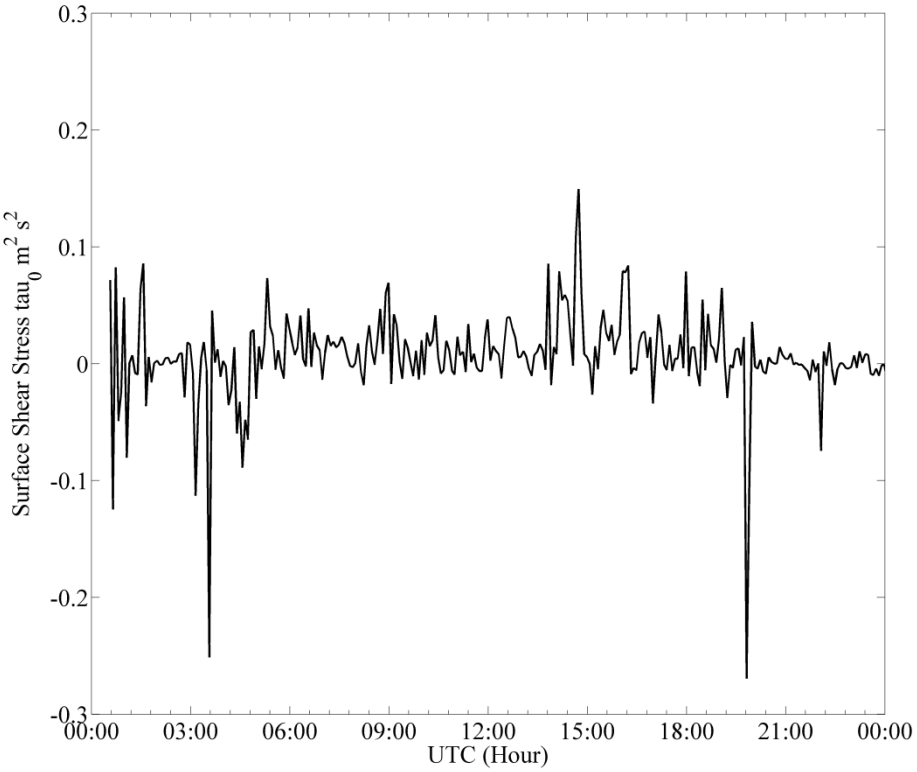

Figures 13 continued Figure 13c

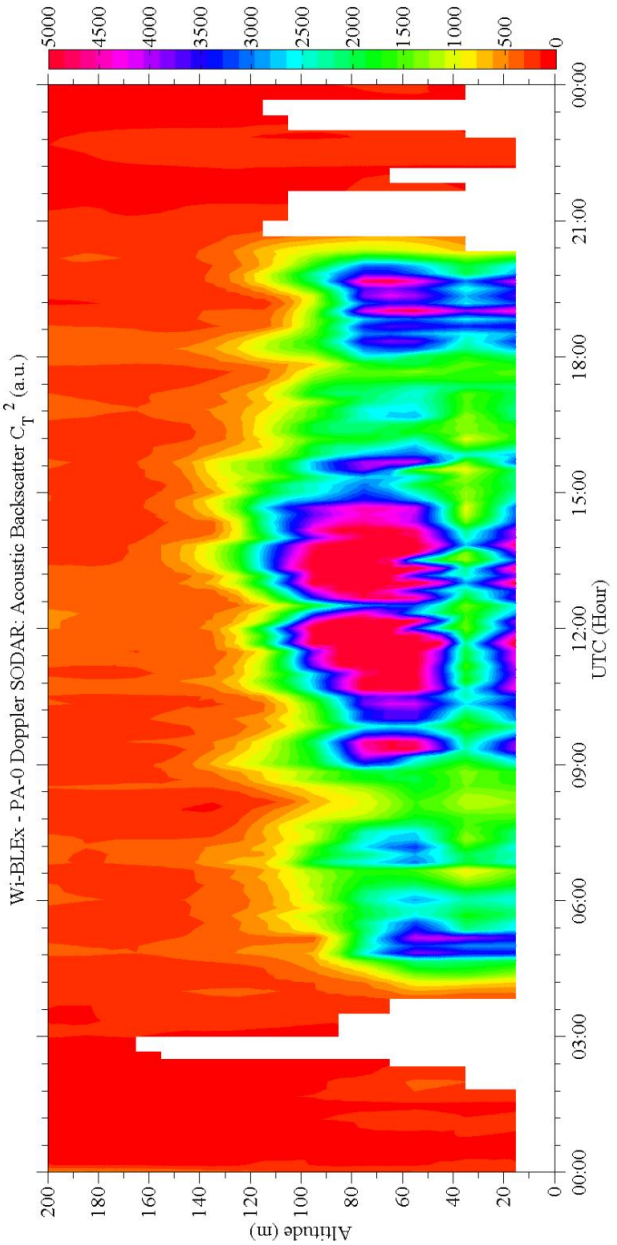

Figure 14. Vertical structure of the ABL from 6 March sodar represented by the thermal turbulent structure coefficient C_T^2 in arbitrary units with time resolution of 10 min and vertical resolution of 10 m.

Figure 15. Vertical Profiles of Case I **(a)** represents the vertical wind speed of the drainage flow episode during 18-19 January 2011. The first line represents the '-●-' in the wind speed profile (log C_T^2) in the **Figure 15 a (b)**, the second arrow represents the '-■-' the wind speed profile (log C_T^2) profile. **Figure 15 c** represents the vertical C_T^2 profile and **Figure 15 d** represent vertical wind speed profile.

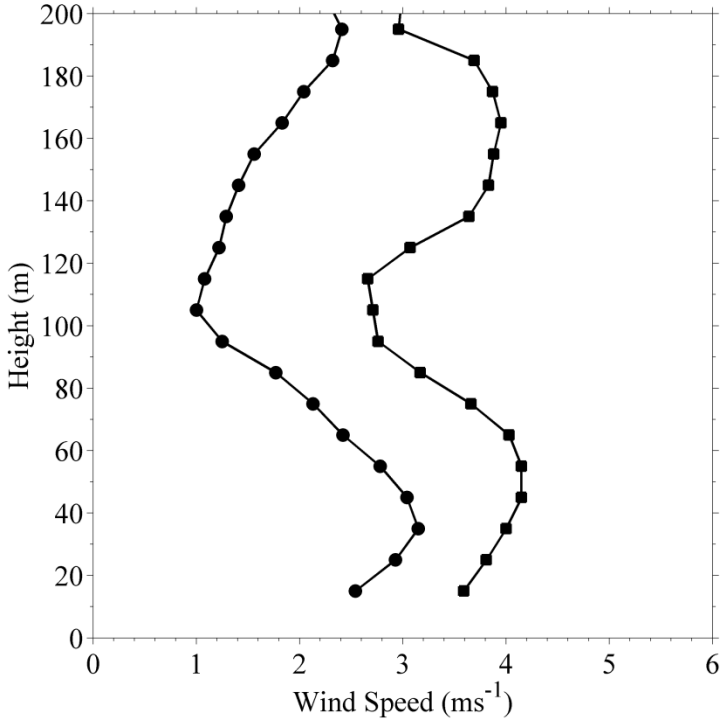

Figure 15a

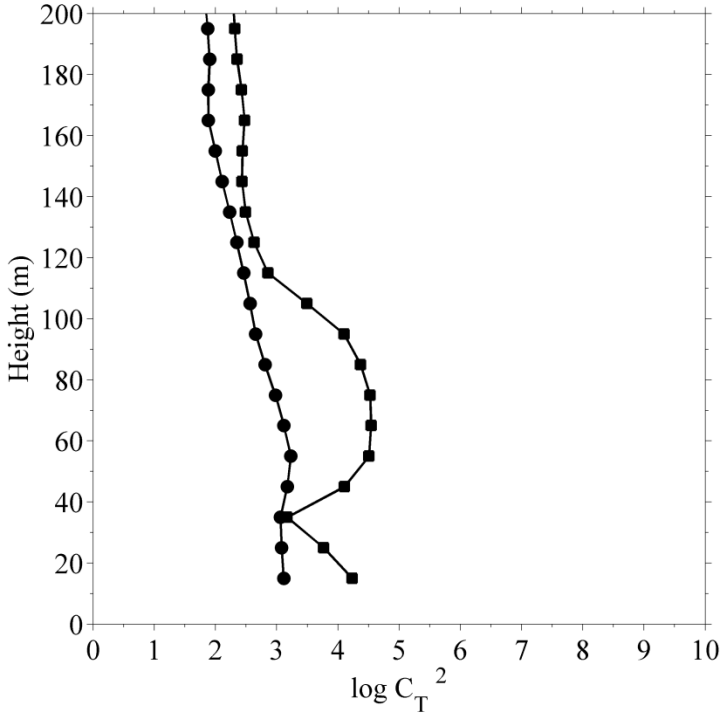

Figure 15b

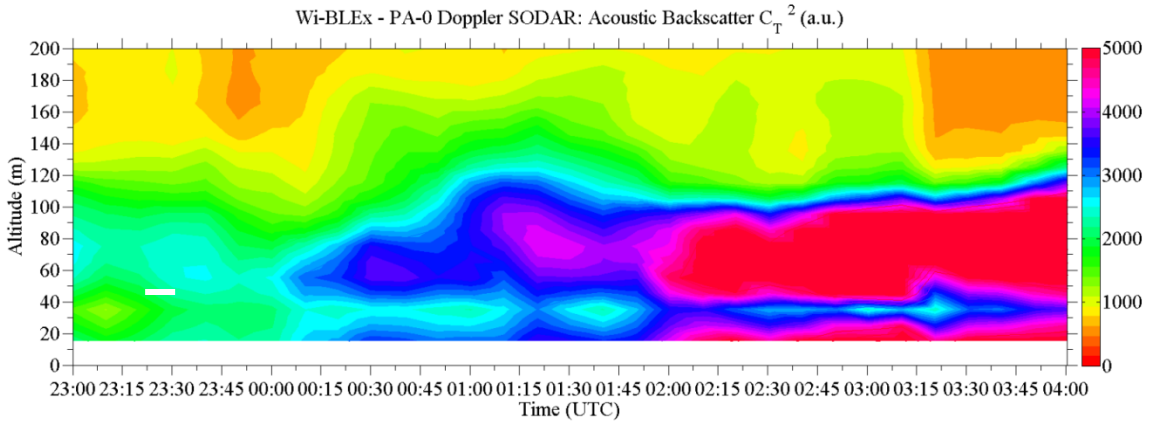

Figures 15 continued Figure 15c

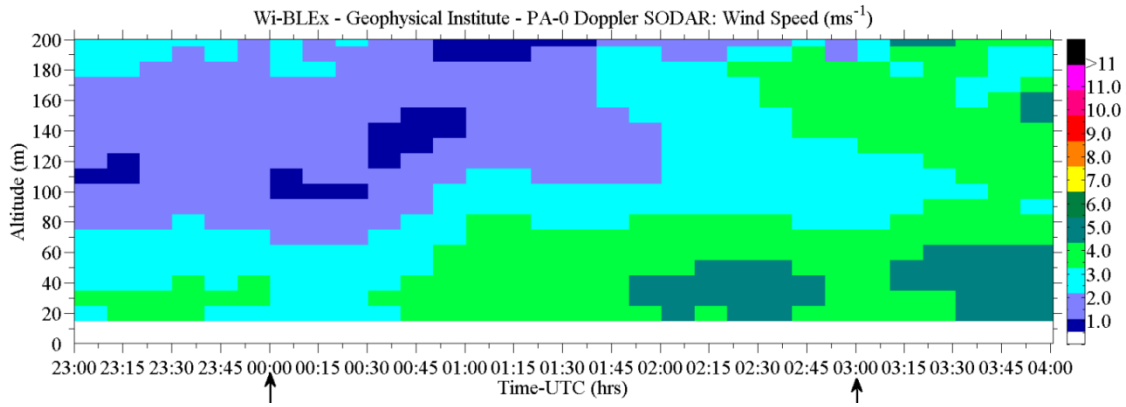

Figure 15d

Figure 16. Vertical Profiles of Case II **(a)** represents the vertical wind speed of the drainage flow episode during 7 February 2011. The first line represents the '-●-' in the wind speed profile (log C_T^2) in the **Figure 16 a (b)**, the second arrow represents the '-■-' the wind speed profile (log C_T^2) profile. **Figure 16 c** represents the vertical C_T^2 profile and **Figure 16 d** represent vertical wind speed profile.

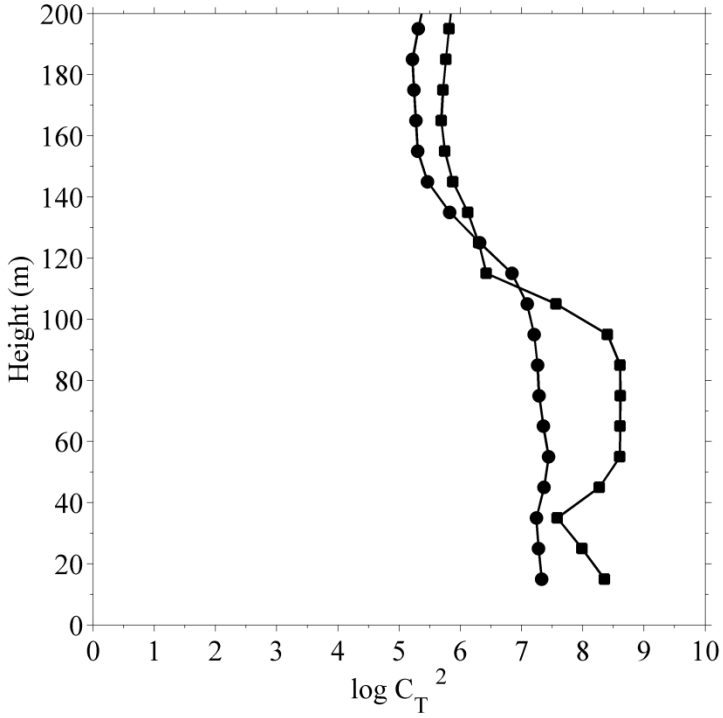

Figure 16a

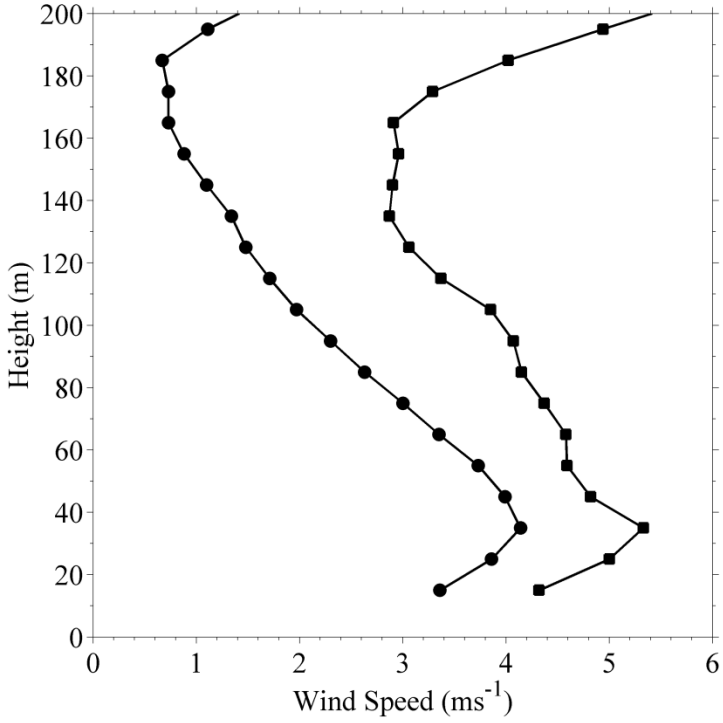

Figure 16b

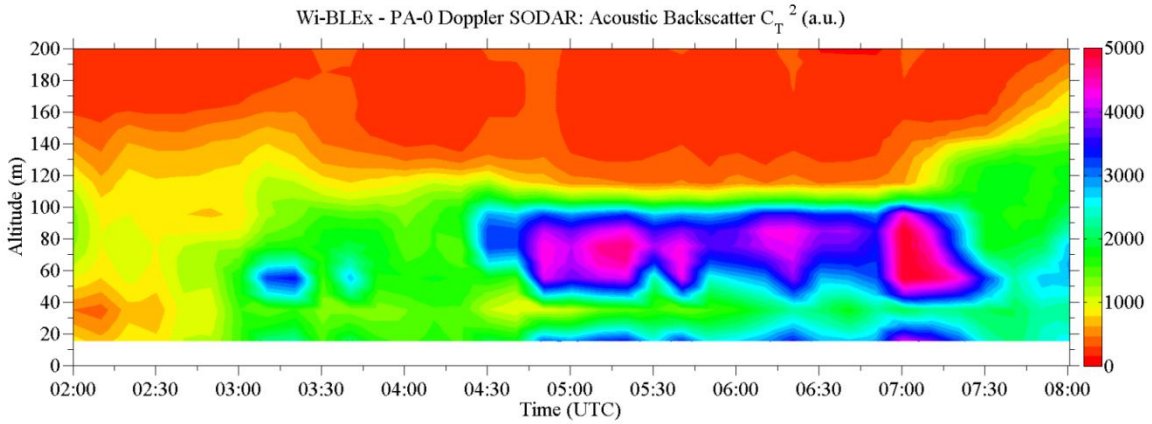

Figure 16 continued Figure 16c

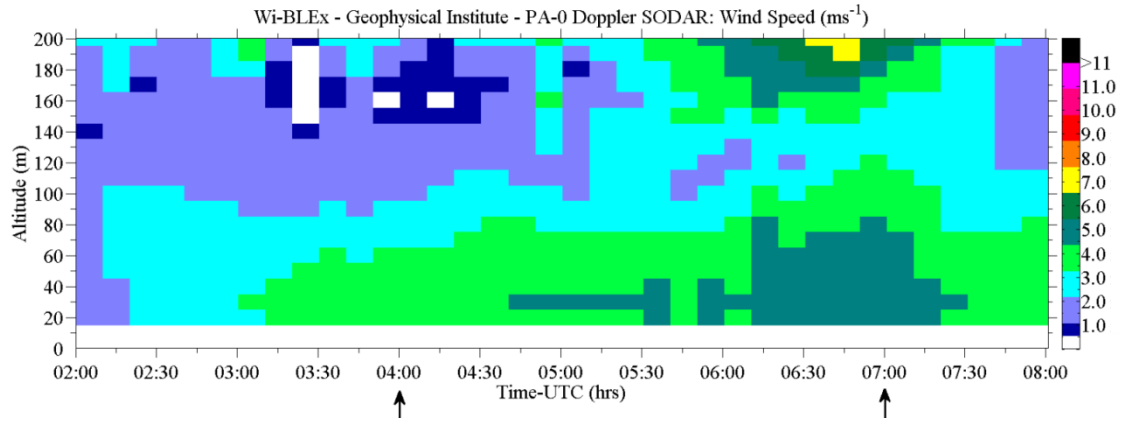

Figure 16d

Figure 17. Vertical Profiles of Case III **(a)** represents the vertical wind speed of the drainage flow episode during 6th March, 2011. The first line represents the '-●-' in the wind speed profile (log C_T^2) in the **Figure 17 a (b)**, the second arrow represents the '-■-' the wind speed profile (log C_T^2) profile. **Figure 17 c** represents the vertical C_T^2 profile and **Figure 17 d** represent vertical wind speed profile.

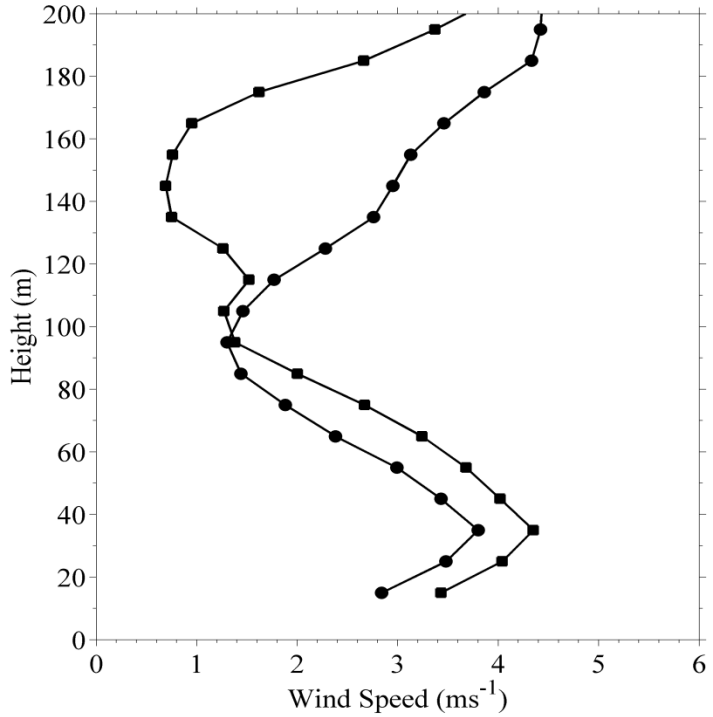

Figure 17a

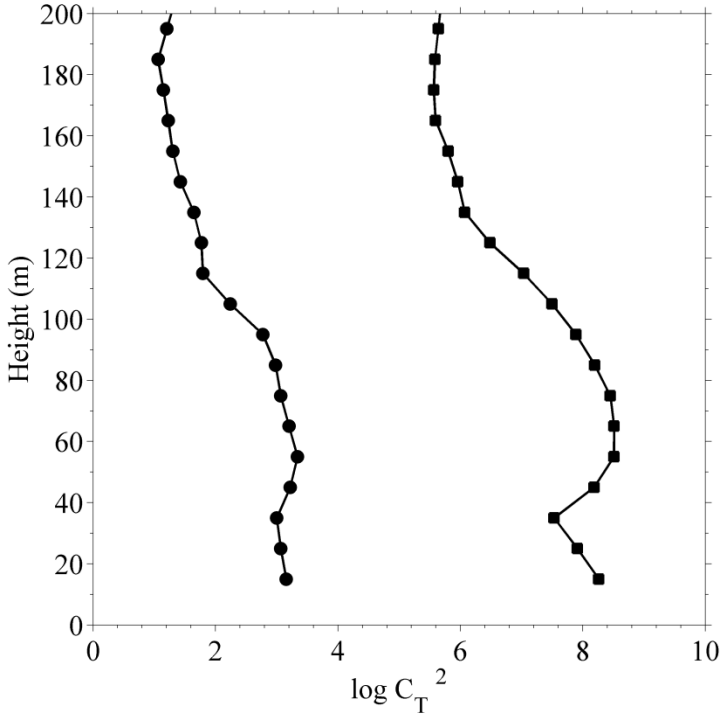

Figure 17b

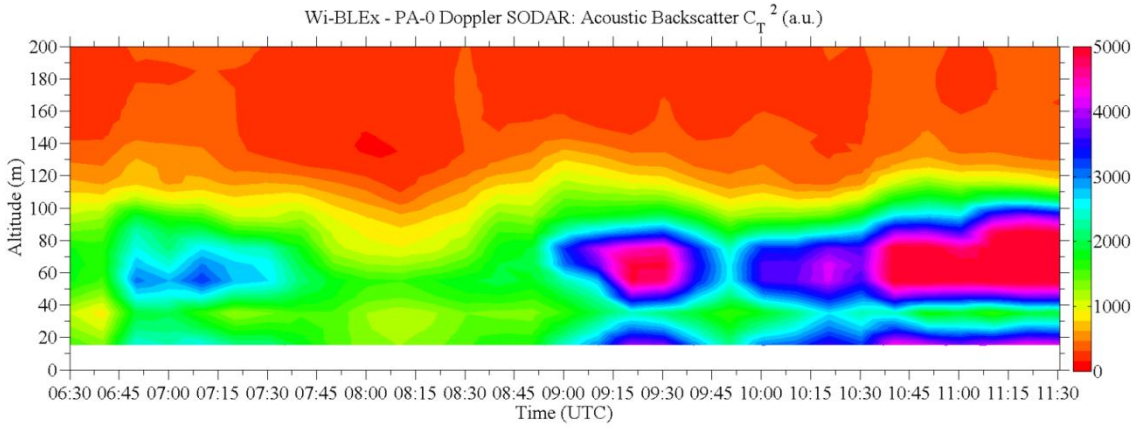

Figure 17 continued Figure 17 c

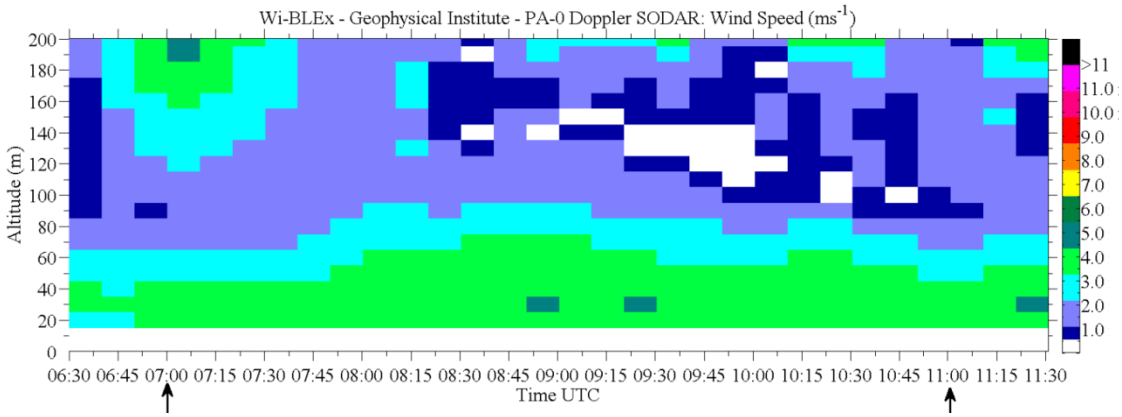

Figure 17 d

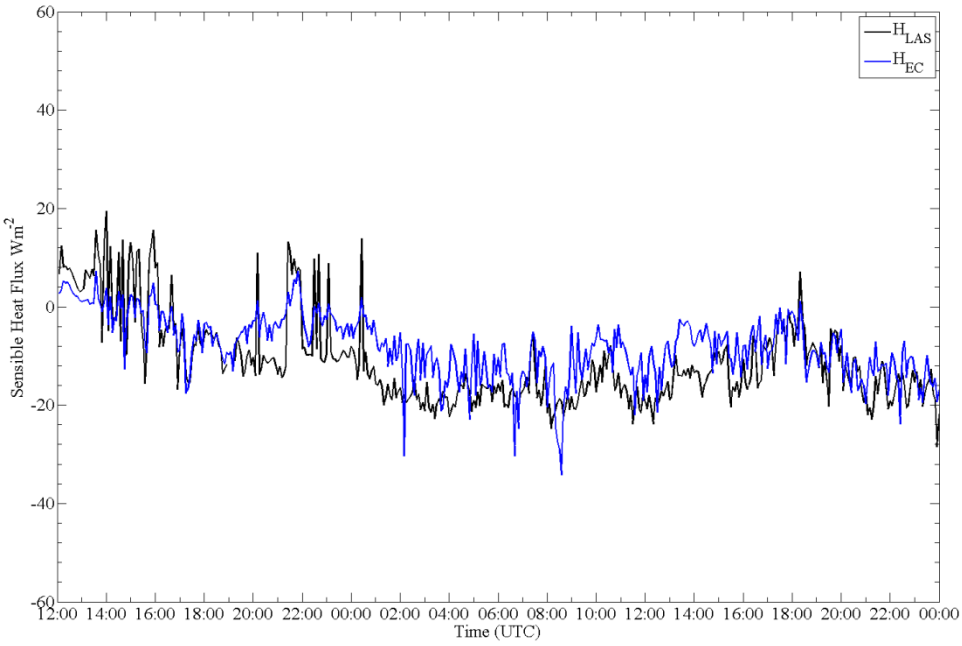

Figure 18. Sensible Heat Flux for Case I: In blue line calculated in 5 min intervals from the scintillometer (H_{LAS}) and the black dash line calculated in 5 min intervals from the sonics (H_{EC})

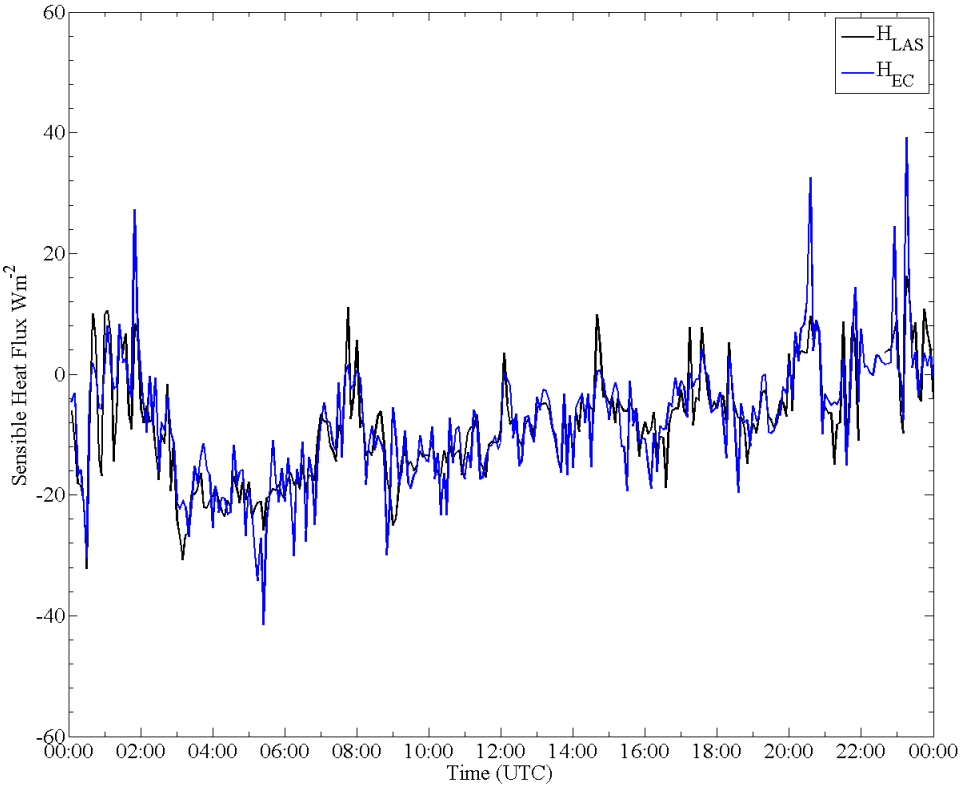

Figure 19. Sensible Heat Flux for Case II: In blue line calculated in 5 min intervals from the scintillometer (H_{LAS}) and the black dash line calculated in 5 min intervals from the sonics (H_{EC})

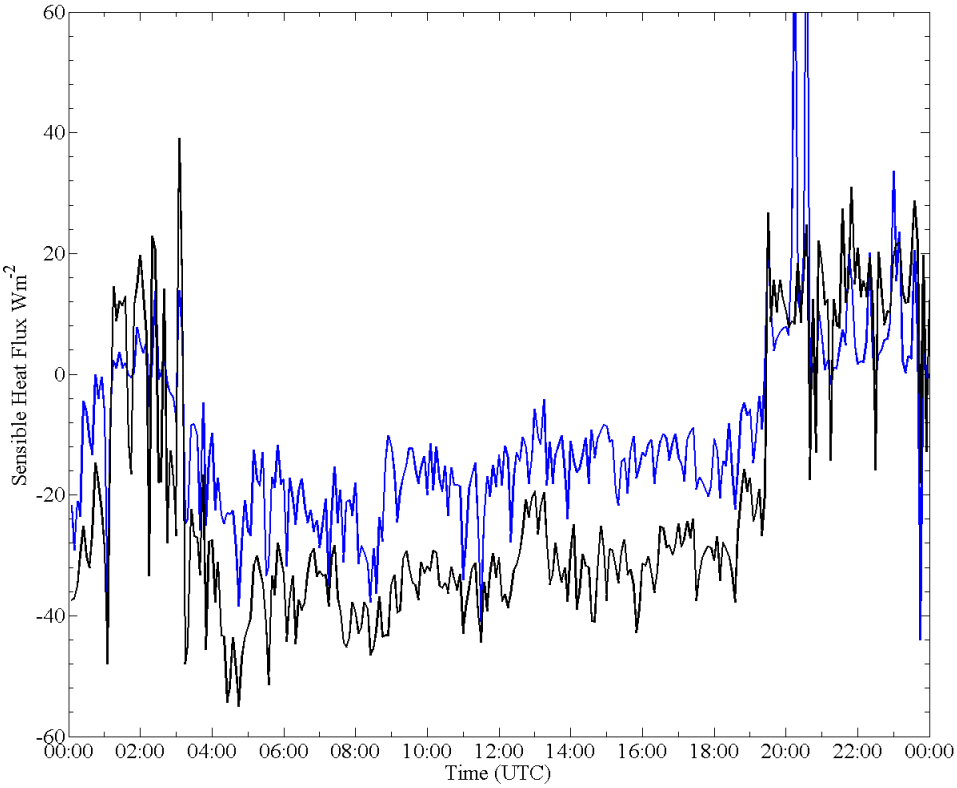

Figure 20. Sensible Heat Flux for Case III: In blue line calculated in 5 min intervals from the scintillometer (H_{LAS}) and the black dash line calculated in 5 min intervals from the sonics (H_{EC})

Chapter 4: The Layered Structure of the Winter Atmospheric Boundary Layer in the Interior of Alaska[1]

4.1 Abstract

The high-latitude winter boundary layer (BL) exhibits a constant, complex layered structure due to the extreme meteorological conditions in Alaska's interior. The occurrence of Elevated Inversion (EI), Surface-Based Inversion (SBI), and stratified layers in the sub-Arctic from January, 2000 to December, 2009 is reported. This analysis is based on radiosonde observation data from the Fairbanks National Weather Service station complemented by Winter Boundary Layer Experiment observations (2008-2011). This study found that SBIs occurred 64.02% of the time; an SBI was combined with one, two, three, or four simultaneous EIs 84.86%, 48.49%, 21.23%, and 7.99% of the time, respectively, in 3633 total cases. The calculated mean SBI height was 377.1 m; EIs occurred at 1230.8 m, 2125.0 m, 2719.8 m, and 3124.6 m. This analysis was able to discriminate between locally-controlled inversion layers and synoptic-dependent inversions, and to identify their formation mechanisms. It was found that in the presence of an SBI layer, 42.96 % of the first EI layers formed under anticyclonic conditions and 28.02% formed under warm advection situations. The remaining 29% of EI layers were identified as synoptic transients; less than 1% remained unclassified. These results lead to the hypothesis that the layered structure of the winter BL in combination with inversion

[1] Mayfield, J. and G.J. Fochesatto, 2011: The Layered Structure of the Winter Atmospheric Boundary Layer in the Interior of Alaska. *J. Appl. Meteorol. Clim. Submitted October, 2001. In Review.*

heights, temperature inversion strength, topography, and orientation of the Fairbanks area could represent a key ingredient in the air pollution promotion process.

4.2 Introduction

The absence of daylight combined with ice and snow-covered surfaces during the extreme winter in interior Alaska create a unique meteorological condition in the lower troposphere, where surface radiative cooling is one of the dominant forcing mechanisms enabling extremely stable boundary layer (BL) states to form, especially under clear skies in the severe low-temperature winter months from December to February. In these cases, and under low-pressure-gradient forces, the topographic configuration and mountain orientation in the Fairbanks area constrain the low-level tropospheric circulation. The air flow in the BL becomes locally quasi-laminar and regionally stagnant, and is dominated mainly by local-scale circulation and radiative cooling. This meteorological configuration can set up several days of strong, stable BLs; multiple stratified layers develop close to the surface, capped by a strong inversion layer known as a Surface-Based Inversion (SBI) (Wendler and Jayaweera, 1972; Wendler and Nipcon, 1974; Holmgren et al., 1975; Hartmann and Wendler, 2005).

During extreme high-latitude winters, in the absence of significant solar radiation, an SBI forms when a stagnant air flow makes contact with ice and snow-covered surfaces under non-advective, clear-sky conditions. In these cases, the air layers immediately above the surface cool by infrared (IR) radiation loss (Garrat and Brost, 1981; Andre and Mahrt, 1982). In the lowest layers of the atmosphere, this radiation transfer is manifested by a positive upward temperature gradient that extends to a height at which the surface

cooling effect vanishes and the air mass "recaptures" the negative environmental gradient. This point is termed the top of the SBI. Thus, the changes induced by this cooling process in the thermal structure of the BL (i.e., density discontinuities) promotes vertical divergence of the IR fluxes (Fuggle and Oke, 1976) and changes in the turbulent flux regime (Estournel et al., 1983; Guédalia et al., 1984; Estournel and Guédalia, 1985). The formation of the SBI at high latitudes was described earlier by Wexler (1936) and Billelo (1966) and follows strictly local conditions set at the synoptic scale (Bowling et al., 1968). This formation process has also been documented during captive balloon experiments in Fairbanks following surface energy-balance studies in connection with low-level clouds (Wendler and Jayaweera, 1972); it indirectly influences surface temperature via synoptic changes in the western Arctic (Stone, 1997) and is influenced by cloud cover (Shupe and Intrieri, 2004). The presence and role of the SBI has been documented during sub-Arctic snowmelt transition experiments (Wendler and Nicpon, 1974) which examined the surface energy balance, and by using acoustic sounding to probe the structure of the winter BL. This interpretation yielded detailed insights into instability layers, the formation and destruction of the inversion layers, and wave activity (Holmgren et al., 1975; Brown and Hall, 1978). On the other hand, climatological and long-term studies of the Arctic environment reveal a consistent SBI presence during winters in the North American Arctic (Maxwell, 1982; Bradley et al., 1992; Kahl et al., 1992), and in Eurasia (Serreze et al., 1992). More recently Hartmann and Wendler (2005) characterized the presence of the Fairbanks area SBI as being related to the wind direction. In their study, the inversion was present 75 % of the time when the wind

direction was from the northeast sector; when there was no inversion, 50 % of the time the winds were from the North, and 50 % of the time they were from the South. The presence of the SBI was evaluated across the Alaskan climatic regions and its time variability was linked to synoptic large-scale climatic fluctuations (Bourne et al., 2010). Similarly, recent studies covering Arctic and Antarctic stations by Zhang et al. (2011) evaluated SBI space-time variability and possible linkage to climatic fluctuations.

Depending upon the synoptic condition, the flow above the SBI may also develop inversion layers with respect to the flow in the BL; these layers are called elevated inversion (EI) layers. EI layers are discontinuities in air density that occur between the SBI and the free troposphere, mainly as a function of a specific synoptic flow condition. Three mechanisms are known to give rise to EI layers in the atmospheric BL flow: (1) "warm advective flows", either through topographically-elevated ridges over a stagnant, low-level BL flow (Byers and Starr, 1941; Busch et al., 1982; Milionis and Davies, 1992), or when warm air masses flow over large bodies of cold surface water (Csanady, 1974); (2) "subsidence inversion", under which EI layers form when an anticyclonic synoptic situation dominates the air flow, as described earlier by Reed and Kunkel (1960), Taylor and Yates (1967), and Busch et al. (1982), and during air pollution episodes as described by Katsoulis (1988 a, b), Prezerakos (1998), and Kallos et al. (1993). Under these conditions, the air motion in the BL is stagnant with little or no advection and is therefore prone to strong, continuous radiative cooling, causing stratification to develop in the vertical structure of the BL, while the upper levels above the BL are dominated by an anticyclone (Wexler, 1941; Bowling et al., 1968). This

stratification increases when the surface cools at a much higher rate than the air aloft. The emitted anthropogenic and biogenic gases and particulate matter are accumulated by the thermal inversions, contributing to "moderate" surface radiation loss by increasing divergence, while a downwelling long-wave IR component changes surface net radiation (Fuggle and Oke, 1976; Estournel et al., 1983; Guédalia et al., 1984); and (3) "residual layers" (Oke, 1978; Stull, 1988; Angevine et al., 2001), which are near-neutral layers containing aerosols and gases from the convective BL that developed on the previous day and exist between the nocturnal, stable BL and the free troposphere. The residual layers mostly form under non-advective and low-subsidence air flow conditions.

According to the aerodynamic concept of an atmospheric BL (Plate, 1971; Oke, 1978; Stull, 1988), the EI layers are not necessarily considered as part of the BL because their formation mechanism, occurrence, and origin are not related to surface processes. Nevertheless, it has been demonstrated through observational and numerical mesoscale modeling that these layers can effectively be coupled to the surface through different mechanisms, primarily including turbulent flows and radiative fluxes. Evidence of this dynamic coupling was documented by the initiation of convection close to the surface during the nocturnal-to-diurnal transition in the BL, a process that gives rise to intermittent turbulent mixing in elevated residual layers by vertical propagation of gravity waves generated at the top of the developing convective BL (Fochesatto et al., 2001 a, b). This interaction actually promotes downward mixing of pollutants and particulates from the elevated layers to the surface. This mechanism as has been demonstrated by the theoretical simulations of Robson (1983), by laboratory simulations (Willis and

Deardorff, 1978) during the nocturnal-to-diurnal transition (Angevine et al., 2001; Fochesatto et al., 2006), and through BL interaction with smoke plumes from forest fires (Pahlow et al., 2005). This study, however, concentrates on the layered structure of the BL during the winter, characterized by the occurrence of inversion layers that form by the first two mechanisms, giving origin to the "synoptically controlled" (EI) layers, which occur in winter at Arctic and sub-Arctic locations.

Fairbanks has been identified by the Environmental Protection Agency as a $PM_{2.5}$ non-attainment area due to regular occurrences of severe wintertime $PM_{2.5}$ pollution episodes. In this context the occurrence of an EI can initiate two mechanisms of potential importance to the Fairbanks air pollution problem. One mechanism is the upper-level capping inversion imposed by the EIs. The strength of this temperature inversion is not as large as that of the SBI, but it is strong enough to effectively cap elevated plume stack emissions from power plants that were able to penetrate the SBI or whose emissions were above the current SBI height. The second mechanism is the possible initiation of mixing in the BL through decreasing inversion strength in the SBI driven by increasing IR flux divergence and the accumulation of IR-absorbing gases and particulate matter in the presence of the EI layers.

This article is organized as follows: section 2 describes the data and methodology used to analyze the observations and to detect inversion levels and stratified layers; section 3 presents the statistical analysis of a temporal series of inversion layers over the selected period (2000-2009); section 4 presents the analysis of locally-controlled inversions and stratified levels; section 5 presents the analysis of synoptically-controlled

EI layers; and section 6 presents a discussion of the described mechanisms and provides supporting observational evidence for persistent low-level SBI inversions. A discussion of the potential for air pollution when EI layers develop in the presence of an SBI is provided by thermodynamics and acoustic remote-sensing profiling during a warm advection.

4.3 Data and Methodology

This study is based on observational radiosonde data archives for the period January, 2000 to December, 2009 from the National Oceanic and Atmospheric Administration's (NOAA's) Earth System Research Laboratory (ESRL) Radiosonde Archive obtained at the Fairbanks International Airport (International Civil Aviation Organization (ICAO) station code PAFA 70261). The data consist of 00 and 12 UTC radiosondes launched twice daily. The data acquired are quality controlled at the station and include observations of pressure, temperature, dew point, wind direction, and wind speed (Schwartz and Govett, 1992). The data is subject to quality-assurance algorithms, including checks for format problems, physically implausible values, climatological outliers, and temporal and spatial temperature inconsistencies. Nevertheless, in order to provide consistency in the analysis performed here, an additional data-screening procedure was elaborated to include only the 00 and 12 UTC radiosonde cases and profiles with more than three points below 700 hPa. Additionally, a control check was performed to ensure that a minimum number of data points per pressure level existed to justify identifying the presence of inversions or stratified levels in each analyzed radiosonde profile. Table I presents the mean and standard deviation of the number of

points in the radiosonde data base as a function of the significant pressure-level thickness. The data processed for this study include data from 2000-to-2009, covering only the winter period from October to March of each year. A total of 3633 profiles were obtained; 2326 profiles falling within the mentioned restrictions were selected for use in this study. Moreover, since the sampling rate of the radiosondes is not constant with height, the number of points per 100 m increment was calculated to indicate how well each atmospheric level was represented (Table 4.1).

An inversion level is a height in the atmosphere where the temperature gradient changes from being positive upward to negative upward; therefore, several algorithms can be created to numerically process the temperature profile and determine the height of the inversion. For instance, Kahl (1990) developed an identification algorithm to detect the inversion level by scanning each profile starting from the surface, using specific constraints to assign the inversion levels for a number of stations in the Arctic. The same algorithm was used more recently by Kankanala (2007) to determine the height of the stable BL during the 2005-2006 winter in Fairbanks, while Zhang et al. (2011) used this algorithm in a climatological analysis over pan-Arctic and Antarctic meteorological stations. On the other hand, Serreze et al. (1992) developed a mathematical fitting process with a specific constraint to determine the height of the SBI for similar climatological purposes. Serreze's algorithm was used recently by Bourne et al. (2010) to determine the temporal SBI series across Alaska and to study the large-scale synoptic coupling related to climate changes. However, temperature profiles in the interior of Alaska exhibit several complex slope changes, indicating the combined presence of stratified,

isothermal, and inversion layers, in particular close to the ground. These layers, when observed with the exclusive view of the radiosonde profile, may present gradients often classified as non-relevant because it is argued that they might be overridden by the eventual intra-day variation (Kahl, 1990; Serreze et al., 1992). However, it has been demonstrated in a recent focused high-resolution radiosonde experiment combined with Doppler sodar measurements during the Winter Boundary Layer Experiment (WiBLEx, 2009/2010) conducted at the Fairbanks International Airport National Weather Service (NWS) station (Malingowski**,** 2010) that these inversions and stratified levels are significant and, more importantly, are constantly present when favorable environmental conditions exist.

Therefore, a numerical procedure was developed to account for stratified and inversion layers and those layers embedded in between (e.g., isothermals). In this case, the temperature profile was assimilated into a poly-line mathematical structure of minimal length, obtained based on an iterative numerical routine. The numerical routine minimizes the following error expression:

$$\varepsilon = \|T(z) - \sum_k m_k.z + b_k\| \quad (1)$$

where T(z) is the original temperature profile and the parameters m_k and b_k are retrieved by polynomial fitting. The convergence is controlled by the error fraction, calculated as the largest singular value of ε, that reproduces inversions and stratified layers with an error difference of less than 1 % and a gradient threshold larger than 0.1 ^{o}C / 100 m to detect stratified or inversion layers at any level.

The numerical sequence starts by creating a vertical profile that connects the first point of the temperature profile near the ground with the last point at 500 hPa and increases the number of points in the fitting of the poly-line structure downward according to the temperature gradient variation within the prescribed mathematical error (Eq. 1), keeping the number of points in the fitted profile to a minimum. Once the significant points of the profile have been retained, determining the inversion and the significant stratified levels follows the procedure of detecting the changes in the signs of the slopes (m_k) in the thermal gradient to deduce the heights at which those changes are verified. This process assigns an "inversion level" to points where a change in the sign of the thermal gradient is verified and "stratified levels" to heights where changes in the thermal gradient are verified, but the sign is preserved according to the following scheme: stratified layers ($m_k \leq 10$ ^{o}C/100 m) and strongly-stratified layers ($m_k > 10$ ^{o}C/100 m). Once a layer is detected, the numerical procedure collects the heights of the inversion layer top and base, the top and bottom temperature (inversion strength), the pressure level, and the dew-point temperature.

Figure 1 illustrates two temperature profile cases and the application of the detection layer algorithm. Inversion (INV) and stratified (S) levels, negative slope layers (N), and isothermal layers (I) are indicated in the rightmost column of Table 2, labeled "Class". In order to ensure consistency between the thermodynamic profile and the retrieved data the method's performance was verified by randomly selecting several cases across the data base. Table 2 indicates the heights of inversions and stratified levels detected by the algorithm in the temperature profile examples.

4.4 Temporal Series of Inversion Layers

Applying the methodology explained in section 2 to the NOAA-ESRL Radiosonde Archive data base for the period January 2000 to December 2009 retrieved the points where a change in the slope is verified with 1 % (0.1 ^{o}C/100 m) of prescribed fitting error. This resulted in a temporal series indicating the presence of multiple inversion levels located, on average, below the standard pressure level of 500 hPa. A test for randomness was performed on each temporal series. The test was applied over sub-ensembles of the temporal series made of 50 data samples, each equivalent to approximately 20 days of data, with random time lag changes to confirm the test results. It was found that the null hypothesis "sequence is random" cannot be rejected at the 5% significance level with probabilities above 50% in all the cases (Wilks, 2006). Similarly, the data series was tested to determine whether the data were normally distributed. The Kolmogorov-Smirnov test (Lilliefords, 1967) was performed over the temporal series and resulted in rejecting the null hypothesis “data comes from a standard normal distribution” at 5% significance. Therefore, the statistical parameters that characterize the temporal series were calculated by using empirical cumulative probability density functions (CPDFs) combined with a tail distribution estimation based on the general Pareto power law (Beirlant et al., 2005) for the lower and upper limits of the data density distribution on each temporal series. Table 3 summarizes the statistical parameters as well as the number of cases found in each temporal series of the retrieved inversion heights. INV-1 is the first inversion detected in the profile, with its base on the surface; INV-2 to INV-5 represent inversions that are present at increasing heights.

Based on these preliminary statistical indicators, the three first inversion layers are retained as the most important in terms of BL exchanges and air pollution dispersion and transport. Figure 2 shows the temporal series of the retrieved inversion heights by years and the histograms of height distributions and the corresponding CPDFs in Figure 3. For each inversion height the depth of the inversion layer (ΔZ), the temperature across the inversion (ΔT), and the temperature gradient (slope, m_k) were determined. Table 4 summarizes the main statistical parameters by inversion series.

Based on the values presented in Table 4, there is a clear distinction between the statistical parameters that characterize INV-1 and those that characterize INV-2 and INV-3 in depth, inversion strength, and stratification. Therefore INV-1 depth ΔZ is the height of the SBI, while INV-2 and INV-3 are indicated here as EI layers.

Of particular interest, INV-1 is present 64.02% of the time while the two EIs, INV-2 and INV-3, are present 54.34% and 31.05% of the time, respectively. Fairbanks is located on the valley floor of the Chena and Tanana river basins; it is sheltered by nearby hills that rise to an elevation of 300-500 m on the northwest, north, and northeast of town, with the foothills of the Alaska Range forming another barrier to the south at ~50 km distance. When the average height of inversion layers, shown in Table 3, is placed in the context of Fairbanks topography, this data indicates that INV-1 (SBI) is mainly "locally controlled" or, more precisely, controlled by local flows and surface processes, while INV-2 and INV-3, the first and second EI layers, are mainly "synoptically controlled".

This finding allows a hypothesis to be constructed, based on the local character and extreme conditions of the winters in interior Alaska, that INV-1 could also develop

stratified and multiply-stratified layers closer to the ground due to the strong radiative cooling rate and the injection of IR-absorbing gases and particulate matter into the atmosphere from anthropogenic emission sources during winter. In addition, because the EIs exist at very low heights, their presence in the Tanana Valley air-shed could play a significant role in the air pollution process. This complexity in the inversion layering is illustrated by an apparent discrepancy in the statistical mean of the inversion layer stratification shown in Table 4. When the ratio of the strength of the temperature inversion ΔT to the depth of the inversion ΔZ is compared to the mean layer stratification m_k for INV-1 (SBI), this ratio ($\Delta T/ \Delta Z$) will converge to the m_k slope only when the inversion layer is always or mostly composed of a single stratified layer, and will differ when this inversion is composed of multiple stratified layers (See Figure 4, 5 and 6).

4.5 Locally-Controlled Inversions

In this section, the characteristics of INV-1 (SBI) and the occurrence of stratification levels within INV-1 are analyzed. The SBI is particularly present in the high latitudes during winter, under clear skies, over snow and ice covered surfaces, and under low-wind conditions. In these cases, the long-wave radiative flux dominates the surface energy balance over turbulent fluxes and advection terms. This radiative equilibrium is fragile and can be disrupted by either the presence of low-level clouds (Wendler and Jayaweera, 1972; Jayaweera et al., 1975) or the development of surface winds (Wendler and Nipcon, 1974), which destroy the stratification. The lowest minimum surface temperature is reached when the SBI becomes decoupled from the rest of the atmosphere. This inversion level is regulated by a number of factors, including local flows, quasi-total

absence of shear-stress turbulence in the surface layer, energy balance equilibrium between surface net radiation and atmospheric downwelling IR, and, most importantly, the presence of anthropogenic-emitted gases and particulate matter that accumulate in the SBI layer.

The SBI and its influence on the thermodynamic characteristics of the atmospheric surface layer is important in regulating turbulent flux regimes in high-latitude ecosystems, and therefore the SBI affects the surface energy balance (Cohen et al., 2007; Huff et al., 2010; Chen et al., 2011), regulating the dynamic exchange mechanisms for dispersion of pollutants and contaminants. Accurately representing the SBI in simulation models is central to describing air pollution in the urban arctic atmosphere (Moelders and Kramm, 2010), because the SBI influences the thermodynamic exchange at the surface interface by imposing boundary conditions on the sub-soil temperatures and consequently altering the state of the permafrost active layer (Romanovsky and Osterkamp, 2000).

The thermodynamic profile that describes the SBI layer can develop an important complexity when stratified layers form. These layers are common features during the winter in interior Alaska and very effectively accumulate pollutants in urbanized areas. The development of SBI layering and the strengthening of the SBI vertical gradient can also cause mixing to occur, specifically downward mixing at its upper interface. (See details in Fernando et al. (1994) of laboratory experiments investigating mixing in stratified layers). Therefore, the thermal gradient in the SBI can be imagined to be composed either of a single stratified layer or of a number of layers, or even to include

isothermal layers. Billelo (1966) sketched these possibilities; they are not repeated here for simplicity.

This study analyzed 3633 radiosonde cases from January 2000 to December 2009, taking into account measurements from October to March of each year and two radiosondes per day at 00 and 12 UTC. From the entire data base, a total of 2326 cases showed the presence of an SBI, indicating that an SBI occurs 64.02% of the time. In the remaining data the inversion was not present, or the pressure height exceeded 500 hPa, or the surface layer was neutral, which occurred mainly when ice or water fog was present (Benson 1965; Bowling et al., 1968). Based on the analysis of the radiosonde data base the SBI presence was screened to determine the characteristics and the statistical occurrence over time of stratification. Stratification was classified as either stratified layers (10 ^{o}C /100 m) or strongly-stratified layers (> 10 ^{o}C /100 m). Figure 4 and Figure 5 presents the temporal series of stratified layer heights, indicating the height where the maximum thermal gradient within the SBI was verified. The statistical parameters are indicated in Table 5.

Of the cases that indicate the presence of SBI layers, 1404 were classified as being formed of stratified layers and 363 of strongly-stratified layers according to the criteria indicated in this section. The remaining cases were composed of a single layer at the limit of algorithm detection, which is 1% (0.1 ^{o}C/ 100 m) for thermal gradient variation. Therefore, 60.36% of SBI cases are composed of a stratified layer while 15.60% are composed of strongly-stratified layers. Moreover, a distinctive pattern is observed in the mean height at which the maximum stratification is attained; strongly-

stratified layers occur at a low height of ~50.2 m, while the 113.6 m height of stratified layers is consistent with the local character of this inversion. These heights are significantly lower than the mean statistical height of the SBI inversion layer; the strongly-stratified layer is about $1/8^{th}$ and the stratified layer about $1/3^{rd}$ of the mean inversion height of 377.1 m. Despite the variability of these two modes, with standard deviation = 112.6 m and maximum = 918 m for stratified layers and standard deviation = 30.3 m and maximum = 270 m for strongly stratified layers, the level of the stratified layer is still below the maximum height of the topography as described before, reinforcing the idea of locally-driven inversion and stratified layering. This in turn imposes a severe restriction on the dispersion and transport of pollutants and particulate matter and creates an important complexity in simulation models, in particular when models attempt to characterize the local character of these stratified inversion layers at extremely low surface wind speeds.

4.6 Synoptically-Controlled Inversions

Synoptically-controlled inversions were identified in section 3 as the temporal series INV-2 and INV-3. These inversions are detected in the free troposphere above the SBI. Because these inversions occur above the first inversion INV-1 and above the ridges defining the topography surrounding the Fairbanks area, they are classified as EIs. In the interior of Alaska, EIs exhibit a multiply-layered structure and thermodynamic properties that differ depending upon the synoptic condition. The non-local air mass capped by the EIs is often a near-neutral slightly-stratified warm air layer, warmer than the air mass

capped by the SBI close to the surface. Therefore, the EIs represent an important feature of radiative flux exchanges over the frigid and stagnant SBI.

As mentioned in the introduction, the dynamic processes lead rise to the presence of EIs in interior Alaska during winter can initially be partitioned into two types: Anticyclonic (AC) and Warm Air Advection (WAA). These two fairly frequent synoptic configurations that dominate interior Alaska in winter occur via a combination of large-scale ocean-land-atmosphere interactions (Petterssen et al., 1956; Curry 1983, 1987). In particular, during the winter in the Arctic region an anticyclone is generated when cold air over the continent produces synoptic-scale high pressure, mainly over the two vast land masses that surround the Arctic, Siberia and North America. On the other hand, warm and moist air over the ocean produces synoptic-scale low pressure localized most of the time in the Aleutian Islands and the Gulf of Alaska. The cyclogenetic combination of low-pressure conditions over the Northern Pacific and jet stream movement from east to west provides storm activity for interior Alaska. The boundary between these climatological synoptic patterns is the Arctic Front. The weather in interior Alaska is determined by the movement of the Arctic Front (Willis and Grice, 1976), which defines the boundary separating the cold and dry continental Arctic air mass from the warm and moist marine air. These synoptic pathways have been recently reviewed by Cassano et al. (2011), who describe the effect of a large-scale synoptic pattern on surface temperature in Alaska. The space-time evolution of Siberian and Canadian surface high-pressure systems enables the advection of warm moist air from the Alaskan coast, allowing this air to penetrate northward in the form of a cyclonic advection into interior Alaska. The

advection acts as a dynamic process; when it reaches interior Alaska, it produces a thermodynamic contrast with the low-lying denser air mass that has been cooled by radiative effects from the ground. These thermodynamic differences lead to, at the meso-local scale the occurrence of an EI also known as a "frontal inversion". Conversely, when the Siberian and Canadian high-pressure systems are strong, a regional synoptic subsidence takes place, causing the air to sink and warm adiabatically, and forms an EI also known as a "subsidence inversion". In the first case, the cyclonic advection moves the air mass and forms the WAA EI; in the second case, the meteorological feature imposes, at a regional scale, a dynamic subsiding motion resulting in a thermodynamic response in the lower tropospheric levels and forming the AC EI. The detection of EI heights and the determination of their characteristic depths and strengths followed the criteria defined in section 3. The statistical parameters are described in Table 4.

Here, however, we address the problem of the eventual difference in properties that exists between an EI originated through a WAA and an EI originated through an AC synoptic driver (Mayfield and Fochesatto, 2010). To address this problem, the EI layers were identified based on the dew-point depression between the top and the base of the first and second EI layers following the procedure developed by Milionis and Davies (1992). Therefore, in the cases where an EI layer was detected, the dew-point identification was evaluated following the criteria indicated in Equation 2:

$$DT_d = T_{d\,Top} - T_{d\,Base} \begin{cases} WAA \rightarrow DT_d > 0 \\ AC \rightarrow DT_d < 0 \\ undefined\ DT_d = 0 \end{cases} \quad (2)$$

Based on this criterion, the EI-1 and EI-2 temporal series were flagged with this condition and four new temporal series of EI layers were created. The first is the series of EI layer heights formed by AC conditions in both EIs, while the second verifies that two EI layers formed after the WAA had occurred. The third and fourth series were generated based on "synoptic transients" characterized by a combination of AC and WAA effects on either EI-1 or EI-2. Figure 7 shows the histogram and CPDFs for the EI-1 and EI-2 (AC) series while Figure 8 displays the same plots for the EI-1 and EI-2 (WAA) series. Figure 10 and 11 shows the histograms and CPDFs for the cases representing synoptic transient combinations. Table 6 summarizes the statistical parameters that characterize the thermodynamic structure of EI layers as well as the differences between them based upon their synoptic driver, i.e., WAA, AC, and synoptic transients (Bodurtha, 1952).

A significant difference was discovered between mean EI heights depending upon synoptic configurations. From Table 6, the mean inversion height of EI-1 (WAA) was 245.4 m below the mean inversion height for EI-1 (AC). In addition, the difference in the 90^{th}-percentile tail interval exceeds 866.9 m. The same behavior is observed when comparing the mean heights of EI-2 WAA and AC cases, and their difference rises to 512.4 m over 2000-2009. Comparing the difference between the mean inversion heights in transient cases against the AC or WAA cases revealed that the mean height of EI-1 (AC-transients) was 315 m lower than the EI-1 (AC) cases and 933 m lower in the 90^{th}-percentile. Similarly, the mean height of EI-1 (WAA-transients) was 247.8 m below that of EI-1 (WAA). These differences observed at the EI-1 level are not reflected equally at the EI-2 level. For example, no appreciable difference was found between AC cases and

AC-transients, while WAA-transients were found to be 140.3 m higher than the average height of WAA cases at the EI-2 level. The density distribution of data was wider in the AC cases than in the WAA cases. This difference is larger at the EI-1 level than at the EI-2 level. Specifically, the 10^{th}- to 90^{th}-percentile interval for EI-1 (AC) was 2246.2 m, while for EI-1 (WAA) it was 1452.3 m. The same interval for EI-2 (AC) was 2949.6 m and for EI-2 (WAA) it was 2620 m. In terms of inversion depths, all EI layers exhibit a mean depth in the range of 200-300 m, while the 10^{th}- to 90^{th}-percentile yields a range of ~ 100-600 m. The average temperature gradient of all EI layers was found to range from ~ 0.8 to 1.5 ^{o}C / 100 m with a 10^{th}- to 90^{th}-percentile range from 0.13 to 2.9 ^{o}C / 100 m.

In the case of the mean dew-point temperature gradient, the occurrence of transients skews the distribution of EI cases differently. For example, the dew point value for EI-1 (WAA) is smaller during a WAA transient, while the opposite occurs for EI-1 (AC). Conversely, at the EI-2 level, the transients skew the density distribution in the opposite direction; the dew point value for EI-2 (WAA) moves to the right when a WAA transient occurs, and to the left for the EI-2 (AC) condition.

4.7 Discussion and Summary

The layered structure of the winter BL in interior Alaska presents two important inversion characteristics: low-level locally-controlled SBI and upper-level synoptically-controlled EI layers. The mean SBI heights are particularly low compared with SBI levels in the Arctic that were documented by Kahl (1990), Kahl et al. (1992), and Serreze et al. (1992), or evaluated at different locations in Alaska (Bourne et al., 2010) and in the pan-Arctic and Antarctic (Zhang et al., 2011). One reason that can explain these differences is

Fairbanks' location and topographic configuration, including its distance from the ocean and the sheltering effect of the mountains to the south and north. These topographic features create the necessary conditions for one of the strongest BLs on Earth to occur (Benson 1965; Bowling et al., 1968; Wendler and Nipcon, 1974); these conditions are comparable to Antarctic conditions (Dalrymple, 1966; Hudson and Brandt, 2005).

In terms of the radiosonde analysis method described in section 2, the temporal SBI series are not restricted to defining an inversion layer only when the depth of the cold layer is 100 m or deeper as in Kahl (1990) and Kahl et al. (1992); the SBI series are not even defined through a fitting process (Serreze et al., 1992) that overrides, in some cases, the air mass in the first layers, depending on the radiosonde resolution and the air-mass thickness. On the other hand, these methodologies seem designed to be more sensitive to retrieving inversion heights when studying the effects of large-scale circulation on the BL (Bourne et al., 2010; Zhang et al., 2011). Nevertheless, in order to assess the reliability of and provide consistency between the methodology developed in section 2 and the actual temporal behavior of the SBI layer, Wi-BLEx observational data from a winter period of collocated radiosonde-acoustic sounding observations at the NWS-PAFA station are provided (winter 2009-2010). The high-resolution profiling of the BL structure is displayed in this section to illustrate the fact that low-level inversions are effectively present at the levels where the radiosondes retrieve them, and they persist in time throughout the entire measurement period. In this case, the selected period was 11 to 13 January 2010. The flow at the BL level was from the E-ENE on 11 and 12 January, dominated by a strong pressure gradient between high pressure centered over Barrow,

AK and a low-pressure system in the Gulf of Alaska moving northward, approaching the Alaskan coast. The BL wind speed did not exceed 4 ms^{-1}. On 13 January, the wind direction changed to N-NE with wind speed lower than 2 ms^{-1}; consequently the wind field was observed to meander, indicating a decrease of the pressure gradient force. The vertical profile of the coefficient of turbulent temperature structure (C_T^2) was measured by sodar from 20 m to 400 m height most of the time, but up to 700 m at 10 m vertical resolution, and is represented in Figure 12. When performed from a monostatic sodar configuration, these measurements are sensitive only to the temperature turbulence (Holmgren et al., 1975; Neff, 1975; Neff and Coulter, 1988) and depict the BL structure. Figure 7 displays the thermodynamic profiles obtained by collocated radiosondes that indicate a steep temperature gradient close to the ground with surface temperature ranging from -30 to -40 ^oC throughout the entire period. The arrows in Figure 13 indicate the times when the radiosondes were launched. Table 7 summarizes a comparison of the BL structure detected by sodar with the structure detected by the radiosondes.

Collocated radiosonde and sodar measurements are concurrent during the entire period. Sodar profiling demonstrates the continuous presence of low inversion levels. The retrieval of SBI heights via acoustic sounder illustrates very low time variability for the 1-to-3-hour evaluated intervals (Table 7). In order to highlight the importance of the layered winter BL structure as a key ingredient in air pollution processes at high latitudes, this paragraph points to observational evidence of dynamic-radiative mechanisms that exist under the complexity of the layered structure and may pose an important modeling constraint. It is clearly evident that a complete assessment of the potential for pollutants

to accumulate in the EI layers requires a suite of mesoscale modeling combined with surface turbulence, radiation, and remote-sensing measurements. Nevertheless, based on the detailed vertical BL structure retrieved by sodar and its correspondence with collocated thermodynamic radiosondes, the possible dynamical process taking place during the occurrence of an EI can be hypothesized. From this hypothesis the potential role of this mechanism in air pollution can be inferred. A WAA case is illustrated in Figures 11 and 12 that leads to an EI layer that tops the SBI. The thermodynamic structure of the BL is described by the temperature profiles starting on 27 January (12 UTC) and continuing through 31 January (00 UTC). Figure 13 presents the series of temperature profiles that indicate the presence of an SBI and the formation over time of multiple EIs. The inversion layers detected by the algorithm are indicated in Table 8. Figure 14 presents the sodar profiles of C_T^2 around the time of radiosonde launch.

The sodar profiles at the beginning, on 27 January, 02 AST (Figure. 14), exhibit a strong inversion close to the ground at ~ 50 - 80 m above ground level with very low turbulence intensity in the upper levels. During the day sodar profiles indicted an increase of turbulent activity above 400 m AGL. This increase is depicted in the C_T^2 profiles, for example at 14:20 AST on 27 January (Figure 14) and overnight-morning during 28 January (Figure 14) while the surface temperature remained ~ -20 ^oC. Turbulence induced by temperature changes above 400 m increased due to the formation of an EI layer at 430 and 500 m Above Ground Level (AGL) as illustrated by the sodar sounding on 28 January, 07:10 AST (Figure 14). During this time the first inversion layer did not exhibit strong thermodynamic changes. However, later the inversion layer close to the

surface showed a decrease in the levels of C_T^2 indicating a decline in the stratification level (28 January, 16:10 AST, 29 January, 2:50 AST, and 29 January, 16:50 AST; Figure 14) due to the increase in the temperature gradient or "warming" in layers above the inversion level without significant increase of wind speed. The variations in C_T^2 are connected in the surface layer with the sensible heat flux. Therefore, a change in C_T^2 encompasses changes in the mean heat fluxes that are reflected in the vertical temperature gradient. This mechanism is observed in the evolution of the temperature profile from temperature-inversion-stratified to near neutrality, consistent with the warming trend at the surface indicated in Table 8. This mechanism, which includes decreasing of first inversion layer temperature gradient and consequently destroying inversions in the lower 1500 m or so, initiates mixing of upper-level emissions with surface (or close to the surface) gas and particulate matter emissions. The occurrence of this mechanism that introduces mixing in lower layers was explored theoretically by Garrat and Brost (1981). Estournel and Guédalia (1985), among other authors, investigated this phenomenon as it relates to dust layers in the desert of the Sahel; it is introduced here as one of the effects that can develop in the presence of a layered high-latitude winter BL structure.

In summary, this article characterizes the layered structure of the winter BL at high latitude in the sub-Arctic region of interior Alaska. The occurrence of multiple inversion layers driven by local (SBI) and synoptic (EI) phenomena was described. The statistical analysis of EI heights for the 2000 to 2009 period based on radiosonde observation data, representative of the continental-interior Alaska region, suggests that the presence of inversion layers is significant for October to March.

The meteorological conditions that initiate the formation of multiple inversion levels (SBI and EI) in the continental Fairbanks area at the meso-synoptic level include warm zonal winds between 925 hPa-850 hPa, or the presence of an anticyclone in the northern regions that yields clear or partly clear skies in the Fairbanks area, and constant synoptic flow. These mechanisms were described and verified using surface and upper-level synoptic charts as well as collocated remote-sensing instrumentation during Wi-BLEx.

A total number of 1974 EI-1 and 1128 EI-2 cases were reported. In the case of EI-1, 828 cases resulted from AC conditions, and within that ensemble 296 represent EI-2 (AC). On the other hand, 540 cases were determined to be WAA, and in 220 of these cases EI-2 (WAA) was present. In terms of synoptic transients, 559 cases were found to be either AC/WAA or WAA/AC. The remaining cases, fewer than 1%, were undetermined. Therefore, 42.96 % of the cases corresponded to AC while 28.02% corresponded to WAA and 29% corresponded to the synoptic transients.

The analysis of radiosonde vertical profiles from the NWS-PAFA for SBI detection is in agreement with collocated vertical observation data retrieved by acoustic sounding during Wi-BLEx and shows that under certain conditions the SBI is present most of the time in interior Alaska. The histograms for the statistical analysis of EI heights were limited to ~ 500 hPa. This restriction is of little importance when estimating the statistical parameters of inversion height distribution. This restriction is compensated for by the low mean height of the statistical mean and the maximum occurrence frequency, respectively, of the ~ 2719 m AGL and ~3124 m AGL layers.

The statistical heights obtained for the SBI are below the heights of the topographic features surrounding Fairbanks to the NW-N-NE while the statistical mean heights for EIs (at least the first and second EI) are just above the topography. This, in turn, severely restricts the dispersion of low-level emissions (e.g., from home heating and car exhaust) capped by the SBI (64.02 % of occurrences - see Table 3) and for upper-level emission plumes (i.e., from power plants) capped by EIs which occurred under an SBI ~ 84.86% (one EI) and 48.49% (two EIs) of the time. Although not definitively conclusive, the radiative feedback imposed by the EI layers can, in principle, be the forcing mechanism that reduces SBI stratification. This process will therefore allow for mixing and radiative interaction between the SBI and the first EI air masses that contain the main sources of local air pollution, as demonstrated by the sodar and thermodynamic profiles.

4.8 Acknowledgements

This research was supported by the Department of Environmental Conservation of Alaska Division of Air Quality grant G00006433-398755, and the Geophysical Institute and the College of Natural Sciences and Mathematics of the University of Alaska Fairbanks. The authors also acknowledge fruitful discussions with Dr. Nicole Moelders and Dr. Richard Collins, Department of Atmospheric Sciences, University of Alaska Fairbanks, use of the ESRL–NOAA reanalysis data base, and the personnel of the NWS-NOAA Fairbanks and the School of Natural Resources and Agricultural Sciences of the University of Alaska Fairbanks for facilitating the sodar deployment at the FAI station and at the University of Alaska Campus Farm.

4.9 References

Andre, J.C., and L. Mahrt, 1982: The nocturnal surface inversion and influence of clear-air radiative cooling. *J. Atmos. Sci.*, **39**, 864–878.

Angevine, W., H. Baltink, and F. Bosveld, 2001: Observations of the morning transition of the convective boundary layer. *Boundary-Layer Meteor.*, **101**, 209-227.

Beirlant, J., G. Dierckx, and A. Guillou, 2005: Estimation of the extreme-value index and generalized quantile plots. *Bernoulli*, **11**, 6, 949-970.

Benson, C.S., 1965: *Ice Fog: Low Temperature Air Pollution, Defined with Fairbanks, Alaska as Type Locality.* College, Alaska: University of Alaska Fairbanks, Geophysical Institute, pp: 134.

Billelo, M.A., 1966: Survey of arctic and subarctic temperature inversions. *U.S. Army Cold Regions Research & Engineering Laboratory*, pp: 36. TR 161.

Bodurtha, F. T., 1952: An investigation of anticyclogenesis in Alaska. *J. Meteor.*, **9**, 118-125.

Bourne, S.M., U.S. Bhatt, J. Zhang, and R. Thoman, 2010: Surface-based temperature inversions in Alaska from a climate perspective. *Atmos. Res.,* **95**, 353-366.

Bowling, S.A., T. Ohtake, and C.S. Benson, 1968: Winter pressure systems and ice fog in Fairbanks, Alaska. *J. Appl. Met.*, **7**, 961-968.

Bradley, R.S., F.T. Keimig, and H.F. Diaz, 1992: Climatology of surface-based inversions in the North American Arctic. *J. Geophys. Res.*, **97**, 15,699-15,712.

Brown, E.H., and F.F. Hall, Jr., 1978: Advances in atmospheric acoustics. *Rev. Geophys. Space Phys.*, 16, 47-110.

Busch, N., U. Ebel, H. Kraus, and E. Schaller, 1982: The structure of the subpolar inversion-capped ABL. *Met. Atmos. Phys.*, 31, 1-2, 1-18.

Byers, H.R., and V.P. Starr, 1941: The circulation of the atmosphere in high latitudes during winter. *Mon. Wea. Rev. Supplement N°. 47,* pp: 34.

Cassano, E.N., J.J. Cassano, and M. Nolan, 2011: Synoptic weather pattern controls on temperature in Alaska. *J. Geophys. Res.*, **116**, pp: 19. D11108.

Chen, N., D. Guan, C. Jin, A. Wang, J. Wu, and F. Yuan, 2011: Influences of snow event on energy balance over temperate meadow in dormant season based on eddy covariance measurements. *J. Hydrology*, **399**, 1-2, 100-107.

Cohen, L., D. Helmig, W. Neff, A. Grachev, and C. Fairall, 2007: Boundary-layer dynamics and its influence on atmospheric chemistry at Summit, Greenland. *Atmos. Environ.*, **41**, 5044-5060.

Csanady, G.T., 1974: Equilibrium theory of the planetary boundary layer with an inversion lid. *Boundary-Layer Meteor.*, **6**, 63-79.

Curry, J.A., 1983: On the formation of continental polar air. *J. Atmos. Sci.,* **40**, 2279-2292.

Curry, J.A., 1987: The contribution of radiative cooling to the formation of cold-core anticyclones. *J. Atmos. Sci.,* **44**. 2575-2592.

Dalrymple, P.C., 1966: A physical climatology of the Antarctic plateau. *Studies in Antarctic Meteorology*, Rubin, M.J., Ed., Antarctic Research Series, Vol. 9, Amer. Geophys. Union, 195-231.

Estournel, C., R. Vehil, D. Guédalia, J. Fontan, and A. Druilhet, 1983: Observations and modeling of downward radiative fluxes in urban/rural areas. *J. Appl. Meteor.* **22**, 134-142.

Estournel, C., and D. Guédalia, 1985: Influence of geostrophic wind on atmospheric nocturnal cooling. *J. Atmos. Sci.,* **42**, 23, 2695-2698.

Fernando, H.J.S., J.C.R. Hunt, and D.J. Carruthers, 1994: Turbulence, waves and mixing at stratified density interfaces: Modeling and experiments. *Stably Stratified Flows*, Castro, I.P. and N.J. Rockliff, Eds., Oxford University Press, 175-200.

Fochesatto, J., P. Drobinski, C. Flamant, D. Guédalia, C. Sarrat, P.H. Flamant, and J. Pelon, 2001a: Observations and modeling of the atmospheric boundary layer nocturnal-diurnal transition during the ESQUIF experiment. *Advances in Laser Remote Sensing*, Dabas, A., C. Loth, and J. Pelon, Eds., Ecole Polytechnique Editions, Paris, France, 439-442.

Fochesatto, J., P Drobinski, C. Flamant, D. Guédalia, C. Sarrat, P. Flamant, and J. Pelon, 2001b: Evidence of dynamical coupling between the residual layer and the developing convective boundary layer. *Boundary-Layer Meteor.,* **99**, 451-464.

Fochesatto, J., R. Collins, C. Cahill, J. Connor, and J. Yue, 2006: Downward mixing in the continental Arctic boundary layer during a smoke episode. *Reviewed and revised papers presented at the Twenty-Third International Laser Radar Conference (ILRC)*, *Nara, Japan, 24-28 July,* 817-820.

Fuggle, R.F., and T.R. Oke, 1976: Long-wave radiative flux divergence and nocturnal cooling of the urban atmosphere. I: Above roof-level. *Boundary-Layer Meteor.,* **10**, 113-120.

Garrat, J.R., and R.A. Brost, 1981: Radiative cooling effect within and above the nocturnal boundary layer. *J. Atmos. Sci.,* **38**, 2730-2745.

Guédalia, D., C. Estournel, and R. Vehil, 1984: Effects of Sahel dust layers upon nocturnal cooling of the atmosphere. *J. Climate Appl. Meteorol.,* **23**, 644-650.

Hartmann, B., and G. Wendler, 2005: Climatology of the winter surface temperature inversion in Fairbanks, Alaska. *Proceedings of the 85th Annual Meeting of the American Meteorological Society, San Diego, CA,* 1-7.

Holmgren, B., L. Spears, C. Wilson, and C.S. Benson, 1975: Acoustic soundings of the Fairbanks temperature inversions. *Climate of the Arctic: Proceedings of the AAAS-AMS conference, Fairbanks, Alaska. 1973. Weller, G. and S.A. Bowling, Eds., Geophysical Institute, University of Alaska,* 293-306.

Hudson, S.R., and R.E. Brandt, 2005: A look at the temperature inversions over the Antarctic plateau. *J. Climate*, **18**, 1673-1696.

Huff, D.M., P.L. Joyce, G.J. Fochesatto, and W.R. Simpson, 2010: Deposition of dinitrogen penta-oxide, N_2O_5, to the snowpack at high latitudes. *Atmos. Chem. Phys. Discuss.*, **10**, 25329–25354, 2010 doi:10.5194/acpd-10-25329-2010.

Jayaweera, K., G. Wendler, and T. Ohtake, 1975: Low Cloud Cover And the Winter Temperature of Fairbanks. *Climate of the Arctic: Proceedings of the AAAS-AMS conference, Fairbanks, Alaska. 1973. Weller, G. and S.A. Bowling, Eds., Geophysical Institute, University of Alaska,* 316-322.

Kahl, J., 1990: Characteristics of the Low-Level Temperature Inversion Along the Alaskan Arctic coast. *Int. J. Clim.*, **10**, 537-548.

Kahl, J.D., M.C. Serreze, and R.C. Schnell, 1992: Tropospheric Low-Level Temperature Inversions in the Canadian Arctic. *Atmosphere-Ocean*, **30**, 4, 511-529.

Kallos, G., P. Kassomenos, and R.A. Pielke, 1993: Synoptic and Mesoscale Weather Conditions During Air Pollution Episodes in Athens, Greece. *Boundary-Layer Meteor.*, **62**, 163-184.

Kankanala, P., 2007: Doppler Sodar observations of the winds and structure in the lower atmosphere over Fairbanks, Alaska. MS Thesis, Department of Atmospheric Sciences, University of Alaska Fairbanks. Available at: ffden-2.phys.uaf.edu /atm/Students/theses/Pavan_thesis.pdf, pp: 65.

Katsoulis, B.D., 1988a: Some meteorological aspects of air pollution in Athens, Greece. *Meteorol. Atmos. Phys.,* **39**, 203-212.

Katsoulis, B.D., 1988b: Aspects of the occurrence of persistent surface inversions over Athens basin, Greece. *Meteorol. Atmos. Phys.,* **39**, 98-107.

Lilliefords, H.W., 1967: On the Kolmogorov-Smirnov test for normality with mean and variance unknown. *J. Amer. Stat. Assoc.*, **62**, 399-402.

Malingowski, J., 2010: An observational study of the surface-based radiation temperature inversion in Fairbanks, Alaska. MS Thesis, Department of Atmospheric Sciences, University of Alaska Fairbanks.. Available at:ffden-2.phys.uaf.edu/atm/Students /theses/JMalingowski_MSthesis_ 2010.pdf, pp: 91.

Maxwell, J.B., 1982: The climate of the Canadian Arctic islands and adjacent water, Volume 2. Climatological Studies N^{o} 30, Environment Canada, Atmospheric Environment Service, 1980-1982. Ottawa, Canada.

Mayfield, J.A., and G.J. Fochesatto, 2010: A study of elevated and surface-based inversions in the Interior of Alaska. *Proceedings of the American Geophysical Union Fall Meeting 2010,* Abstract #A21C-0070.

Milionis, A.E., and T.D. Davies, 1992: A five-year climatology of elevated inversions at Hemsby (UK). *Int. J. Clim.*, **12**, 205–215. doi: 10.1002/joc.3370120209.

Moelders, N., and G. Kramm, 2010: A case study on wintertime inversions in Interior Alaska with WRF. *Atmos. Res.,* **95**, 314-332.

Neff, W.D., 1975: Quantitative evaluation of acoustic echoes from the planetary boundary layer. Tech. Rep. ERL 322-WPL, National Oceanic and Atmospheric Administration [available as PB 253-207 from the National Technical Information Center, Springfield, VA.]. pp.34.

Neff, W.D., and R.L. Coulter, 1988: Acoustic Remote Sensing. In: *Probing the Atmospheric Boundary Layer*, Lenschow, D.H., Ed., Amer. Meteor. Soc., 201-235.

Oke, T.R., 1978: *Boundary Layer Climates*. Methuen & Co. Ltd., pp: 434.

Pahlow, M., J. Kleissl, M. Parlange, J. Ondov, and D. Harrison, 2005: Atmospheric Boundary-Layer Structure Observed During A Haze Event Due to Forest-Fire Smoke. *Boundary-Layer Meteor.*, **114**, 53-70.

Petterssen, S., W.C. Jacobs, and B.C. Haynes, 1956: Meteorology of the Arctic. *Naval Research Report*, OPNAV PO3-3.

Plate, E.J., 1971: Aerodynamic Characteristics of Atmospheric Boundary Layers. U.S. Atomic Energy Commission, Division of Technical Information [available from National Technical Information Service, U.S. Dept. of Commerce, Springfield, Va.] pp.190.

Prezerakos, N.G., 1998: Lower Tropospheric Structure and Synoptic Scale Circulation Patterns During Prolonged Temperature Inversions over Athens, Greece. *Theor. Appl. Climatol.*, **60**, 63-76.

Reed, R.J., and B.A. Kunkel, 1960: The Arctic Circulation in Summer. *J. Atmos. Sci.*, **17**, 5, 489-506.

Robson, R.E., 1983: On the Theory of Plume Trapping By An Elevated Inversion. *Atmos. Environ.*, **17**, 10, 1923-1930.

Romanovsky, V.E., and T.E. Osterkamp, 2000: Effects of Unfrozen Water on Heat and Mass Transport Processes in the Active Layer and Permafrost. *Perm. Periglac. Proc.*, **11**, 219–239.

Schwartz, B.E, and M. Govett, 1992: A Hydrostatically Consistent North American Radiosonde Data Base At the Forecast Systems Laboratory, 1946–present. Tech. Memo. ERL-FSL-4.[Available from NOAA, 325 Broadway, Boulder, CO 80303.]. pp. 81.

Serreze, M., J. Kahl, and R. Schnell, 1992: Low-level Temperature Inversions in the Eurasian Arctic and Comparisons with Soviet Drifting Station Data. *J. Climate*, **5**, 615-629.

Shupe, M.D., and J.M. Intrieri, 2004: Cloud Radiative Forcing of the Arctic Surface: The Influence of Cloud Properties, Surface Albedo, and Solar Zenith Angle. *J. Climate.,* **17,** 616-628.

Stone, R.S., 1997: Variations in Western Arctic Temperatures In Response to Cloud Radiative and Synoptic-Scale Influences. *J. Geophys. Res.,* **102**, D18, 21,769-21,776.

Stull, R., 1988: *An Introduction to Boundary Layer Meteorology*. Kluwer Academic Publishers, Dordrecht, The Netherlands. pp. 666.

Taylor, J.A., and R.A. Yates, 1967: *British Weather in Maps. 2nd Ed.* St. Martin's Press, pp. 315.

Wendler, G., and K. Jayaweera, 1972: Some measurements on the development of the surface inversion in Central Alaska during winter. *Pure and Applied Geophysics*, **92**, 209-221.

Wendler, G., and P. Nipcon, 1974: Low-level temperature inversions in Fairbanks, central Alaska. *Mon. Wea. Rev.*, **103**, 34-44.

Wexler, H., 1936: Cooling in the lower atmosphere and the structure of polar continental air. *Mon. Wea. Rev.*, **64**, 122-136.

Wexler, H., 1941: Observation of nocturnal radiation at Fairbanks, Alaska and Fargo, North Dakota. *Mon. Wea. Rev. Supplement N°. 46, pp: 21.*

Wilks, D. S., 2006: *Statistical Methods in the Atmospheric Sciences. Academic Press*, pp: 627.

Willis, G., and J. Deardorff, 1978: A laboratory study of dispersion from an elevated source within a modeled convective planetary boundary layer. *Atmos. Environ.*, **12**, 1305-1311.

Willis, R.A., and G.K. Grice, 1976: The Winter time Arctic Front And its effects on Fairbanks. NOAA Technical Memorandum NWS AR-16. 23 pp.

Zhang, Y., D.J. Seidel, J.-Ch. Golaz, C. Deser, and R. Tomas, 2011: Climatological Characteristics of Arctic and Antarctic Surface-Based Inversions. *J. Climate*, **24**, 5167-5186.

4.10 Figures

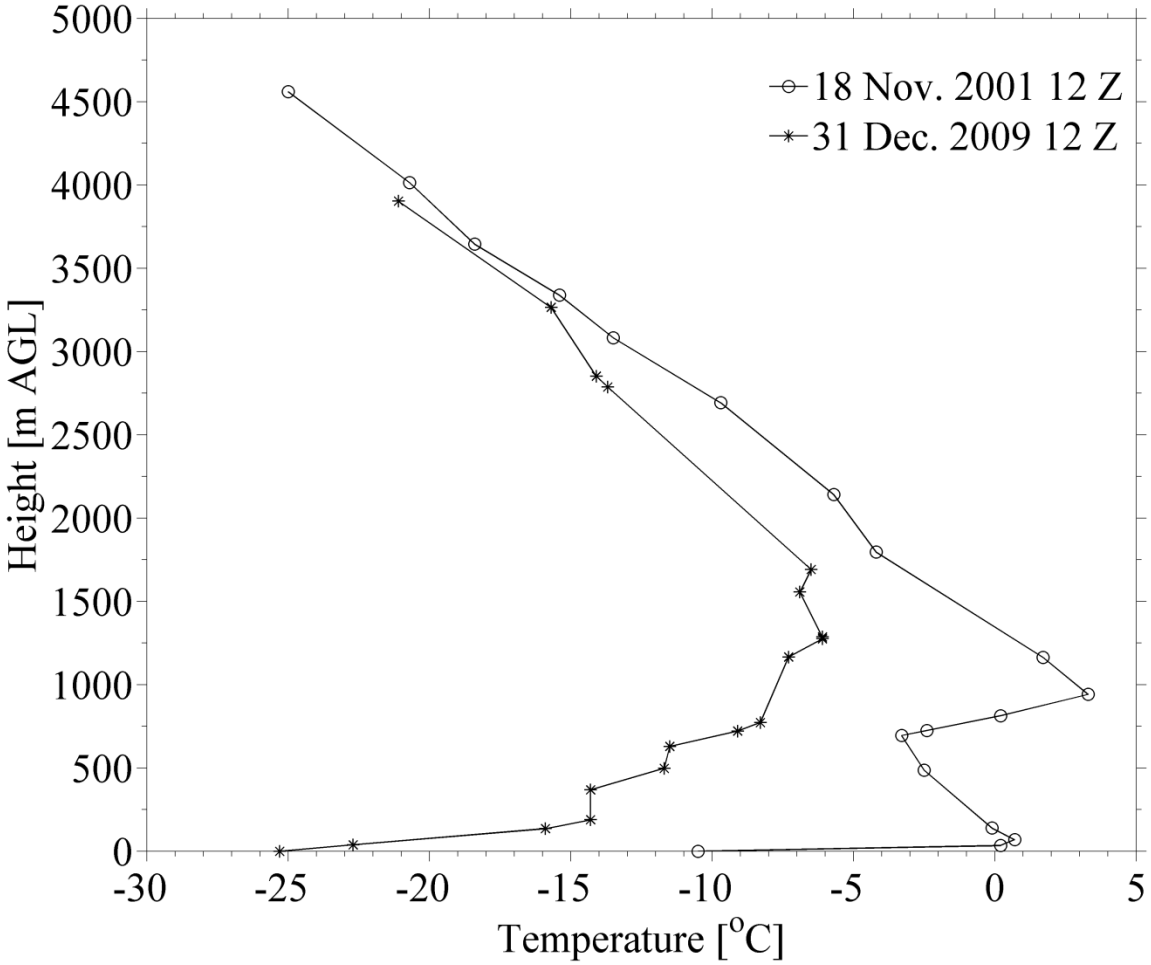

Figure 1. Examples of temperature profiles indicating multiple inversion layers. The vertical axis is height (m) above ground level (PAFA station is at 138 m above sea level). The examples shown indicate stratified layers within the first inversion with different strengths indicated by the case of 18 Nov. 2001 (strongly stratified) and 31 Dec. 2009 (stratified).

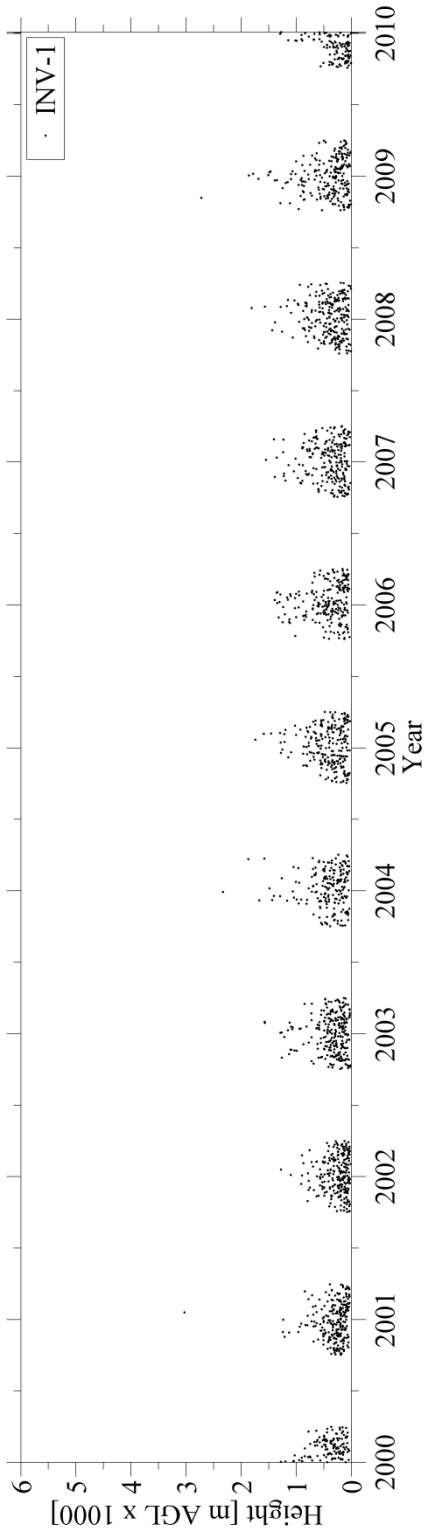

Figure 2a. Temporal series of inversion heights and statistical characterization. (INV-1)

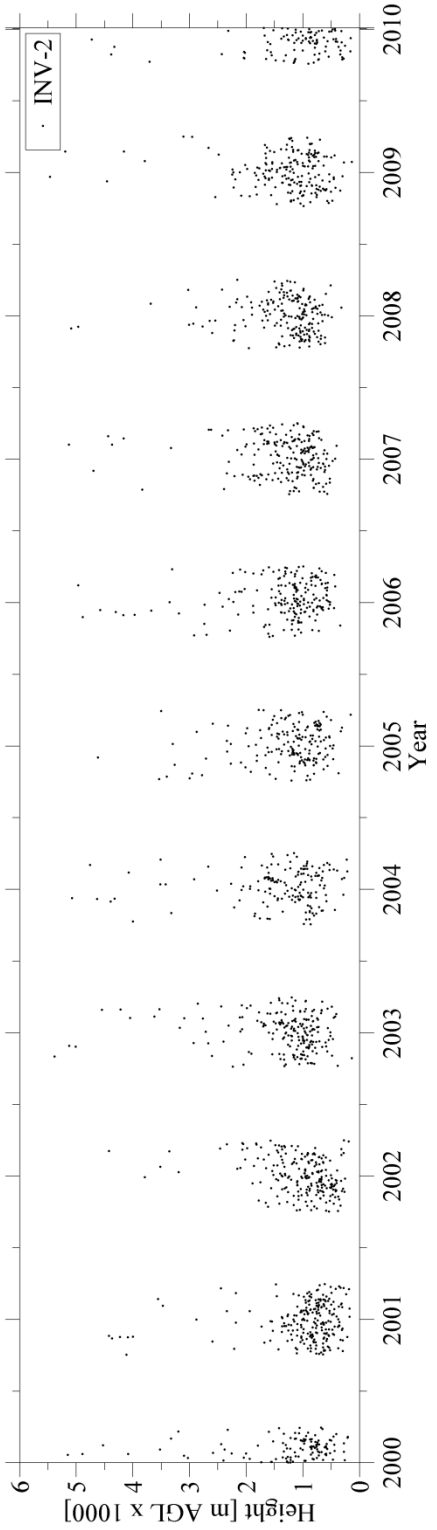

Figure 2b. Temporal series of inversion heights and statistical characterization. (INV-2)

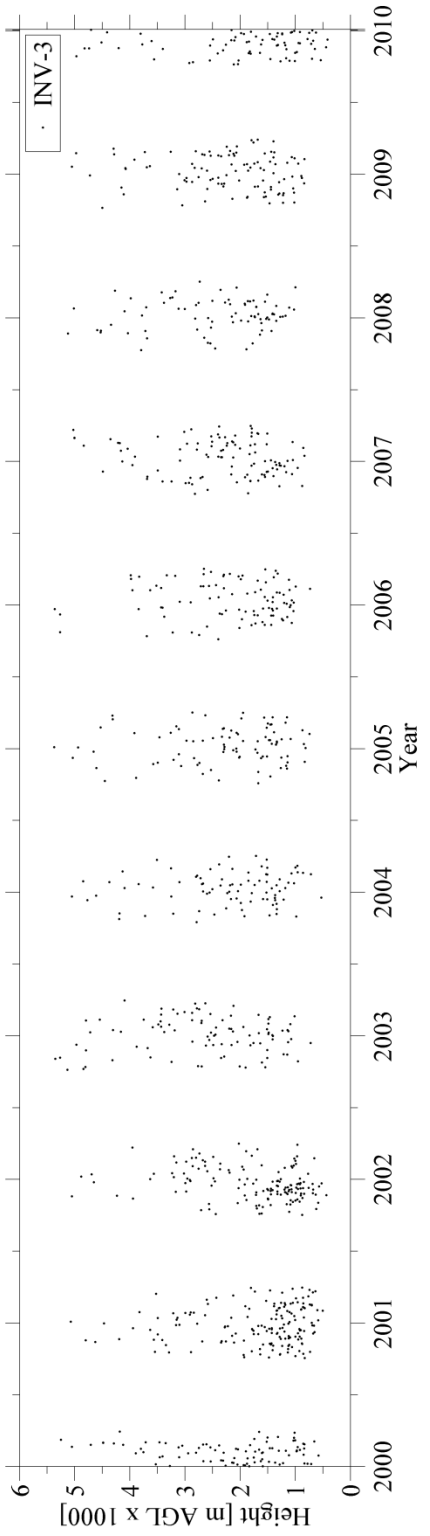

Figure 2c. Temporal series of inversion heights and statistical characterization.

Figure 3. Figure 3a) INV 1: Y axis: Number of Occurrence; left Y axis: cumulative probability density function CPDF) corresponding to the temporal series. The heights are expressed in [m AGL X 1000]. Figure 3b) INV 2: Y axis: Number of Occurrence; left Y axis: cumulative probability density function CPDF) corresponding to the temporal series. The heights are expressed in [m AGL X 1000]. Figure 3c) is the INV 3: Y axis: Number of Occurrence; left Y axis: cumulative probability density function CPDF) corresponding to the temporal series. The heights are expressed in [m AGL X 1000].

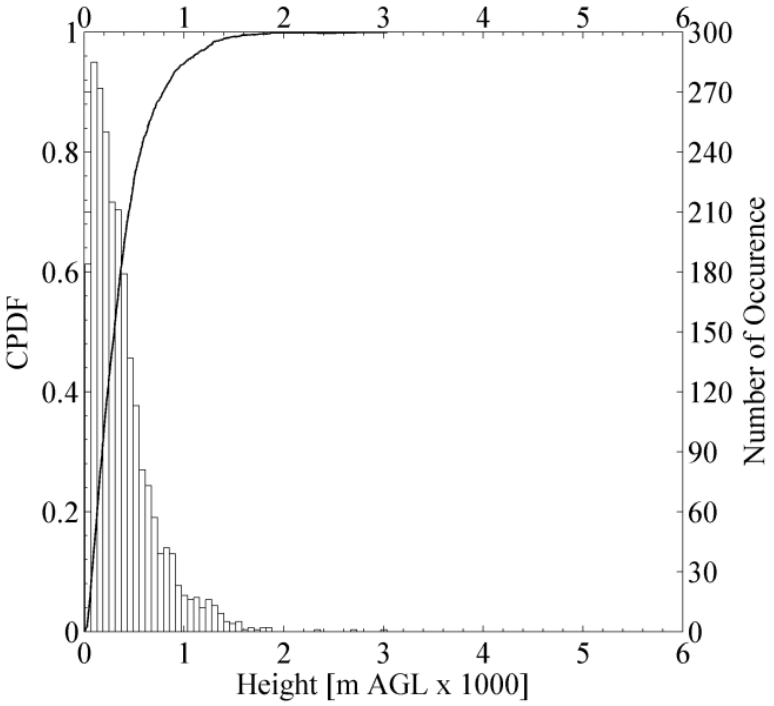

Figure 3a

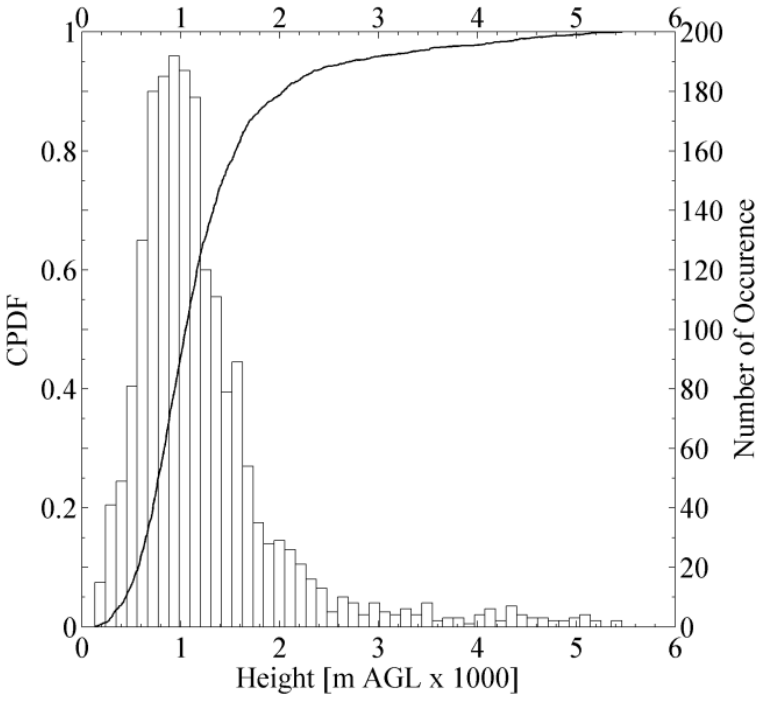

Figure 3b

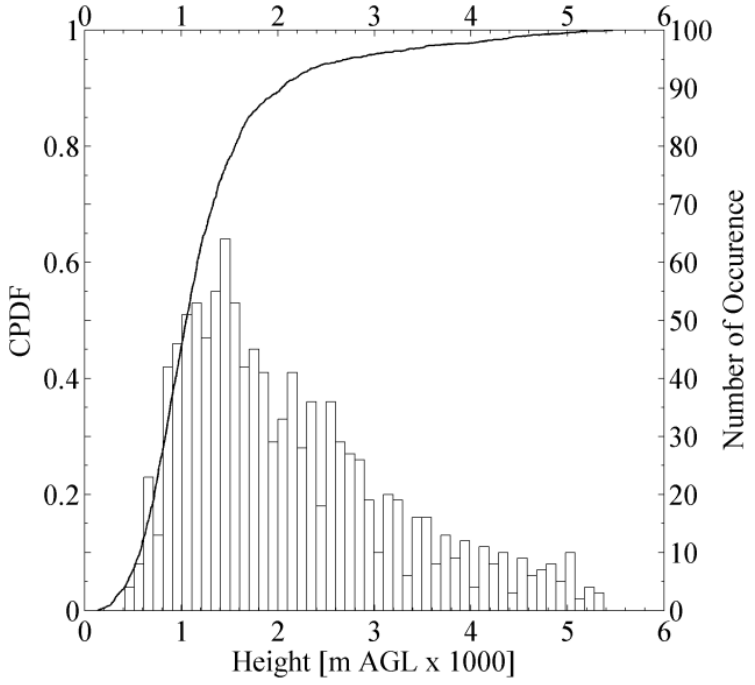
CPDF
Number of Occurence
Height [m AGL x 1000]
0
0.2
0.4
0.6
0.8
1
0
10
20
30
40
50
60
70
80
90
100
0
1
2
3
4
5
6

Figure 3c

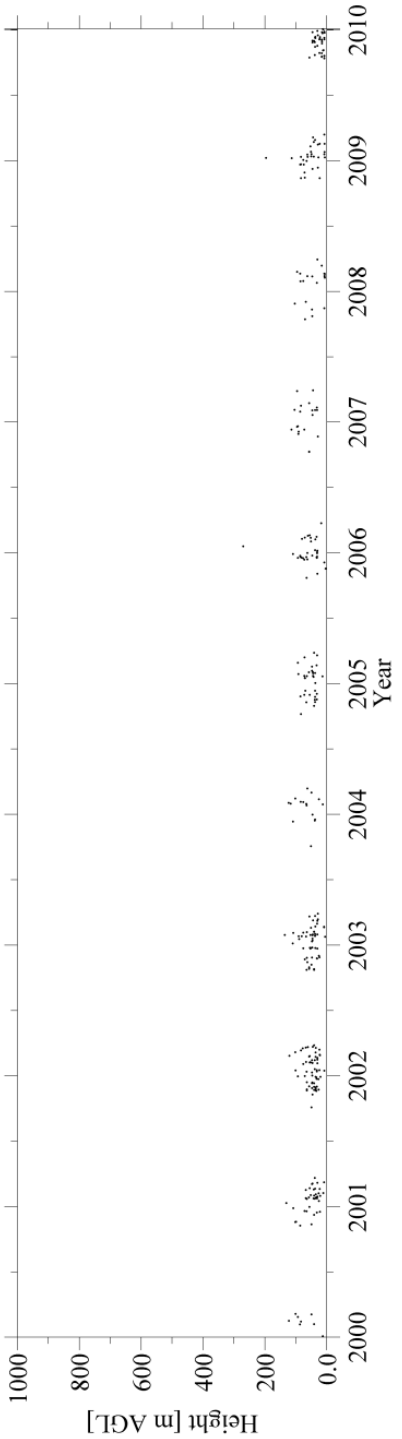

Figure 4. Temporal series of stratified layers within the surface-based inversion. Defined by a thermal gradient $m_k < 10\ ^oC/100$ m The heights are expressed in m AGL.

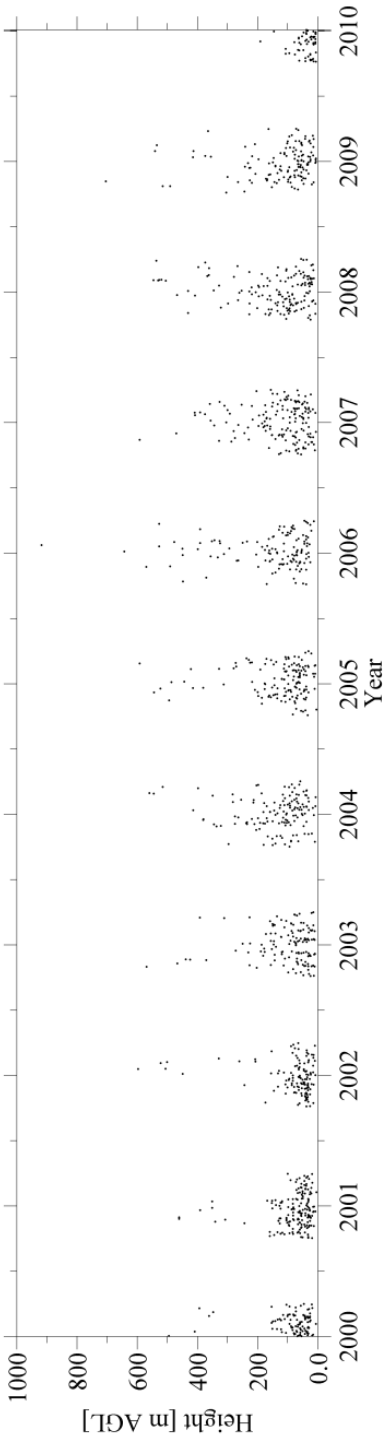

Figure 5. Temporal series of stratified layers within the surface-based inversion. Defined by a thermal gradient $m_k > 10\ ^oC/100$ m. The heights are expressed in m AGL.

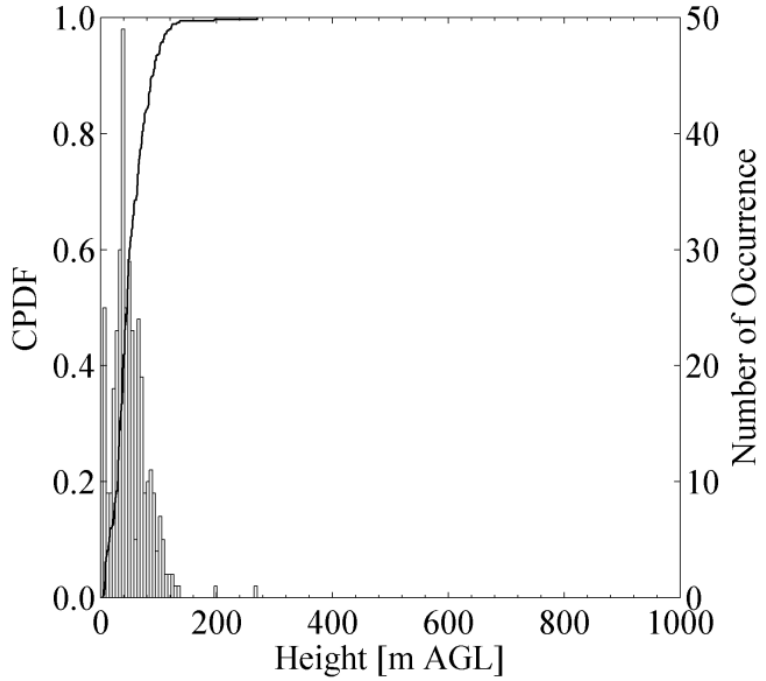

Figure 6a

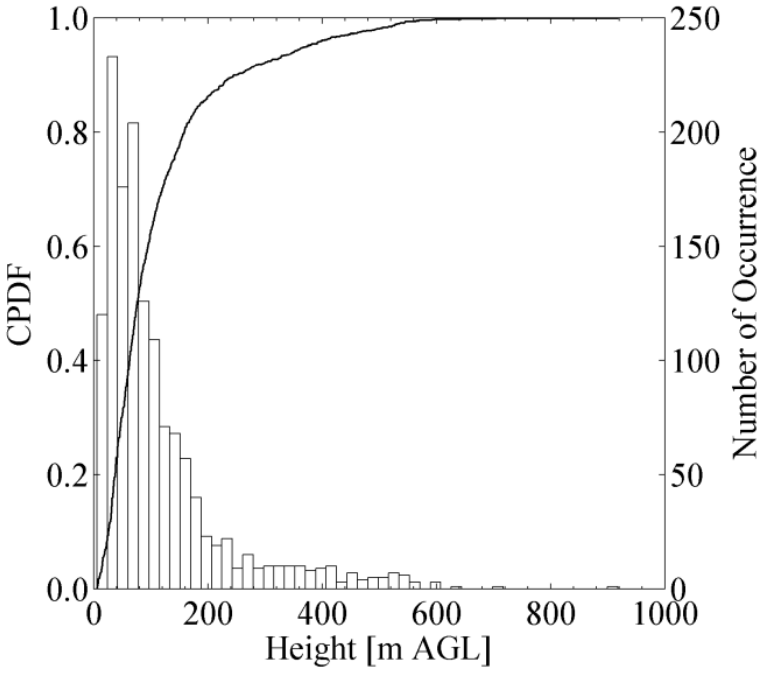

Figure 6b

Figure 6. Statistical characterization of the stratified layers within the surface-based inversion. Figure 6a represents stratified layers and Figure 6b represents strongly stratified layers within the SBI.

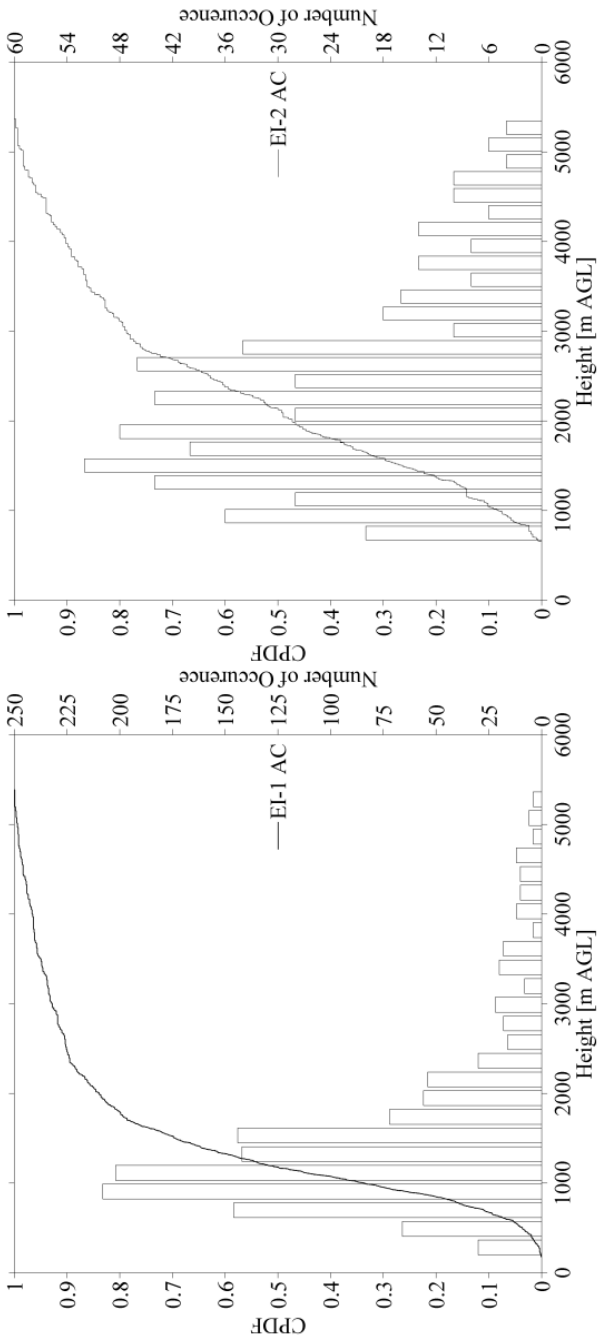

Figure 7. Statistical analysis of the temporal series of Elevated Inversion (EI) layers during Anticyclonic (AC). Vertical axis illustrates the histogram (number of occurrence on the right y axis) and the cumulative probability density function (CPDF) (left y axis). The Figures correspond to AC situations for EI-1 (Bottom) and EI-2 (Top). Lower panels correspond to WAA situations for EI-1 (left) and EI-2 (right).

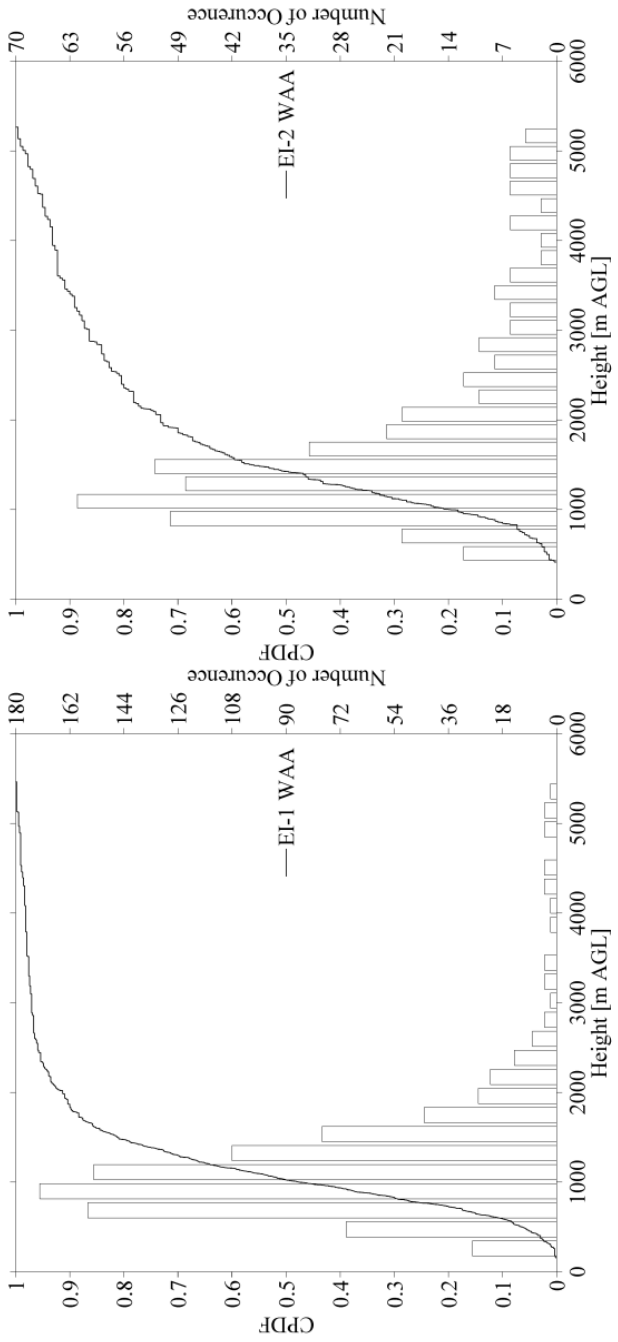

Figure 8. Statistical analysis of the temporal series of Elevated Inversion (EI) layers during Warm Air Advection (WAA) conditions. Vertical axis illustrates the histogram (number of occurrence on the right y axis) and the cumulative probability density function (CPDF) (left y axis). Figures correspond to WAA situations for EI-1 (Bottom) and EI-2 (Top).

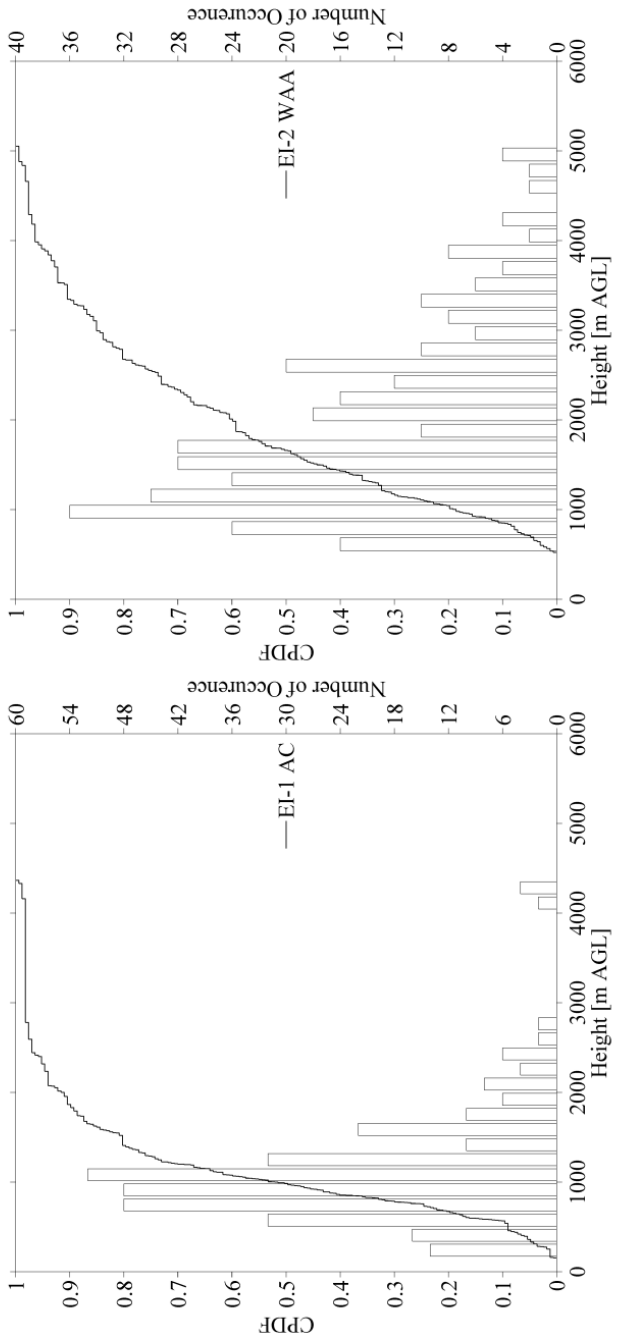

Figure 9. Statistical analysis of the temporal series of Elevated Inversion (EI) layers during synoptic transients. Vertical axis illustrates the histogram (number of occurrence on the right y axis) and the cumulative probability density function (CPDF) (left y axis). The bottom figure represents the case of EI-1 AC and top EI-2 WAA.

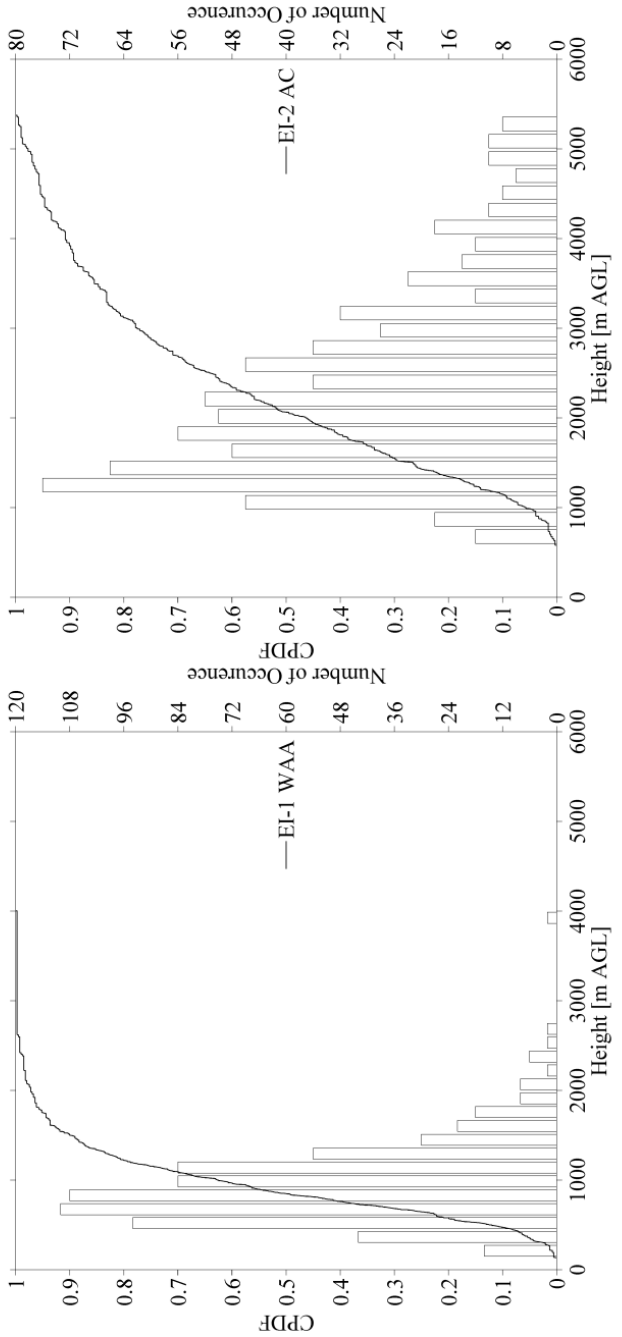

Figure 10. Statistical analysis of the temporal series of Elevated Inversion (EI) layers during synoptic transients. Vertical axis illustrates the histogram (number of occurrence on the right y axis) and the cumulative probability density function (CPDF) (left y axis). The bottom figure represents the cases of EI-1 WAA and the top figure EI-2 AC.

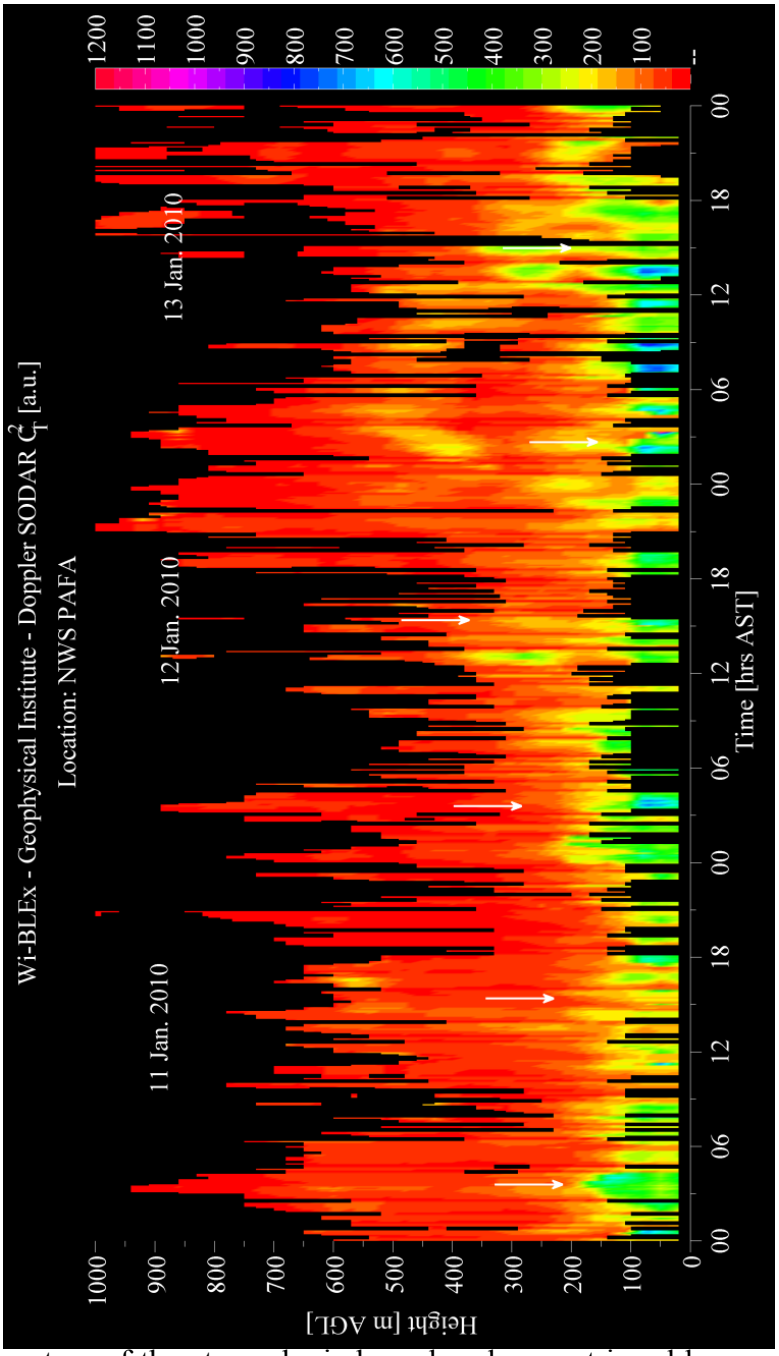

Figure 11. Vertical structure of the atmospheric boundary layer retrieved by monostatic Doppler Phased Array Acoustic Sounder (Sodar Remtech PA-2) from 11 to 13 January, 2010 in Fairbanks, Alaska. The profiles start at 20 m AGL with a vertical resolution of 10 m and an average time of 10 min. The color scale is coded linear. Vertical arrows indicate the times when collocated radiosonde profiles are available for comparison at 00 Z and 12 Z at the NWS-PAFA station. The horizontal axis is time in Alaska Standard Time (AST)

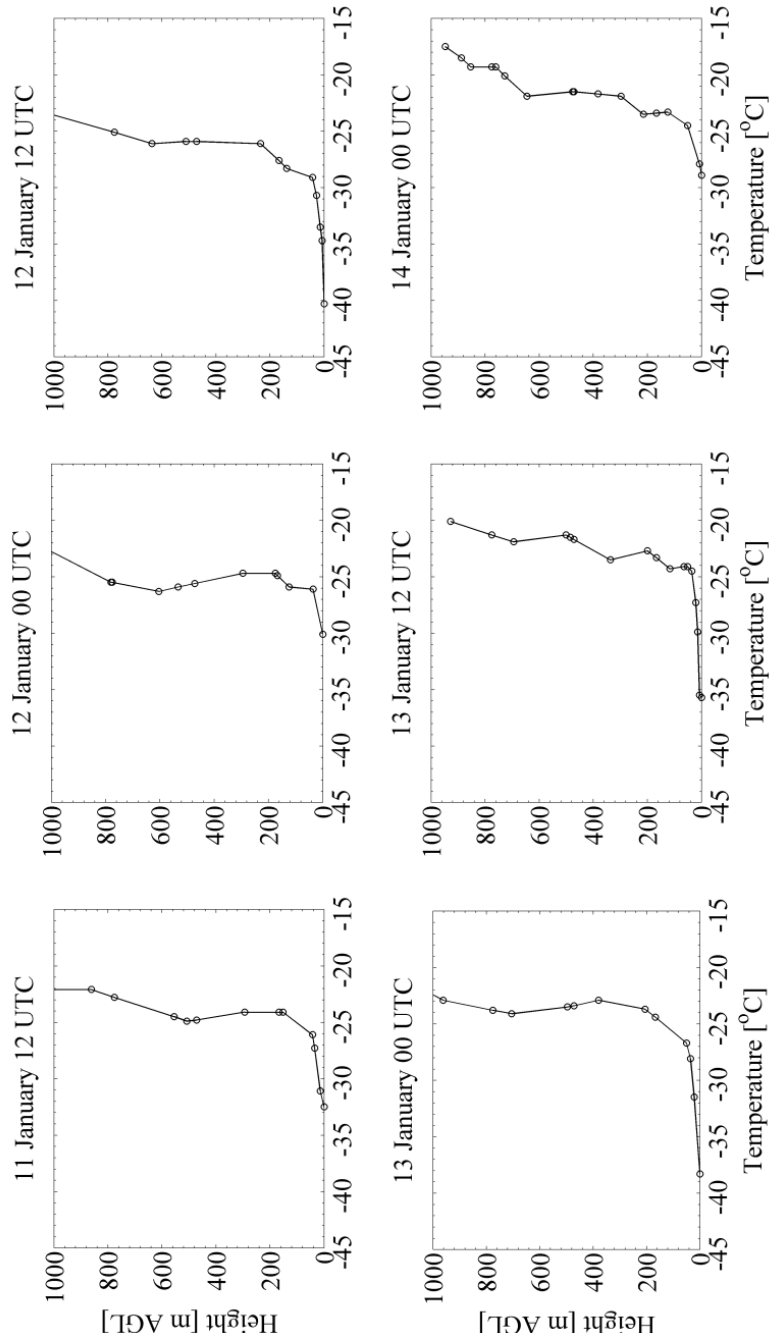

Figure 12. Thermodynamic structure of the boundary layer retrieved by radiosondes 00 and 12 Z from 11 to 14 January of 2010 at the NWS-PAFA station in Fairbanks, Alaska. The dates and times are in UTC for radiosonde launches indicated in the small heading of each plot. Vertical axis is m AGL and horizontal axis is temperature in ^{o}C

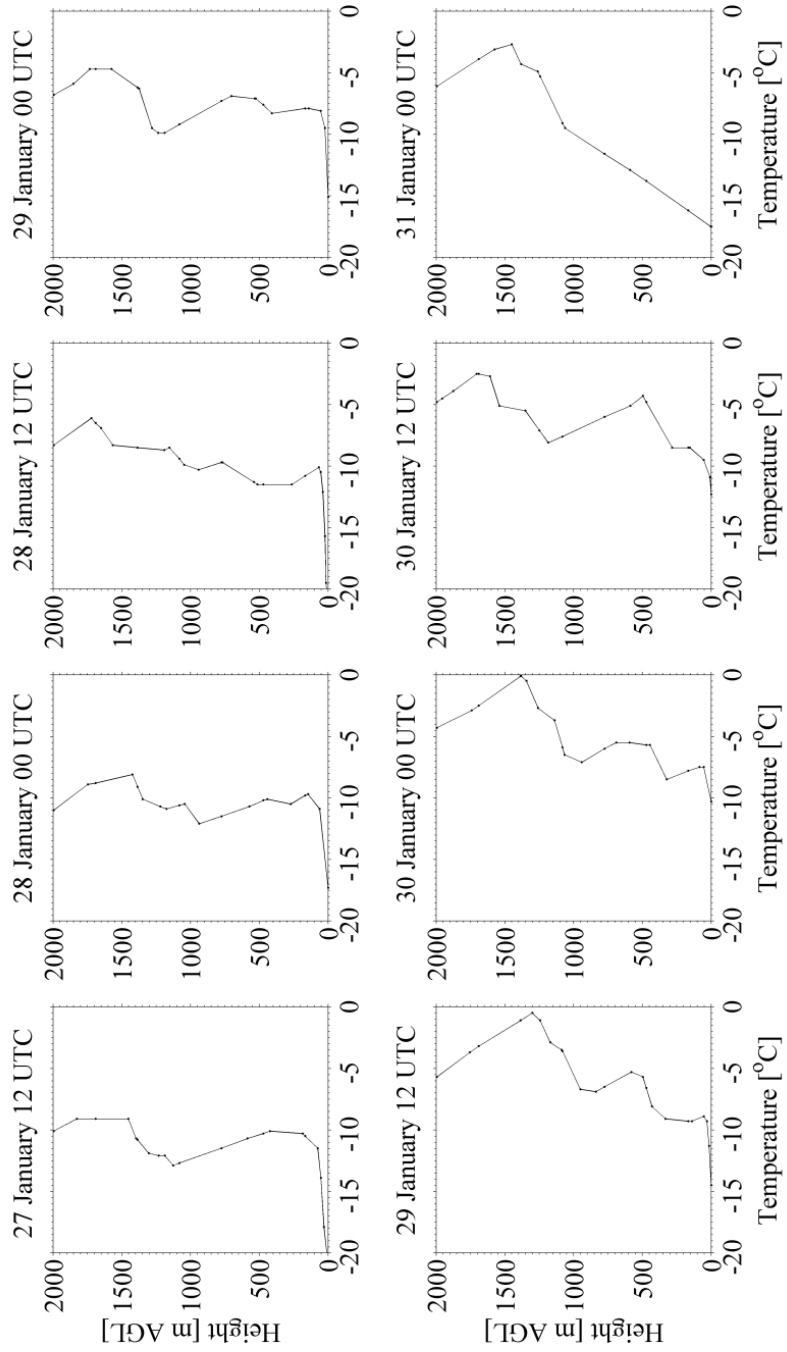

Figure 13. Temperature profiles starting on 27 January at 12 UTC and continuing until 31 January at 00 UTC collected by radiosonde launches at National Weather Service station PAFA in Fairbanks, Alaska. Vertical axis is m AGL and horizontal axis is temperature in ^{o}C.

Figure 14. Sodar profiles relative to the turbulence temperature structure coefficient C_T^2. The figures illustrate the presence of the first inversion at an altitude between 50 and 80 m. Figures 14 (a-f) show the formation of a second elevated inversion above 400 m AGL; The figures illustrate the reduced stratification at lower levels over time given by the decreasing intensity of C_T^2 over.

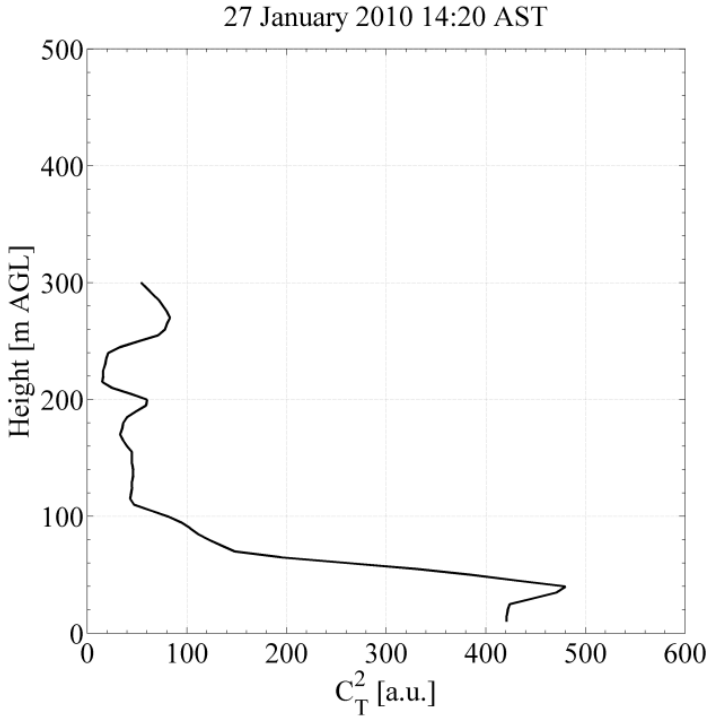

Figure 14a

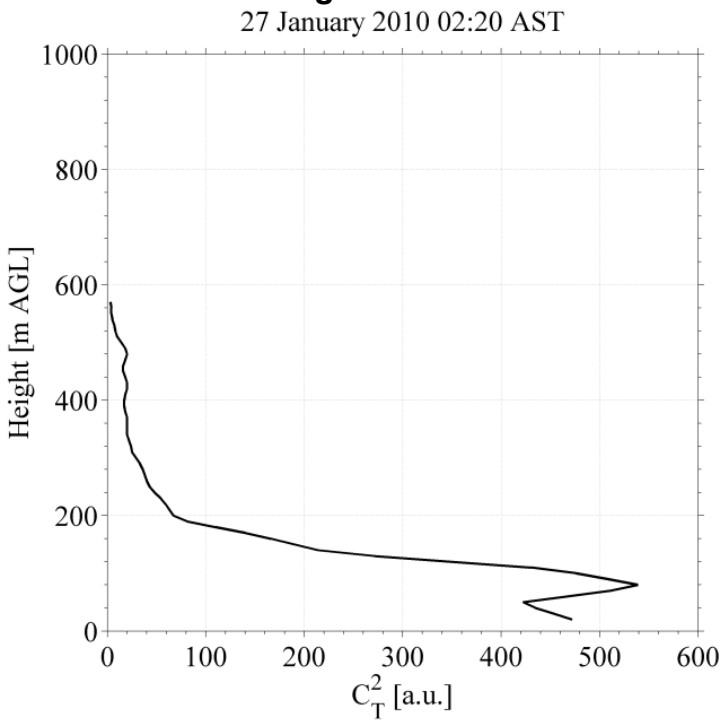

Figure 14b

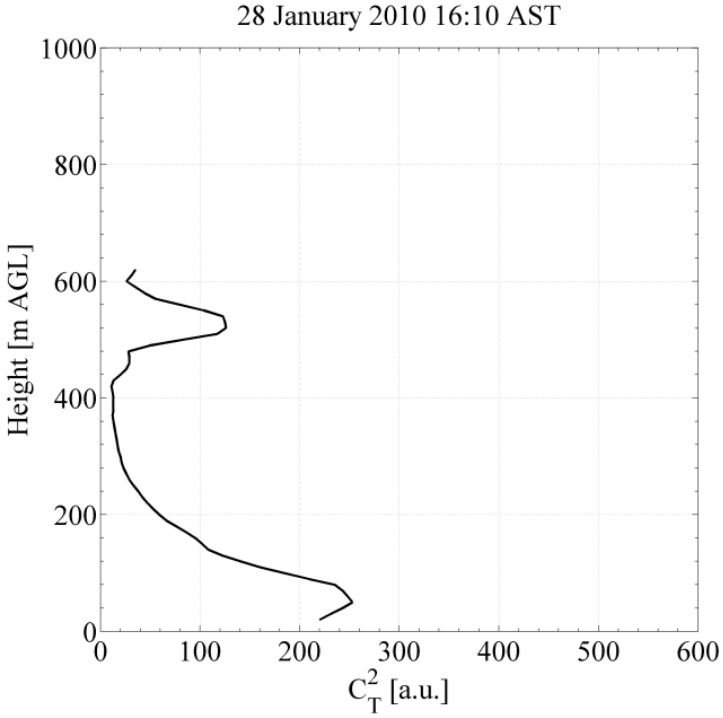

Figure 14c

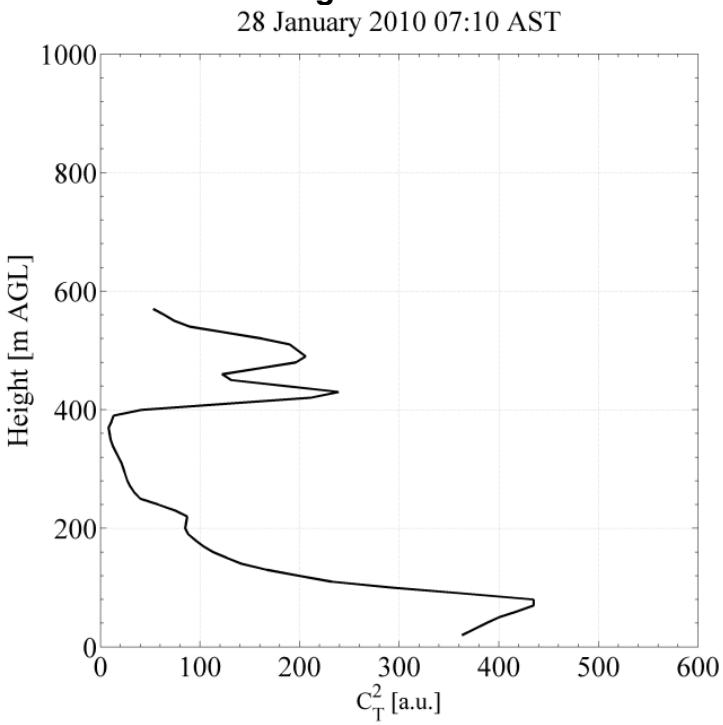

Figure 14d

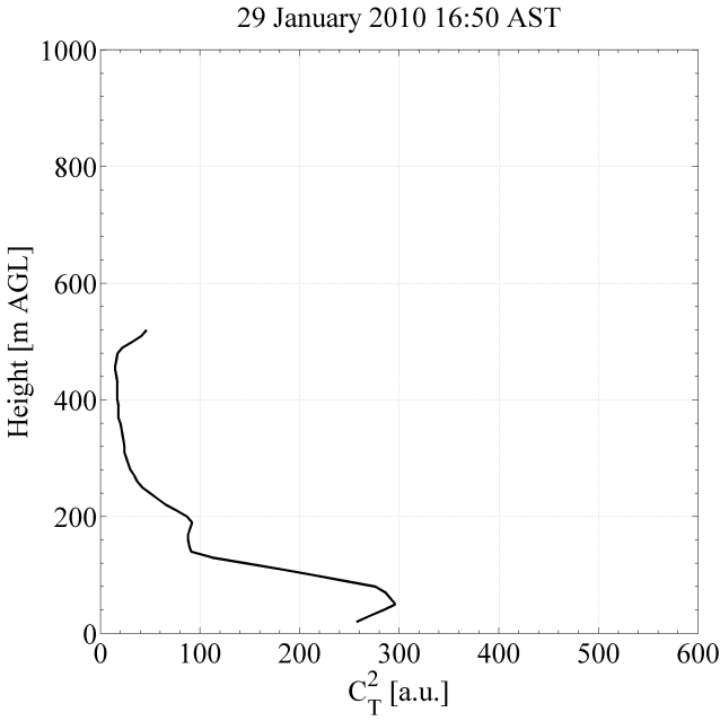

Figure 14e

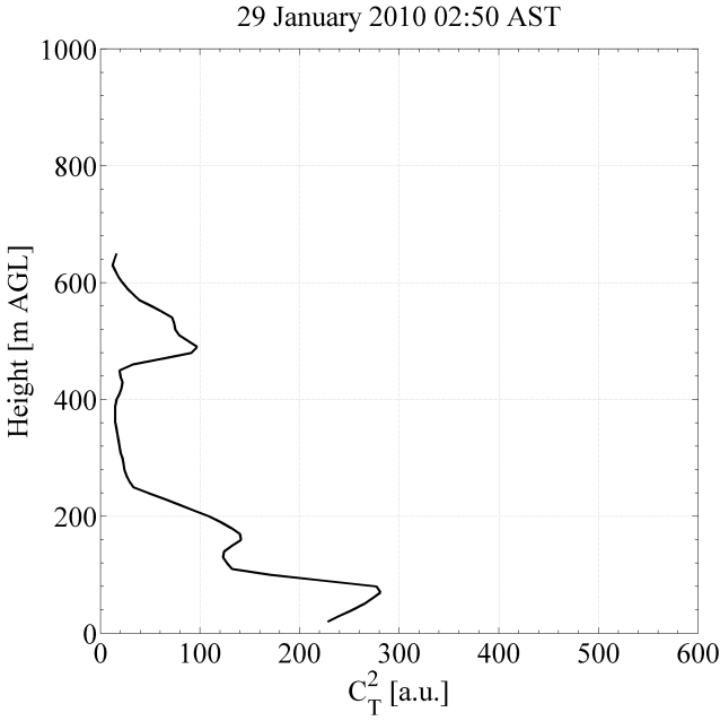

Figure 14f

4.11 Tables

TABLE 1. Number of average radiosonde data points <N> and standard deviation σ_N available per atmospheric pressure thickness and layer height obtained from a total of 2326 samples.

Pressure Level	**500-1000**	**700-1000**	**850-1000**	**925-1000**		
<N>	15.2	11.3	7.1	4.3		
σ_N	5.6	3.8	2.5	1.7		
Height Layers	**<100 m**	**<200 m**	**<300 m**	**<400m**	**<500 m**	**<700 m**
<N>	1.7	2.3	2.6	3.0	3.5	4.6

TABLE 2 Retrieved inversion and stratified layers for radiosonde profiles of 18 Nov 2001 (12Z) and 31 Dec 2009 (00Z). Z_b is the base of the inversion in m AGL, ΔZ is the thickness of the layer in m, ΔT is the temperature gradient across the layer in ^oC, and m_k in ^oC /100 m and b_k in ^oC are the fitting coefficients. The Class column indicates whether the layer represents an inversion (INV) when $m_k < 0$ or a stratified level (S) when $m_k > 0$; N (negative slope) and I (isothermal).

18 Nov 2001 12Z Strongly Stratified Case						
Layer	**Z_b [mAGL]**	**Depth ΔZ [m]**	**ΔT [^oC]**	**m_k [^oC /100 m]**	**b_k [^oC]**	**Class**
1	0	34	10.7	31.5	-10.5	S
2	34	35	0.5	1.4	-0.3	INV1
3	69	70	-0.8	-1.1	1.5	N
4	139	348	-2.4	-0.7	0.9	N
5	487	207	-0.8	-0.4	-0.6	N
6	694	31	0.9	2.9	-23.4	S
7	725	88	2.6	2.9	-23.8	S
8	813	128	3.1	0.1	-19.5	INV2
9	941	223	-1.6	-0.7	10.1	N
10	1164	632	-5.9	-0.9	12.6	N
11	1796	345	-1.5	-0.4	3.6	N
12	2141	552	-4.0	-0.7	9.8	N
13	2693	390	-3.8	-0.9	16.5	N
14	3083	255	-1.9	-0.7	9.5	N
15	3338	306	-3.0	-0.9	17.3	N
16	3644	370	-2.3	-0.6	4.3	N
31 Dec 2009 00Z Stratified Case						
Layer	**Z_b[mAGL]**	**Depth ΔZ [m]**	**ΔT [^oC]**	**m_k [^oC /100m]**	**b_k [^oC]**	**Class**
1	0	38	2.6	6.8	-25.3	S
2	38	97	6.8	7.0	-25.4	S

Table 2 (continued)

3	135	54	1.6	2.9	-19.9	INV1
4	189	180	0	0.0	-14.3	I
5	369	128	2.6	2.0	-21.8	S
6	497	132	0.2	0.2	-12.5	S
7	629	92	2.4	2.6	-27.9	S
8	721	51	0.8	1.6	-20.4	S
9	772	394	1.0	0.3	-10.3	S
10	1166	109	1.2	1.1	-20.1	INV2
11	1275	11	0	0.0	-6.1	I
12	1286	270	-0.8	-0.3	-2.3	N
13	1556	135	0.4	0.3	-11.5	INV3
14	1691	1096	-7.2	-0.7	4.6	N
15	2787	65	-0.4	-0.6	3.5	N
16	2852	413	-1.6	-0.6	-3.1	N

TABLE 3. Statistical parameters of the temporal series of inversion heights INV-1 to INV-5 during the period Jan. 2000 to Dec. 2010 over a total of 3633 analyzed radiosondes

	mean	median	std dev	0-10%	10-90%	90-100%	points
INV-1	377.1	302.0	312.9	0-78.5	78.5 -791.9	> 791.9	2326
INV-2	1230.8	1050.5	772.5	0-571.9	571.9- 2037.3	> 2037.3	1974
INV-3	2125.0	1844.5	1089.2	0 -963.3	963.3- 3771	> 3771	1128
INV-4	2719.8	2483.0	1146.1	0- 1364.9	1364.9-4428.7	> 4428.7	494
INV-5	3124.6	3036.5	1102.1	0-1739.9	1739.9-4859.6	> 4859.6	186

TABLE 4. Statistical analysis of inversion characteristics: inversion depth ΔZ [m], temperature strength ΔT [^{o}C] and stratification m_k [^{o}C /100 m] for INV-1 to INV-3.

		mean	median	std dev	0-10%	10-90%	90-100%
INV-1	ΔZ	377.1	302	312.9	8-107	107-1099	1099-3033
	ΔT	8.4	8.0	5.6	0.1-1.4	1.4-19.4	19.4-33.5
	m_k	3.2	2.4	3.0	0.1-0.7	0.7-6.6	6.6-27.6
INV-2	ΔZ	286.2	238.5	207.0	135-509.6	509.6-2411.7	2411.7-5465
	ΔT	2.9	2.2	2.8	0.1-0.6	0.6-9.8	9.8-34.1
	m_k	1.2	1.0	1.3	0.03-0.24	0.24-2.5	2.5-39.0
INV-3	ΔZ	220.5	175	160.5	415-961	961-3914	3914-5375
	ΔT	1.8	1.2	2.1	0.1-0.4	0.4-7.0	7.0-25.2
	m_k	0.9	0.7	0.9	0.02-0.4	0.4-7.0	7.0-9.4

TABLE 5. Statistical indicators of the temporal series of stratified layers within the INV-1 (SBI): ΔZ [m], ΔT [^{o}C], and maximum stratification [^{o}C/100 m].

		min	max	mean	median	std dev	0-10%	10-90%	90-100%	Cases
Stratified	ΔZ	5	918	113.6	76	112.6	5-36.2	36.2-458.8	458.8-918	1404
	ΔT	0.1	16.2	3.7	2.9	3.2	0.1-0.7	0.7-10.7	10.7-16.2	
	m	0.02	10	4.2	3.8	2.7	0.004-0.7	0.7-8.1	8.1-10	
Strongly Stratified	ΔZ	4	270	50.2	46	30.3	4-13	13-113	113-270	363
	ΔT	0.4	28.6	7.3	7.2	3.7	0.4-2.6	2.6-13.0	13.0-28.6	
	m	10	77.1	16.3	13.9	7.6	10-10.6	10.6-26.3	26.3-77.1	

TABLE 6. Statistical parameters describing the Elevated Inversion (EI) height, depth, strength, and dew point for the EI-1 and EI-2 temporal series.

	EI-AC		EI-WAA		EI-Transient(AC/WAA)		EI-Transient(WAA/AC)	
	EI-1	**EI-2**	**EI-1**	**EI-2**	**EI-1**	**EI-2**	**EI-1**	**EI-2:**
Cases	828	296	540	220	167	167	392	392
				Height [m AGL]				
mean	1431.4	2288.5	1186	1776.1	1116.4	1916.4	938.2	2294.7
median	1178.5	2134	1025	1426	985	1660	850.5	2065.5
std dev	883.2	1070.0	717.1	1072.5	661.0	1018.8	452.6	1070.7
min	178	656	156	415	156	523	135	581
max	5385	5365	5465	5265	4367	5053	4003	5375
0-10%	178-641.8	656-1035.6	156-568.8	415-842	156-541	523 -849.5	135-462.4	581-1143.4
10-90%	641.8-2888	1035.6-3985.2	568.8-2021.1	842-3462	541-1955	849.5-3428	462.4-1541.2	1143.4-3967.6
90-100%	2888-5385	3985.2-5465	2021.1-5465	3462-5265	1955-4367	3428-5053	1541.2-4003	3967.6-5375
				Depth [m]				
mean	280.5	210.6	316.8	224.6	245.5	223.9	284	227.8
median	235	175	254.5	167	190	189	249	172.5
std dev	194.9	148.1	234.8	169.3	181.6	161.4	203.1	166.9
min	26	19	23	31	31	25	18	30
max	1281	917	1274	1159	1170	1091	1648	1053
0-10%	26 - 94.2	19 - 71.4	23 - 87.4	31 - 80.6	31- 89.5	25 - 72.6	18 - 74.3	30 - 83.8
10-90%	94.2 - 652.6	71.4 - 451.2	87.4 - 794.9	80.6 - 485	89.5- 480.6	72.6 - 412.4	74.3 - 623.5	83.8 - 497.8
90-100%	652.6 – 1281	451.2 - 917	794.9 - 1274	485 - 1159	480.6 - 1170	412.4 - 1091	623.5 – 1648	497.8 - 1053
				Strength [°C / 100 m]				
mean	0.99	0.80	1.44	1.20	1.0	1.10	1.50	0.80
median	0.8	0.6	1.2	0.9	0.7	0.9	1.2	0.5
std dev	0.8	0.7	1.9	1.1	0.8	1.1	1.5	0.8
min	0.03	0.04	0.04	0.05	0.03	0.05	0.06	0.02
max	4.6	4.3	39.0	6.5	3.6	9.4	20.3	7.1
0-10%	0.03 - 0.2	0.04 - 0.13	0.04 - 0.3	0.05 - 0.2	0.03 - 0.2	0.05 - 0.2	0.06 - 0.4	0.02 - 0.14
10%-90%	0.2 - 2.0	0.13 - 1.7	0.3 - 2.8	0.2 - 2.7	0.2 - 2.4	0.2 - 2.5	0.4 - 2.9	0.14 - 1.8
90%-100%	2.0 - 4.6	1.7 - 4.3	2.8 - 39.0	2.7 - 6.5	2.4 - 3.6	2.5 - 9.4	2.9 - 20.3	1.8 - 7.1
				Dew Point [°C]				
mean	-4.0	-4.8	2.8	2.3	-3.5	2.5	2.7	-5.1
median	-2.4	-2.8	1.8	1.3	-1.8	1.5	1.8	-3.6
std dev	4.7	5.0	2.8	3.0	4.5	2.8	2.9	5.1
min	-32	-32.7	0.1	0.1	-22.5	0.1	0.1	-24.6
max	-0.1	-0.1	18.4	23.6	-0.1	13.4	29.1	-0.1
0-10%	-32 - (-16)	-32 - (-14.6)	0.1 - 0.6	0.1 - 0.3	-22.5 - (-13.8)	0.1 - 0.4	0.1 - 0.5	-24.6 - (-15.6)
10%-90%	-16 - (- 0.7)	-14.6 - (-0.6)	0.6 - 9.24	0.3 - 7.0	-13.8 - (-0.4)	0.4 - 8.66	0.5 - 7.9	-15.6 - (-0.7)
90%-100%	-0.7 - (-0.1)	-0.6 - (-0.1)	9.24 - 18.4	7.0 - 23.6	-0.4 - (-0.1)	8.66 - 13.4	7.9 - 29.1	-0.8 - (-0.1)

TABLE 7. Comparison of sodar and radiosonde observations (RAOBS) of SBI heights. The retrieved SBI heights from sodar are indicated by the mean calculated over a one hour period ($h_{SODAR\ 1hr}$) and the standard deviations calculated for one and three hours ($\sigma_{h(1\text{-}3hrs)}$).

Sounding	h_{RAOBS} [m]	$h_{SODAR\ 1hr}$ [m]	$\sigma_{h\text{-}(1\ hr)}$ [m]	$\sigma_{h\text{-}(3\ hrs)}$ [m]
11 Jan, 12 Z	295.0	168.5	23.0	31.5
12 Jan, 00Z	176.0	190.0	44.0	123.0
12 Jan, 12Z	210.0	168.5	23.0	31.0
13 Jan, 00Z	382.0	148.5	42.0	125.3
13 Jan, 12Z	51.0	66.4	15.0	93.0
14 Jan, 00Z	126.0	158.0	91.0	75.0

TABLE 8. Inversion levels measured by radiosonde profiles from 27 Jan (12 Z) to 31 Jan (00 Z). The inversion heights have been retrieved by the detection algorithm (section 3). Heights are expressed in m AGL; column dT/dZ [°C / 100 m] indicates the temperature gradient in the SBI and column T indicates the surface temperature.

Sounding	Heigths of Inversion Layers [m]	dT/dZ [°C/100m]	T [°C]
27 Jan, 12 UTC	167, 423, 1233, 1453, 1827	6.23	-20.9
28 Jan, 00 UTC	156.5, 456.5, 1042, 1423, 1748	5.19	-17.3
28 Jan, 12 UTC	53, 767, 1155, 1721	20.38	-21.3
29 Jan, 00 UTC	154, 704, 1733	5.11	-15.1
29 Jan, 12 UTC	54, 580, 1301	10.37	-14.5
30 Jan, 00 UTC	69.5, 445, 1386	3.45	-10.3
30 Jan, 12 UTC	167, 496, 1707	2.28	-12.3
31 Jan, 00 UTC	1450	1.00	-17.5

Chapter 5: Thesis Summary and Research Perspective

The first objective of this thesis was to determine the effect of the small scale drainage flow on the surface atmospheric boundary layer through micrometeorological measurements of turbulence at the surface and in upper levels. Three episodes have been selected to illustrate the main characteristics of this interaction: 18-19 January 2011, 7 February 2011 and 6 March 2011.

Under specific meteorological conditions (e.g., anticyclone situation), drainage flow occurs in two well-defined and different time-regimes: sustained flow and intermittent flow. Drainage flows may occur under different synoptic meteorological patterns as well but they are not the objective of study in this research. The intermittent drainage flow example is represented by the case on 7 February 2011 while the sustained flow is exemplified by the cases on 18-19 January and 6 March 2011. Particularly noticeable is that on 7 February, the drainage flow disrupts the basin on the basis of short-time flow "pulses" through the entire study case (see description on Chapter III). This intermittent flow exhibits overtime a decreasing strength (i.e., reduced maximum wind speed). Nevertheless, the resulting turbulent variables developed at the surface obtained from autocovariance and cross covariances of turbulent velocities and temperature reveals a larger development than in the cases of the sustained flow. Another important characteristic is associated with the basin response to the small scale flow variations (e.g., onset and breakup): the surface atmospheric boundary layer re-stratifies, immediately after flow breakup returning to a stagnant surface flow (i.e., stable state). This mechanism is due to the combined effect of the volumetric cooling imposed by the

arrival of the cold air mass that entered the basin and the strong radiative cooling rate under anticyclone conditions in the winter of the interior of Alaska.

On the other hand, the examples illustrating the sustained drainage flow on 18-19 January and 6 March exhibits a longer timescale (i.e., >3hrs). In these cases; the time-averaged momentum transport into the basin is smaller because the continuous presence of the drainage flow in the basin hampers the surrounding environment to condition the flow motion. Conversely, turbulent kinetic energy (TKE), surface stress (τ_0), and friction velocity (u^*) all have similar characteristics while turbulent sensible heat fluxes are different and the temporal evolution of wind direction from the northwest/west-northwest in the vertical up to 200 m, and a decrease in temperature and consequently decrease of the sensible heat fluxes agrees well.

The second research objective was to study the effect of the small scale drainage flow in the vertical structure of the ABL. In the three detailed experimental case studies it is shown that at the onset of the drainage flow an increase in wind speed in the first 200 m of the ABL. This signature coincides in time with surface measurements and turbulent measurements indicative of drainage flow. In the first 200 m of the ABL and at specific heights, the thermal turbulence C_T^2 measurements increased due to the onset and time variations of the drainage flow. From these results it is concluded that the changes in C_T^2 only can occur due to shear-driven thermal turbulence which magnifies as the vertical gradient of wind speed is maximum (i.e., above and below the wind maximum) if the previous state of the ABL was slightly stable or near neutral but without significant thermal and mechanical turbulence which has been verified in the three studied cases.

Therefore, increases of C_T^2 are exclusively driven by shear stress leading to thermal stratification of the upper layers above the wind maximum and at the surface atmospheric boundary layer below the wind maximum. However the development of turbulence in both regions follows different interacting processes. For instance, in the surface atmospheric boundary layer the turbulence is driven by the friction with the surface, damped by the surface layer thermal stratification and the shear-driving turbulence imposed by the drainage current while in upper levels, above the wind maximum, the turbulence is driven by shear and local stratification. These physical mechanisms are present in time at the onset of the drainage flow and the interplay between these mechanisms explains why at the beginning the flow, in the surface layer, is buoyancy dominated. The flow later on becomes shear-driven when the stratification at the surface has been destroyed.

From calculation of the surface turbulent magnitudes it can be seen that the kinematic momentum is stronger during the 6 March case study. This larger difference is originated from the higher thermal contrast existing between the source basin, the Goldstream Valley, and the target basin, the Tanana River Valley during the corresponding time of the winter. This difference arises because of the introduction of the diurnal cycle of solar radiation during the late winter affecting mostly one of them (the Tanana Valley). Therefore, the surface effects and stratification in late winter are more sudden and stronger than in the deep winter. Consistent with this hypothesis, it has also been observed during Wi-BLEx that the increased momentum borne by late winter drainage flow causes the flow to penetrate farther out into the valley. The spatial

extension of the flow will: (1) cause more vertical and horizontal mixing in the valley of anthropogenic air pollution, (2) cause stratification to occur over a large area close to the Fairbanks area foothills, and (3) cause stronger and faster micrometeorological effects at the surface layer.

The third objective was to determine if synoptic forces other than anticyclones affect the occurrence of drainage flows. Based on a simplified concept, the occurrence of the drainage flow depends upon the thermal difference, that at basin scales that can be accumulated, and the stratification that is built on them mainly due to surface radiative cooling. Therefore, during the course of this research, a hypothesis was elaborated in terms of investigating at the synoptic-scale, if forcing from elevated inversions in the Tanana Valley Basin may have an effect on the occurrence of drainage flow. The analysis of ten-years of thermodynamic soundings is detailed in Chapter IV where the layered structure of the winter ABL is analyzed in detail. This research provides observational evidence of what can be called a dynamic-radiative coupling between EI-layers and surface based inversions during synoptic changes. The observations provided evidence of formation of the EI layers in the presence of a SABL and of the decreasing stratification level in the SABL giving by the radiative-dynamic interaction of these two inversion layers whenever no other dynamic mechanism is present (e.g., advective flows, subsidence, upsidence, etc). This mechanism reduces strength in the surface stratification favoring the conditions for the drainage flow to penetrate the SABL.

Summarizing, the investigated drainage flow and its interaction with the SABL play an important role in the surface energy balance of an area (e.g., basin) by forcing the

surface sensible heat flux to be negative. It must be noted as well that forcing negative turbulent fluxes at the surface interface will also impose a boundary condition for sub-soil temperature regimes impacting upon frozen soils and vegetation. The spatial and temporal scales of variability of this phenomenon were determined in this research and are important characteristics to further introduce this process in mesoscale models. The connection between the surface atmospheric boundary layer turbulence and the upper layers in the ABL remains as further research subjects. At the onset of the drainage flow the shear-stress introduced by the velocity profile of wind speed in the ABL produces two region of shear, above and below the height of maximum of wind speed (leading edge of the drainage flow). While in upper shear-driven layer the turbulence is generated after balancing between local ABL stratification and shear-driven turbulence; turbulence in the lower layer below the speed maximum includes an additional term of surface friction and with complex stratification profiles.